

Electrokinetic and Optical Detection of Nucleic Acids for Biomedical Diagnosis in Microfluidics

Rui Miguel Raposo Pinto

Thesis to obtain the Master of Science Degree in
Biomedical Engineering

Supervisor: Doctor João Pedro Estrela Rodrigues Conde

Co-supervisor: Doctor Francisco Javier Lombardo Enguita

Examination Committee

Chairperson: Doctor Cláudia Alexandra Martins Lobato da Silva

Supervisor: Doctor João Pedro Estrela Rodrigues Conde

Member of the Committee: Doctor Duarte Miguel de França Teixeira dos Prazeres

June 2014

Agradecimentos

Em primeiro lugar, gostaria de fazer um agradecimento especial à minha família, em especial aos meus pais, por todo o apoio e paciência ao longo da minha formação, especialmente nos últimos meses, durante os quais tive a oportunidade de sentir como é fazer investigação científica. Lamento ainda os muitos fins-de-semana assombrados pelo tratamento de dados experimentais.

Gostaria de agradecer ao INESC-MN pela oportunidade de trabalhar nas suas instalações e, em especial, ao Dr. João Pedro Conde, pela sua orientação nos aspectos mais técnicos do trabalho, pelas reuniões frequentes e pelo seu entusiasmo contagiate. Ao Dr. Francisco Enguita agradeço a discussão de alguns aspectos biológicos de ordem prática e a inspiração para o objectivo do trabalho a longo prazo (detecção de miRNAs circulantes para fins de diagnóstico).

Não podia deixar de agradecer a companhia dos meus colegas no dia-a-dia do trabalho laboratorial, pela partilha de opiniões e pelas suas ideias e críticas construtivas acerca deste trabalho. Sem a partilha das frustrações, seria fácil sermos tomados pela desmotivação. Nas reuniões do grupo de investigação, foi sempre um prazer partilhar convosco os últimos resultados e sentir que fazia parte deste grupo. Saúdo ainda a Dra. Virginia Chu pelo seu papel importante na liderança do grupo.

Agradeço aos técnicos incansáveis do INESC-MN, nomeadamente ao Fernando Silva, à Virgínia Soares e ao José Bernardo pelo apoio técnico na sala limpa. Dedico ainda um agradecimento ao Dr. Narayanan Srinivasan pela ajuda nas sessões intermináveis de microspotting.

A todos o meu obrigado e desejo das maiores felicidades. Como disse em tempos Henry Ford, “Quer você pense que pode, ou que não pode, você está certo”, e certamente que vocês conseguirão.



INESC-MN Optics Group (December 2013)

Resumo

Os *microRNAs* são *RNAs* endógenos, com cerca de 22 nucleótidos, que têm papéis regulatórios importantes nas células. Estes agentes biologicamente activos foram detectados em circulação, podendo ser usados como biomarcadores de diversas doenças. Os sistemas *lab-on-a-chip* podem ser decisivos na análise de *microRNAs* na prática clínica. Nesta tese, foi explorado um princípio de detecção eléctrica, sem marcação, para a detecção de ácidos nucleicos em microfluídica.

Os microcanais foram fabricados em *PDMS* e selados contra vidro onde previamente foram depositados eléctrodos planares, permitindo realizar medições electrocinéticas e de fluorescência. Provou-se que as medições de potencial e corrente de *streaming* são adequadas para a descrição da carga eléctrica global do canal. Os potenciais ζ calculados variaram entre -67 mV (água desionizada) e -4.6 mV (100 mM PB), num canal não funcionalizado. Para a detecção de *DNA* alvo, o microcanal foi tratado com *APTES*, sonda de *ssDNA* e bloqueado com *BSA*. Depois da imobilização da sonda, a sua densidade superficial era $2.09 \times 10^4 \mu\text{m}^{-2}$ (15.7% de uma monocamada densa) e, depois do passo de bloqueio, $9.71 \times 10^3 \mu\text{m}^{-2}$ (7.3% de uma monocamada densa). Usando uma amostra de 16 nL, as correntes de *streaming* permitiram detectar 5 μM de *DNA* alvo (com a sequência do *miR-122*) e distingui-lo de um controlo negativo (com a sequência do *miR-375*). As medições de fluorescência permitiram detectar 500 nM de *DNA* alvo.

Finalmente, é apresentada uma lista de sugestões, de modo a melhorar a sensibilidade e especificidade do método e integrá-lo num sistema de análise miniaturizado.

Palavras-Chave: corrente de streaming; fluorescência; microfluídica; *microRNA*; *DNA*; sem marcação

Abstract

microRNAs are endogenous RNAs with a length of about 22 nucleotides that can play important regulatory roles in the cells. The recent discovery of circulating miRNAs has opened the possibility to study this class of biologically active agents as biomarkers of disease. Lab-on-a-chip systems may play a decisive role in the profiling of microRNAs for point-of-care diagnostic purposes. This thesis explores an electrical, label-free detection principle for microfluidic detection of nucleic acids.

PDMS microchannels were sealed against glass where planar electrodes were previously deposited on. This microfluidic system allowed for electrokinetic and fluorescence measurements. Transient streaming current and potential measurements proved to be accurate in describing the overall electrical surface charge of the channel. For a bare channel, ζ -potential values varied between -67 mV (DI Water) and - 4.6 mV (100 mM PB). In order to recognize the target DNA, the microchannels were functionalized with APTES, ssDNA probe and blocked with BSA. After probe immobilization, the probe density on the surface was $2.09 \times 10^4 \mu\text{m}^{-2}$ (15.7% of a dense monolayer) and, after the blocking step, it dropped to $9.71 \times 10^3 \mu\text{m}^{-2}$ (7.3% of a dense monolayer). Using a 16 nL sample, streaming current measurements allowed to detect 5 μM of target DNA (miR-122 sequence) and distinguish it from a negative control (miR-375 sequence), while the fluorescence measurements detected down to 500 nM target DNA.

A considerable number of enhancements are suggested in order to improve the sensitivity and specificity of the method and to integrate it on a micro total analysis system.

Key Words: *DNA; fluorescence; label-free; microfluidics; microRNA; streaming current*

Index

Index of Tables	G
Index of Figures	G
List of Abbreviations	K
1. Introduction.....	1
1.1. Motivation and Thesis Outline	1
1.2. microRNAs as Novel Biomarkers	2
1.2.1. Biomarker Definition and Desired Characteristics	2
1.2.2. Biogenesis and Functions of the microRNAs.....	3
1.2.3. Circulating microRNAs	6
1.2.4. Association with Disease and Possible use as Biomarkers.....	7
1.3. State-of-the-Art in microRNA Measurement.....	10
1.3.1. Main microRNA Profiling Techniques	10
1.3.1.1. Microarrays	11
1.3.1.2. Quantitative Reverse-Transcription Polymerase Chain Reaction	14
1.3.1.3. Northern Blotting.....	18
1.3.1.4. Next-Generation Sequencing	19
1.3.2. Source Material for Circulating microRNA Profiling	22
1.3.3. Storage, Preparation and Enrichment of microRNAs	22
1.4. Microfluidics and Lab-on-a-Chip.....	24
1.4.1. Introduction to Micro Total Analysis Systems	24
1.4.2. The Main Functional Modules	25
1.4.3. Considerations on the Fabrication of Microfluidic Devices	27
1.4.4. Review of microRNA Detection on Microfluidics.....	28
1.5. The Goals of This Thesis.....	30
2. Electrokinetics in Microfluidics	31
2.1. Historic Background	31
2.2. The Origin of the Surface Charge.....	31
2.3. The Electric Double Layer	32
2.4. Streaming Current and Potential in Microfluidics	33

3.	Experimental Methods	36
3.1.	Solution Preparation	36
3.2.	DNA Oligonucleotides	36
3.3.	Surface Functionalization Protocol	37
3.4.	Microfluidic Device Fabrication	39
3.4.1.	Hard Mask Fabrication	39
3.4.2.	SU-8 Mould Fabrication	41
3.4.3.	PDMS Microchannel Fabrication	42
3.4.4.	Electrode Deposition and Patterning on Glass	43
3.4.5.	Device Sealing and Ancillary Equipment Connection	45
3.5.	Streaming Current and Potential Measurements	47
3.6.	Fluorescence Measurements	50
3.7.	DNA Surface Density Calibration Using the Nanoplotter	51
4.	Results and Discussion	53
4.1.	Measurements with DI Water, KCl and Buffer Solutions	53
4.2.	Microchannel Silanization	60
4.3.	Detection of 5 µM Target DNA	62
4.4.	Towards the Detection of Lower Target Concentrations	66
4.4.1.	Blocking Step Optimization	67
4.4.2.	Steady State vs Flow Incubation	70
4.4.3.	DNA Surface Density Determination Using Fluorescence	71
5.	Conclusions and Future Endeavors	77
5.1.	Conclusions	77
5.2.	Future Perspectives	78
6.	References	I
7.	Annexes	IX
7.1.	Run Sheet – Aluminium Hard Mask Fabrication	IX
7.2.	Run Sheet – SU-8 Mould Fabrication	XIV
7.3.	Run Sheet – PDMS Microchannel Fabrication	XVI
7.4.	Run Sheet – TiW Electrode Fabrication	XVIII

Index of Tables

Table 1 – Comparison of the main next-generation sequencing platforms. Based on (Liu, et al., 2011)	20
Table 2 – Summary of the main features of microarrays, quantitative real-time reverse transcription PCR (qRT-PCR) and next-generation sequencing (NGS) as tools for miRNA profiling and discovery. For more details on the normalization strategies, see (Meyer, et al., 2010).....	21
Table 3 – Name, sequence and modifications (Mod.) of the oligonucleotides used in this work.....	37
Table 4 – Typical experimental pumping and waiting periods for the streaming current measurements.	49
Table 5 – Fluorescence microscope filters used, respective characteristics and fluorophore response.	50
Table 6 – Experimental and reference zeta-potential values as a function of the ionic strength of the solutions and depending on the material (silica or PDMS). Reference 1: (Erickson, et al., 2000). Reference 2: (Kirby & Hasselbrink, 2004).	60

Index of Figures

Figure 1 – Predicted stem loops of the founding <i>C. elegans</i> miRNAs, lin-4 (left) and let-7 (right) RNAs. Mature miRNAs (red) and flanking sequence (black). Adapted from (Bartel, 2004).	3
Figure 2 – miRNA biogenesis pathway (A) and the two posttranscriptional mechanisms that downregulate gene expression: mRNA cleavage (B) or translational repression (C). Adapted from (Bartel, 2004).....	5
Figure 3 – Biogenesis and release of miRNAs from a donor cell (A). Extracellular miRNA is protected from degradation due to loading into microvesicles, exosomes, apoptotic bodies or due to the association with high-density lipoprotein (HDL) or other miRNA-binding protein complexes (RBP). Extracellular miRNAs can be transferred to recipient cells where they modify gene expression (B). Adapted from (Kinet, et al., 2013).	7
Figure 4 – Overview of the miRNA signatures (overexpression or underexpression of specific miRNAs) that correspond to different CVDs, namely ischemic heart disease (IHD), heart failure (HF), stroke, coronary artery disease (CAD), diabetes mellitus (DM) and hypertension. Adapted from (Empel, et al., 2012).	8
Figure 5 – Microarray fluorescence image and analysis. On the left: example of the output of a microarray experiment (target molecules labelled with red and green fluorescent dyes), adapted from (Reinke, 2006). On the right: Graphical representation of the analysis of a microarray experiment, where different levels of RNA expression, corresponding to different spots, can be distinguished by the height of the peaks, adapted from (FitzGerald, et al., 2005).	11
Figure 6 – RNA (on the left) and LNA (on the right) monomer structures. Adapted from (Doessing & Vester, 2011).	13

Figure 7 – Reverse transcription of miRNA using specific primers: stem-loop primer (left) and linear primer (right). Adapted from (Benes & Castoldi, 2010).....	14
Figure 8 – Universal reverse transcription of all the mature miRNAs contained in the sample by enzymatic tailing of the miRNAs by using Poly(A) Polymerase (left) or T4 RNA Ligase (right) Adapted from (Benes & Castoldi, 2010).	15
Figure 9 – Detection of the amplicon by the use of the SYBR Green intercalator. Adapted from (Benes & Castoldi, 2010).	16
Figure 10 – Detection of the amplicon by TaqMan probes. Adapted from (Benes & Castoldi, 2010).	17
Figure 11 – Detection of mature and pre-cursor miR-205 using NB. tRNAlv is used as a RNA loading control. Adapted from (Tran, 2009).	18
Figure 12 – Pictures and schematics of examples of microfluidic-based POC platforms: (A) i-STAT (Abbott), (B) Epocal and (C) Abaxis. Adapted from (Chin, et al., 2012).....	25
Figure 13 – Potential (Ψ) and flow (u) profiles as a function of the distance (y) from the solid surface (top) and representation of the respective electric double layer in the vicinity of a flat surface (bottom). Adapted from (Li, 2004) and (Kirby & Hasselbrink, 2004).....	33
Figure 14 – Schematic of the streaming current (I_s), conduction current (I_c) and external (faradic) current (I_{ext}), established during a streaming current experiment inside a microchannel. For charge conservation, $I_s = I_c + I_{ext}$	35
Figure 15 – Surface functionalization protocol illustration.....	38
Figure 16 – Basic components of a magnetron sputtering system (left) and Nordiko N7000 deposition system at INESC MN cleanroom (right). Image on the left adapted from (Micro Magnetics, 2014).	39
Figure 17 – AUTOCAD design of the microfluidic chip (top view), containing two microchannels (left), and detail of the microchannel (right), including dimensions. Design as by (Martins, et al., 2011).	40
Figure 18 – Hard mask fabrication flowchart (side view). Dimensions of materials not to scale.	41
Figure 19 – Glass samples with and without aluminium (left) and complete hard mask with the shape of two microchannels patterned on it (right). This hard mask will be used to expose a layer of SU-8 photoresist and create the mould for the PDMS microchannel fabrication.....	41
Figure 20 – SU-8 mould fabrication flowchart (side view). Dimensions of materials not to scale.....	42
Figure 21 – Flowchart of the PDMS fabrication by casting on a SU-8 mould (side view). Dimensions of materials not to scale.	42
Figure 22 – PDMS chip upon removal from the SU-8 mould. The mould is on the bottom of a Petri plate, the liquid PDMS is poured on top, cured on the oven, and then the PDMS chip is cut from the mould.	43
Figure 23 – AUTOCAD design of the electrodes and pads for two microchannels (left), and detail of the design (right), including dimensions (top view). Design as by (Martins, et al., 2011).	44
Figure 24 – Flowchart of the electrode deposition and patterning on glass (side view). Dimensions of materials not to scale.	44

Figure 25 – Images of the TiW electrode microfabrication. Glass sample after lithography, with the transparent areas not covered by photoresist (left) and glass sample after TiW deposition, ready for the liftoff step (right).	44
Figure 26 – PDMS chip (on the left), ready to be sealed against the glass with the TiW electrodes (on the right).	45
Figure 27 – Photographs of the sealed microfluidic devices. Top view (left) and the bottom view (right) of the chips employed in the streaming current and fluorescence experiments.	46
Figure 28 – Some of the parts used to manufacture the chip holder (top left), top view of the chip holder with mounted microfluidic chip, two tubes and adapters (top right), side view of the chip holder and chip (bottom left) and chip holder mounted inside a metallic box enclosure (bottom right).	46
Figure 29 – Picoammeter, syringe pump and metallic box (left) and detail of the syringe pump and metallic box (right).....	47
Figure 30 – Positive current convention. A neutral species gives an electron to the inlet electrode. The electron is driven through the picoammeter and delivered to a positive counterion at the outlet electrode, resulting in a positive current reading in the Keithley 237. If the measured current is positive, the counterions in the EDL are positive and the surface charge is negative.....	47
Figure 31 – Example of a streaming current measurement with DI water in the channel. No transient behaviour of the external current is observed due to the low ionic strength of the solution.....	48
Figure 32 – Example of a streaming current measurement with a 1 mM KCl solution in the channel. The external current is transient because of the higher ionic strength of the solution, which decreases the channel resistance.....	49
Figure 33 – Illustration of the method used to calculate the streaming current values from the measured external currents, in the case of a non-transient external current (left) and for a transient external current (right).....	49
Figure 34 – Leica DMLM microscope setup, used for the fluorescence imaging (left) and fluorescence image acquired using the I3 filter, with highlighted regions of interest (right).....	50
Figure 35 – SIM Nanoplotter 2.1 system overview (left) and detail of the open nanoplotter; note the PDMS chip on the center of the image, ready for spotting; the oligonucleotide solutions are deposited on the well plate (right).	52
Figure 36 – PDMS microchannel after spotting 1.12 nL drops. The first four spots on the left dried on the center of the channel, but the last three dried towards the wall on the channel. The length of the microchannel is 4 mm and the width 200 µm. Imaging in visible light, using the Leica DMLM microscope with a 2.5x objective.	52
Figure 37 – Example of a 1.12 nL spot of DNA probe solution. Imaging in visible light (left) and using the I3 fluorescence filter (right), on the Leica DMLM microscope, with the 20x lens. The width of the microchannel is 200 µm.....	52
Figure 38 – Linear dependency of the streaming current on the flow rate, for DI water, KCl solutions, PB and PBS.....	53
Figure 39 – Linear dependency of the streaming potential on the flow rate, for DI water, KCl solutions and PBS. On this streaming potential scale, the measurements for the higher counterion concentrations cannot be clearly distinguished (see the next figure).	55

Figure 40 – Linear dependency of the streaming potential on the flow rate, for DI water, KCl solutions and PBS.....	56
Figure 41 – Apparent conductivity of KCl, PB and PBS solutions in the microchannel, as a function of the ionic concentration.	57
Figure 42 – Zeta potential as a function of the total ionic concentration of the solutions flowing in the microchannel. A logarithmic dependency is observed. The results are identical when calculating the zeta potential with the streaming current data and the streaming potential data.....	59
Figure 43 – Streaming current measured (DI water at 10 μ l/min) before and after the APTES silanization. The surface charge is reverted after silanization. Error bars represent the standard deviation due to 3 repetitions of the experiment, on distinct channels.	61
Figure 44 – Optimization of the washing conditions after APTES silanization.....	62
Figure 45 – Streaming current and fluorescence measurements after each functionalization step, culminating in the detection of 5 μ M of target DNA. It is possible to distinguish between a fully complementary DNA target (miR-122) and a DNA control target (miR-375). Error bars represent the standard deviation due to 3 repetitions of the experiment, in distinct channels.	63
Figure 46 – Target DNA fluorescence on the functionalized microchannels, after the wash with PB at 10 mM. Complementary target (left) and non-complementary, control target (right). The complementary target signal is six times larger than the one of the non-complementary target, demonstrating specificity of the system.	65
Figure 47 – Streaming current and fluorescence results of the experiment for the detection of 500 nM of target DNA by static incubation in the channel. The streaming current measurements do not distinguish between a fully complementary DNA target (miR-122) and a non-complementary DNA control target (miR-375), but fluorescence does. Error bars represent the standard deviation due to 3 repetitions of the experiment, in distinct channels.	67
Figure 48 – Streaming current and fluorescence results of the experiment for the detection of 5 μ M of target DNA by static incubation in the channel (no surface blocking performed).....	68
Figure 49 – Streaming current and fluorescence results of the experiment for the detection of 5 μ M of target DNA by static incubation in the channel (salmon sperm DNA blocking test).	68
Figure 50 – BSA and salmon sperm DNA as surface blocking agents, compared with a control (no blocking). Streaming current and target fluorescence (TX2 filter) after the 10 mM PB wash step.	69
Figure 51 – Streaming current after static or flow incubation of target DNA. Readings performed with 10mM PB. The bars represent the average and the error bars the standard deviation of the individual experiments in different channels.....	70
Figure 52 – Target fluorescence (TX2 filter) after static or flow incubation of target DNA. The bars represent the average and the error bars the standard deviation of the individual experiments in different channels.	70
Figure 53 – miR-122 possible self-annealing sites (red).....	71
Figure 54 – Exposure linearity check. The fluorescence of one probe spot was imaged for several exposure conditions and the fluorescence intensity, after treatment on	

imageJ, was plotted against the exposure time. As long as there is no over exposure (saturation on at least one channel), the linearity holds good.	72
Figure 55 – Absolute probe fluorescence (I3 filter) as a function of the probe surface density. Fluorescence values adjusted to the scale of 2 s exposure, unitary gain conditions. Error bars (standard deviation) are due to spot area and fluorescence dispersion, given that each concentration was spotted 3 times.	73
Figure 56 – Absolute target fluorescence (TX2 filter) as a function of the target surface density. Fluorescence values adjusted to the scale of 2 s exposure, unitary gain conditions. Error bars (standard deviation) are due to spot area and fluorescence dispersion, given that each concentration was spotted 3 times.	74

List of Abbreviations

A	Adenine
Ago2	Argonaute 2
APTES	(3-AminoPropyl)TriEthoxySilane
BSA	Bovine Serum Albumin
C	Cytosine
CAD	Coronary Artery Disease
cDNA	complementary DNA
CVD	Cardiovascular Disease
dA	deoxyAdenosine
DI	Deionized
DNA	DeoxyriboNucleic Acid
dsDNA	double-stranded DNA
dT	deoxyThymidine
DWL	Direct Write LASER
EDL	Electric Double Layer
EP	Ectopic Pregnancy
G	Guanine
HCMV	Human CytoMegaloVirus
hCG	human Chorionic Gonadotropin
HDL	High-Density Lipoprotein
HDMS	HexaMethylDiSilazane
HPLC	High Performance Liquid Chromatography
IPA	IsoPropyl Alcohol
ITP	IsoTachoPhoresis
kb	kilobase
KCl	Potassium Chloride

LDL	Low-Density Lipoprotein
LE	Leading Electrolyte
LOC	Lab-On-a-Chip
miRNA	microRNA
MSP	miRNA-specific primer
mRNA	messenger RNA
NB	Northern Blotting
NGS	Next-Generation Sequencing
nt	nucleotides
PB	Phosphate Buffer
PBS	Phosphate Buffered Saline
PCR	Polymerase Chain Reaction
PDMS	Poly(DiMethylSiloxane)
PGMEA	Propylene Glycol Monomethyl Ether Acetate
pI	Isoelectric point
PMMA	Poly(MethylMethAcrylate)
POC	Point-Of-Care
qRT-PCR	quantitative real-time Reverse-Transcription Polymerase Chain Reaction
qPCR	quantitative Polymerase Chain Reaction
RISC	RNA-Induced Silencing Complex
RNA	RiboNucleic Acid
RNAi	RNA interference
rRNA	ribosomal RNA
SA	Spontaneous Abortion
SG	SYBR Green
siRNA	small interfering RNA
sRNA	small RNA
ssDNA	single-stranded DNA
SVG	Silicone Valley Group
T	Thymine
T2DM	Type 2 Diabetes Mellitus
TE	Trailing Electrolyte
TiW	Titanium Tungsten
Tm	melting Temperature
VIP	Viable Intrauterine Pregnancy
µTAS	micro Total Analysis Systems

1. Introduction

1.1. Motivation and Thesis Outline

Deoxyribonucleic Acid (DNA) was demonstrated as the genetic material by Oswald Theodore Avery in 1944 and its double helical strand structure, composed of four bases, was determined by James D. Watson and Francis Crick in 1953, leading to the central dogma of molecular biology. (Avery, et al., 1944) (Watson & Crick, 1953) Genomic DNA defines the species and the individuals, making the DNA sequence fundamental to the research on the structures and functions of cells, and the decoding of life mysteries. Ribonucleic acid (RNA) also plays an important role in the central dogma of biology, being the messenger that carries the genetic information until it is translated into a protein. In addition, RNA is involved in regulatory processes that can be considered as important as the genetic information itself.

Medicine and other bioscientific disciplines investigate the mechanisms behind the various pathologies that affect our health in order to treat or manage them, but prior to any intervention or prescription, there is the need for accurate diagnosis. Medicine has now many diagnostic tools unimaginable a century ago, such as new radiology and laboratory techniques. Biomarkers for various conditions are continuously discovered and there is the need to develop detection schemes for them, and then to implement them in a practical way, in order to make better, faster and easier diagnostics. Working on the biomedical field, I hope that our discoveries lead to the delivery of better healthcare services, the increasing of life expectancy and, ultimately, the quality of life improvement of the populations.

The present work goes towards the development of a RNA detection system that provides a fast analysis without requiring sample labelling. The purpose of this system would be to assist medical diagnosis, given that the presence and concentration of different RNAs in circulation has been associated to various diseases. microRNA (miRNA), a recently discovered circulating biomarker, is presented in the current chapter (Chapter 1), as well as the state-of-the-art techniques for its detection, followed by the approach used in this original work. Chapter 2 is devoted to the study of the physicochemical phenomena that constitutes the foundation of the developed system. Chapter 3 is dedicated to the description of the experimental methods and materials. In Chapter 4, the results of a series of experiments are synthesized, explored and discussed as much as possible. Conclusions and future endeavors close the thesis on Chapter 5.

1.2. microRNAs as Novel Biomarkers

1.2.1. Biomarker Definition and Desired Characteristics

Before introducing miRNAs and discussing its use as biomarkers, it is sensible to shortly review the definition of biomarker as well as different types and properties of biomarkers. The term biomarker (biological markers) was introduced in 1988 as a Medical Subject Heading term: “Measurable and quantifiable biological parameters (e.g., specific enzyme concentration, specific hormone concentration, specific gene phenotype distribution in a population, presence of biological substances) which serve as indices for health- and physiology-related assessments, such as disease risk, psychiatric disorders, environmental exposure and its effects, disease diagnosis, metabolic processes, substance abuse, pregnancy, cell line development, epidemiologic studies, etc.” (United States National Library of Medicine, 2013)

A biomarker may be measured on a biological sample (blood, urine, or tissue test), it may be extracted from a recording obtained from a person (blood pressure, electrocardiogram, or Holter), or it may derive from an imaging test (echocardiogram or computerized tomography scan). Biomarkers can indicate a variety of health or disease characteristics, including the level or type of exposure to an environmental factor, genetic susceptibility, genetic responses to exposures, markers of subclinical or clinical disease, or indicators of response to therapy. Accordingly, biomarkers can be classified as antecedent biomarkers (identifying the risk of developing an illness), screening biomarkers (screening for subclinical disease), diagnostic biomarkers (recognizing overt disease), staging biomarkers (categorizing disease severity), or prognostic biomarkers (predicting future disease course, including recurrence and response to therapy, and monitoring efficacy of therapy). (Vasan, 2006)

The desirable properties of biomarkers vary with their intended use. For screening biomarkers, features such as high sensitivity, specificity and predictive values, and low costs are important. For diagnostic markers, in addition to the aforementioned characteristics, rapid sustained elevation, high tissue specificity, release proportional to disease extent, and assay features conducive to point-of-care (POC) testing are critical. For prognostic biomarkers, narrow intra-individual variation and tracking with disease outcome or therapy are critical, while costs may be less important because only people with disease are tested. (Vasan, 2006) Some biomarkers may be used for both diagnostic and prognostic purposes.

Biomarkers that do not change disease management cannot affect patient outcome and, therefore, are unlikely to be cost-effective. Typically, for a biomarker to change management, it is important to have evidence that risk reduction strategies should vary with biomarker levels, and a biomarker-guided approach translates into better patient outcomes compared with a management scheme (usually the current standard of care) without the biomarker levels. (Vasan, 2006)

This work is motivated by the possibility of using miRNA levels as biomarkers, which will be now presented and described in some detail.

1.2.2. Biogenesis and Functions of the microRNAs

The discovery of the first miRNA is addressed on this paragraph, based on an explanation by (Bartel, 2004). In 1993, it was discovered that lin-4, a gene known to control the timing of *C. elegans* larval development, does not code for a protein but instead produces a pair of small RNAs. (Lee, et al., 1993) One is approximately 22 nucleotides (nt) in length, and the other has approximately 61 nt. The longer one was predicted to fold into a stem loop and was proposed to be the precursor of the shorter one. It was also noticed that these lin-4 RNAs had antisense complementarity to multiple sites in the lin-14 gene. This complementarity fell in a region previously proposed to mediate the repression of lin-14 by the lin-4 gene product (Wightman, et al., 1991). This regulation substantially reduces the amount of LIN-14 protein without noticeable change in levels of lin-14 messenger RNA (mRNA). Together, these discoveries supported a model in which the lin-4 RNAs pair to the lin-14, causing translational repression of the lin-14 message as part of the regulatory pathway that triggers the transition from cell divisions of the first larval stage to those of the second (Lee, et al., 1993) (Wightman, et al., 1993)

The shorter lin-4 RNA (Figure 1) is now recognized as the founding member of an abundant class of tiny regulatory RNAs called miRNAs. In short, miRNAs are endogenous RNAs with a length of about 22 nt that can play important regulatory roles in animals and plants by targeting mRNAs for cleavage or translational repression (Bartel, 2004). The importance of miRNA-mediated gene regulation is coming into focus as more miRNAs and their regulatory targets and functions are discovered. Currently, thousands of miRNAs have been identified in humans and other species, and online miRNA sequence repositories, such as the miRbase database, are available. (Almeida, et al., 2011)

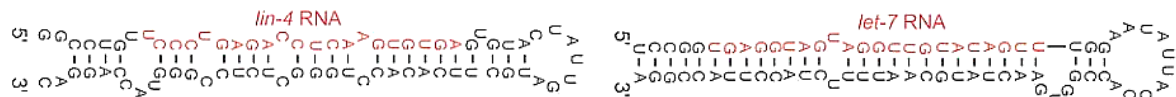


Figure 1 – Predicted stem loops of the founding *C. elegans* miRNAs, lin-4 (left) and let-7 (right) RNAs. Mature miRNAs (red) and flanking sequence (black). Adapted from (Bartel, 2004).

Most miRNA genes come from regions of the genome quite distant from previously annotated genes, implying that they derive from independent transcription units. Nonetheless, about a quarter of the human miRNA genes are preferentially in the same orientation as the predicted mRNAs, suggesting that most of these miRNAs are not transcribed from their own promoters but are instead processed from the introns of pre-mRNAs. This arrangement provides a convenient mechanism for the coordinated expression of a miRNA and a protein. (Bartel, 2004)

The RNA must go through a series of processing steps to go from a primary transcript that potentially extends 1 kilobase (kb), or even longer, to an approximately 22 nt mature miRNA. These mechanisms are well grounded in the review articles by (Bartel, 2004) and (Zeng, 2006), on which the present paragraph is based. The first step is the generation, in the nucleous, of an approximately 60 nt long hairpin RNA, called the precursor miRNA, or pre-miRNA (Figure 2A, Step 1). This precursor is excised from the primary transcript by an enzyme called Drosha, an RNaseIII-type endonuclease, which

produces duplex RNA products containing a 5'phosphate and a 3'-OH, with a 2 nt overhang at the 3' end (Figure 2A, Step 2). Drosha requires a regulatory subunit called DGCR8, which contains two double-stranded RNA-binding domains that presumably help the subunit to recognize the correct substrates. Once pre-miRNAs are produced, they are exported from the nucleus to the cytoplasm by Exportin5 and its Ran-guanosine triphosphate cofactor (Figure 2A, Step 3). Exportin5 mediates macromolecular nucleocytoplasmic trafficking and is specialized at binding to minihelix-containing RNAs with a 3' overhang, such as the pre-miRNAs. Exportin5 may also have the function of protecting pre-miRNAs from the moment they are generated in the nucleus until they are ready for the next cleavage step in the cytoplasm. In the cytoplasm, guanosine triphosphate is hydrolysed to guanosine diphosphate and the Exportin5 complex releases its cargo. In the next step, Dicer, another RNaseIII-type enzyme, cleaves the pre-miRNAs in the cytoplasm. Certain proteins with double-stranded RNA-binding domains, such as TRBP and PACT (in humans), bind to Dicer and contribute to its function, enhancing the affinity of Dicer for RNAs. Most Dicer proteins preferentially bind to single-stranded 3' ends of double-stranded RNAs. As a pre-miRNA generated by Drosha already contains a 2 nt 3' overhang, Dicer recognizes this feature and cleaves the double-stranded region approximately 20 nt away (Figure 2A, Step 4). The product is a miRNA duplex intermediate containing approximately 2 nt 3' overhangs at both ends. Dicer produces a miRNA duplex intermediate, yet usually only one of the two strands can be detected in cells. The selection of the mature miRNA strand is likely to involve differential binding to, and then differential retention of, the two individual RNA strands by Dicer and its associating proteins. At the RNA sequence level, it appears that the strand with the less stable hydrogen bonding at its 5' end within the original duplex is selectively stabilized and becomes the mature miRNA, whereas its complementary strand is lost. This property might explain why so many miRNAs have a uracil residue at their 5' ends. Such miRNAs have the highest chance of being selected given that a uracil:guanine base pair is less stable than a uracil:adenine pair, which in turn, is less stable than a guanine:cytosine pair. By eliminating half of the RNAs from the duplexes, the number of genes whose expression could be targeted is reduced. Dicer or its complex interacts with a family of proteins called Argonautes which may contribute to miRNA biogenesis by selecting or binding to and subsequently stabilizing mature miRNAs (Figure 2A, Steps 5 and 6). Argonaute proteins are thought to be a core component of the RNA-induced silencing complex (RISC), which identifies target messages based on the complementarity between the miRNA and the mRNA, and then the endonuclease of the RISC cleaves the mRNA.

In fact, microRNAs can direct the RISC to downregulate gene expression by two posttranscriptional mechanisms: mRNA cleavage (Figure 2B) or translational repression (Figure 2C). Following nucleocytoplasmic export, the miRNA pathway on animals appears to be indistinguishable from the central steps of RNA silencing pathways known as RNA interference (RNAi). According to the prevailing model, the choice of posttranscriptional mechanisms is not determined by whether the small silencing RNA originated as a small interfering RNA (siRNA) or a miRNA, but instead is determined by the identity of the target. (Bartel, 2004) Once incorporated into a cytoplasmic RISC, the miRNA will specify cleavage if the miRNA has sufficient complementarity to the mRNA, or it will repress productive translation if the mRNA does not have sufficient complementarity to be cleaved but does have a suitable constellation of miRNA complementary sites. If cleavage of the mRNA occurs, it is performed at a site

near the middle of the miRNA complementarity, measuring from the 5' end of the miRNA, between the nucleotides pairing to residues 10 and 11 of the miRNA (Figure 2B). When a miRNA guides cleavage, the cut is at precisely the same site as that seen for siRNA-guided cleavage. Also, the register of cleavage does not change when the miRNA is not perfectly paired to the target at its 5' terminus. Therefore, the cut site appears to be determined relative to miRNA residues and not relative to miRNA:target base pairs. After cleavage of the mRNA, the miRNA remains intact and can guide the recognition and destruction of additional messages. Regarding translational repression, the miRNA might repress translation at a step after translation initiation, in a manner that does not perceptibly alter the density of the ribosomes on the message, by the slowing or stalling of all the ribosomes on the message (Figure 2C). An alternative possibility is that translation continues at the same rate but is nonproductive because the newly synthesized polypeptide is specifically degraded. Because near-perfect complementarity is thought to be required for RISC-mediated cleavage but not translational repression, the lower degree of complementarity seen in animals suggests that translational repression is more prevalent in animals. (Bartel, 2004)

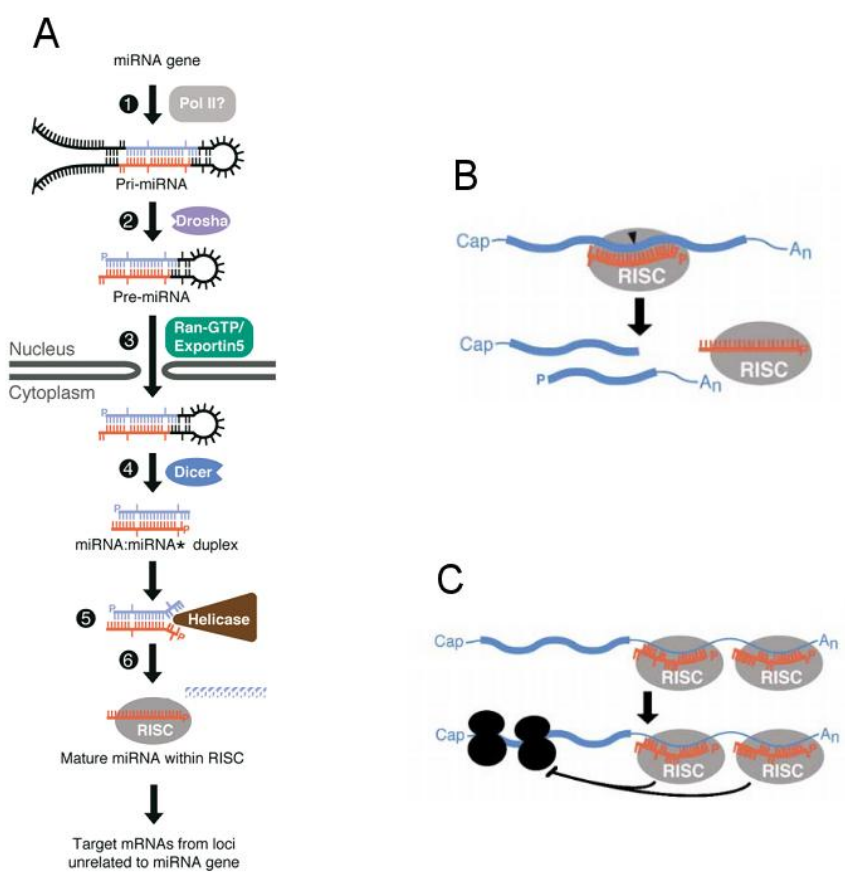


Figure 2 – miRNA biogenesis pathway (A) and the two posttranscriptional mechanisms that downregulate gene expression: mRNA cleavage (B) or translational repression (C). Adapted from (Bartel, 2004).

1.2.3. Circulating microRNAs

To achieve the goal of early diagnosis and treatment, miRNAs could play an important role. The recent discovery of circulating miRNAs has opened the possibility to study this class of biologically active agents as modes of inter-cellular information flow as well as biomarkers of disease. (Kinet, et al., 2013)

Subsequently, it became evident that miRNAs can be exported from cells (Figure 3A), and are found in most extracellular biological fluids, including saliva, urine, tears, and breast milk. Extracellular miRNAs are unexpectedly stable, and must be protected from degradation, as naked RNA is readily targeted by exonucleases that are present in various extracellular fluids. (Kinet, et al., 2013) Indeed, miRNAs are packaged in microparticles such as exosomes, microvesicles, and apoptotic bodies, or are associated with RNA-binding proteins, including Argonaute 2 (Ago2) or lipoprotein complexes like the high-density lipoprotein (HDL), as depicted in Figure 3. The vesicular packaging or protein association of the miRNA confers its stability even upon exposure to severe conditions that would induce prompt degradation of free RNA, such as extreme pH, high temperatures and prolonged storage. (Empel, et al., 2012)

Exosomes are small (40–120 nm) extracellular microvesicles arising from the exocytosis of multivesicular bodies. They are produced by a multitude of cells, including epithelial cells, hematopoietic cells, endothelial cells and tumour cells. Exosomes can serve as carriers for miRNAs and have been identified in most circulating body fluids. Some miRNAs can be either more or less expressed in donor cells or in the secreted exosomes, suggesting the existence of cellular mechanisms that actively concentrate specific miRNA species in exosomes. (Kinet, et al., 2013)

Microvesicles or shedding microvesicles are another form of small, defined vesicles that are shed from the plasma membrane by a wide variety of cells. They are larger (0.1–1 µm) than exosomes and are produced by budding of vesicles from the plasma membrane. (Kinet, et al., 2013)

Another vesicular form where miRNAs reside are apoptotic bodies, byproducts of apoptotic cells. Apoptotic or dying cells release membrane vesicles into the extracellular environment via bleeding of the plasma membrane. These are larger particles (1–5 µm) with a heterogeneous shape. (Empel, et al., 2012).

From the total circulating miRNA, 80 % are by-products of dead cells and exist in a non-vesicle form, protein-bound. (Empel, et al., 2012) Proteins shown to be associated with circulating miRNAs, aiding in the formation of highly stable complexes, are nucleophosmin 1, a nuclear protein involved in ribosomal processing, and proteins from the Argonaute family, especially Ago2, which are components of the RISC, as explained in section 1.2.2. (Kinet, et al., 2013) (Empel, et al., 2012)

Recently, it was shown that HDL can also transport endogenous miRNAs. HDL particles have an average size of 8 to 12 nm, which makes them substantially smaller than exosomes. Furthermore, they contain lipids, such as phosphatidylcholine, that are known to form stable ternary complexes with nucleic acids. How HDL is loaded with miRNAs is not known exactly, but biophysical studies suggest that HDL simply binds to extracellular plasma miRNA through divalent cation bridging. (Creemers, et al., 2012)

The stability of miRNAs in the circulation raises the intriguing possibility that they are taken up by distant cells to regulate their gene expression (Figure 3B). One of the well-described functions of microvesicles and exosomes is to promote communication between the cells from which they are derived and their surrounding environment. Depending on the cell type from which these particles originate, they carry a range of bioactive molecules such as proteins, DNA, RNA, and miRNAs. (Creemers, et al., 2012) Currently, the potential function of extracellular miRNAs is being studied intensively, and it has been confirmed that miRNAs may indeed function in cell-to-cell communication and that miRNAs in microparticles may mediate the repression of critical mRNA targets in distant recipient cells. (Creemers, et al., 2012)

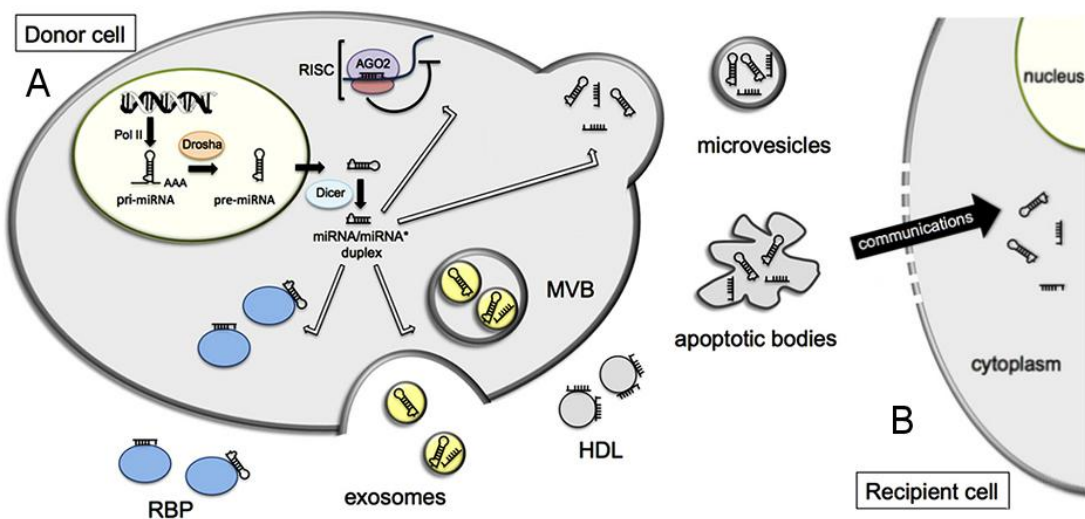


Figure 3 – Biogenesis and release of miRNAs from a donor cell (A). Extracellular miRNA is protected from degradation due to loading into microvesicles, exosomes, apoptotic bodies or due to the association with high-density lipoprotein (HDL) or other miRNA-binding protein complexes (RBP). Extracellular miRNAs can be transferred to recipient cells where they modify gene expression (B).

Adapted from (Kinet, et al., 2013).

1.2.4. Association with Disease and Possible use as Biomarkers

The use of miRNAs as biomarkers is the greatest motivation for the development of a POC platform for its detection and measurement, and thus, it represents the inspiration for this thesis. Initially, the correlation between miRNAs and different pathologic conditions was studied in tissue samples from the diseased organ, but since the discovery of circulating miRNAs in body fluids, there has been a growing interest in miRNAs as biomarkers. miRNA profiles have been associated with a range of diseases and conditions and are currently a subject of study.

miRNAs can act as oncogenes (oncomirs) or tumour suppressors and are involved in a variety of pathways deregulated in cancer. (Almeida, et al., 2011) The first demonstration of a link between circulating miRNAs and cancer came from studies published in 2008. In a study investigating serum from 60 patients with diffuse large B cell lymphoma, a significant increase in levels of miR-155, miR-21

and miR-210 were found, when compared with controls. (Lawrie, et al., 2008) Patients with high levels of miR-21 were also found to have a longer relapse-free survival. Soon after, a study confirmed that miR-141 levels were able to discriminate between prostate cancer patients and controls. (Mitchell, et al., 2008) Additionally, several miRNAs were detected specifically in the serum of lung or colorectal cancer patients, with a large number common to both groups. (Chen, et al., 2008) In follow-up studies by Chen et al., the levels of miR-25 and miR-223 were increased 5- and 3-fold, respectively, in patients with non-small-cell lung carcinoma whereas let-7a did not change. (Reid, et al., 2011) A number of other studies have focused on colorectal cancer, ovarian cancer, breast cancer, pancreatic cancer, leukemia, gastric cancer and hepatocellular carcinoma, among others. In most of the studies, it was possible to establish a certain miRNA profile for each type of cancer. Surprisingly, in some cases, the miRNA profiles can be more sensitive and/or specific than the current state of the art cancer biomarkers.

Circulating B-type natriuretic peptide and its amino-terminal fragment, N-terminal pro-brain natriuretic peptide, are clinically established diagnostic biomarkers for heart failure. (Kinet, et al., 2013) For patients with acute myocardial infarction, circulating levels of cardiac troponins are considered a gold standard for the early diagnosis of this disease. Unfortunately, elevated levels of cardiac troponins have also been reported in patients with end-stage renal disease, which indicates that this marker lacks specificity for acute myocardial infarction. (Empel, et al., 2012) For atherosclerosis, many biomarkers have been proposed, such as C-reactive protein, interleukins IL-1 and IL-6, apolipoproteins apoA-I and apoB, and fibrinogen. (Kinet, et al., 2013) However, it is not clear whether these new biomarkers are useful predictors of future cardiovascular events and the interest of the scientific community in studying circulating miRNAs as potential clinical biomarkers of CVDs has recently increased. Several studies have reported the use of miRNAs as circulating biomarkers for diagnosis/prognosis of cardiovascular diseases such as ischemic heart disease, stroke, heart failure, hypertension, atherosclerosis and diabetes mellitus, as depicted in Figure 4.

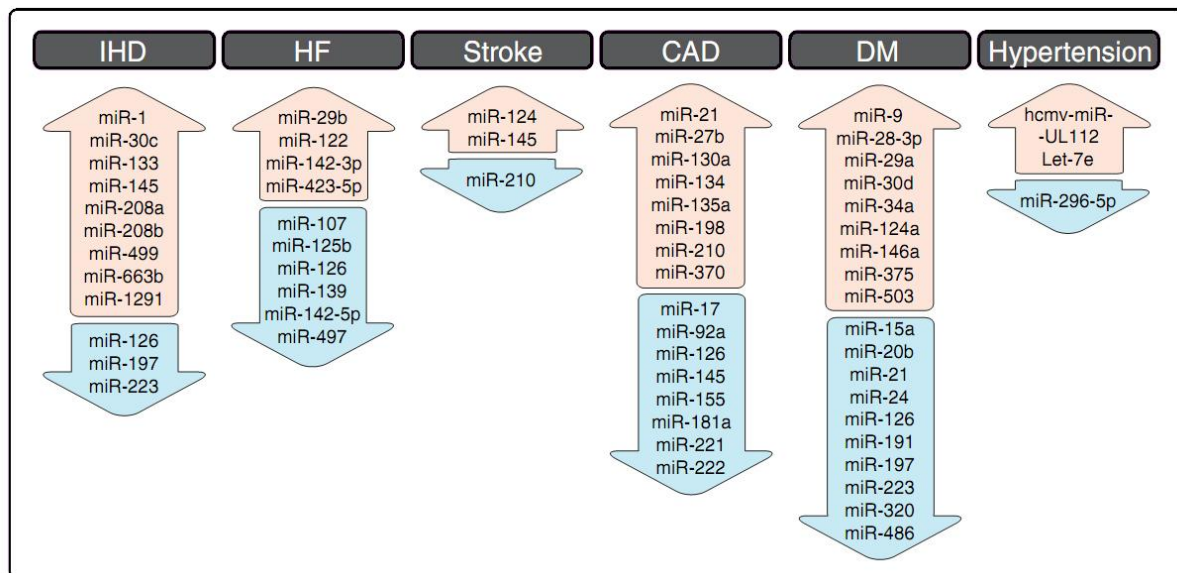


Figure 4 – Overview of the miRNA signatures (overexpression or underexpression of specific miRNAs) that correspond to different CVDs, namely ischemic heart disease (IHD), heart failure (HF), stroke, coronary artery disease (CAD), diabetes mellitus (DM) and hypertension. Adapted from (Empel, et al., 2012).

Other studies point to the fact that oxidative liver injury may also be correlated to specific miRNA patterns, as reviewed by Reid et al., in 2011. Changes in plasma miRNAs were found in a mouse model of drug-induced liver injury. (Wang, et al., 2009) Analysis of liver and plasma samples revealed a number of changes that were for the most part reciprocal: miR-122 and miRs-29a-c all decreased in greater than 5-fold in the liver while increasing 5–500-fold in plasma. Elevated levels of miR-122 and miR-192 in plasma were also more sensitive than alanine aminotransferase enzyme levels, and appeared more rapidly. Other study in a rat model was carried out to determine whether specific circulating miRNAs were able to monitor tissue injury. (Laterza, et al., 2009) Increases in levels of miR-122, miR-133a and miR-124 were found in plasma following injury to liver, muscle or brain, respectively. Unlike aspartate aminotransferase and alanine aminotransferase, plasma levels of miR-122 and miR-133a seemed to discriminate between liver and muscle injury. More recently, yet another work provides the first evidence for the potential use of miRNAs as biomarkers of human drug-induced liver injury. (Lewis, et al., 2011)

A study that sequenced cellular microRNAs identified a miRNA signature of sepsis. (Ma, et al., 2013) Sepsis is a common cause of death in the intensive care unit with mortality up to 70% when accompanied by multiple organ dysfunction. Rapid diagnosis and the appropriate antibiotic therapy and pressor support are therefore critical for survival. After validation, miR-150 and miR-4772-5p-iso were able to discriminate between patients who have systemic inflammatory response syndrome and patients with sepsis. This finding was also validated in independent cohort with an average diagnostic accuracy of 86%. Other study evaluated the diagnostic and prognostic value of miR-150 serum levels in patients with critical illness and sepsis. (Roderburg, et al., 2013) The authors concluded that reduced miR-150 serum concentrations are associated with an unfavorable outcome in patients with critical illness, independent of the presence of sepsis, indicating the potential use of circulating miRNAs as a prognostic marker in critically ill patients.

The presence of pregnancy-associated miRNAs in the maternal circulation has been investigated in two studies reviewed by Reid et al. In the first, miRNAs in the placenta, maternal blood cells and plasma were analysed, and candidate miRNAs were selected based on a 10-fold increased concentration in placenta compared with maternal blood cells, and absence in post-delivery plasma. 17 candidate miRNAs were identified, and the 4 miRNAs present at highest concentration were analysed in maternal plasma. Both miR-141 and miR-149 were found to be significantly reduced post-delivery, and miR-141 levels increased with pregnancy stage. In a second study, 12 miRNAs were present at levels greater than 5-fold increased in the third trimester versus non-pregnant samples. Of these, miR-526 and miR-527 showed a greater than 500-fold increase and together with miR-520d-5p could accurately distinguish pregnant from non-pregnant women.

More recently, miR-323-3p was studied as a candidate biomarker of ectopic pregnancy (EP). (Zhao, et al., 2012) In most pregnancies, the fertilized egg travels through the fallopian tube to the uterus, but in EP, the embryo is fixed within one of the two fallopian tubes, or, in rare cases, in the ovary, abdomen, or cervix, leading to complications. The use of serum human chorionic gonadotropin (hCG) and progesterone to identify patients with EP has been shown to have poor clinical utility. It has been found that the concentrations of serum hCG, progesterone, miR-517a, miR-519d, and miR-525-3p were significantly lower in EP and spontaneous abortion (SA) cases than in viable intrauterine pregnancy

(VIP) cases (Zhao, et al., 2012). In contrast, the concentration of miR-323-3p was significantly increased in EP cases, compared with SA and VIP cases. As a single marker, miR-323-3p had the highest sensitivity for EP (37.0% at a fixed specificity of 90%). In comparison, the combined panel of hCG, progesterone, and miR-323-3p yielded the highest sensitivity for EP (77.8%, at a fixed specificity of 90%), making this biomarker panel extremely promising in the diagnosis of EP.

1.3. State-of-the-Art in microRNA Measurement

The biogenesis of miRNAs, its functions in the cell and possible use of circulating miRNAs as biomarkers of disease have already been addressed on this introduction. It is now pertinent to review the most currently used miRNA detection techniques in order to compare them with the method proposed on this thesis.

The wide range of platforms employed in miRNA isolation and quantification in the studies of circulating miRNAs makes comparing the findings in these studies difficult. It is well acknowledged that there is low correlation of results obtained from different platforms or even from the same platform using products from different vendors, such as microarrays from Agilent and Affymetrix. (Etheridge, et al., 2011) In addition to methodological differences, there is also a lack of consistency regarding the source materials for analysis as well as optimal normalization and quantification strategies. (Reid, et al., 2011) Further research is necessary to address these important points and to bring consensus to this rapidly expanding field.

1.3.1. Main microRNA Profiling Techniques

In general, all miRNA profiling methods can be separated into two categories: one that utilizes direct oligonucleotide hybridization without sample RNA amplification and the other requiring sample amplification. There are inherent advantages and disadvantages to both approaches as protocols that do not perform sample amplification will require a larger starting amount of total RNA, while protocols that require sample amplification could be more prone to handling errors that can also be amplified. (Kong, et al., 2009) Although there is currently no gold standard, there are some mainstream methods to detect and measure the expression levels of miRNAs, all of which face unique challenges: northern blotting (NB), microarray hybridization, quantitative real-time reverse-transcription polymerase chain reaction (qRT-PCR), and next-generation sequencing (NGS). (Git, et al., 2010) (Koshiol, et al., 2010)

1.3.1.1. Microarrays

Microarray technology was developed in 1995, allowing multiple hybridizations to occur in parallel, on a glass or quartz support where antisense probes are immobilized. (Liu, et al., 2008) Depending on the platform used, the probes may be spotted or synthesized by photochemical synthesis. The spotting can be performed using a hand held spotting device (this method is low cost but the spots are macroscopic, the resulting array is relatively large and requires considerable amounts of DNA or RNA to hybridize), or using automated robots. (Kong, et al., 2009) Three different technologies classically exist to detect nucleic acids (DNA or RNA) on an array platform, which were reviewed by Kong et al., in 2009. The first, commonly used for custom arrays, is based on the spotting of unmodified oligonucleotides over poly-lysine coated glass or silanized glass (this coating provides electrostatic immobilization of the probe). The second also uses probe spotting on glass slides, but the distinction is that the 5' terminus of the probe is cross-linked to the matrix on the glass (covalent bonding), which increases the probe density compared to the former. In the last technology, the probes are photochemically synthesized directly on the surface, which is made of quartz.

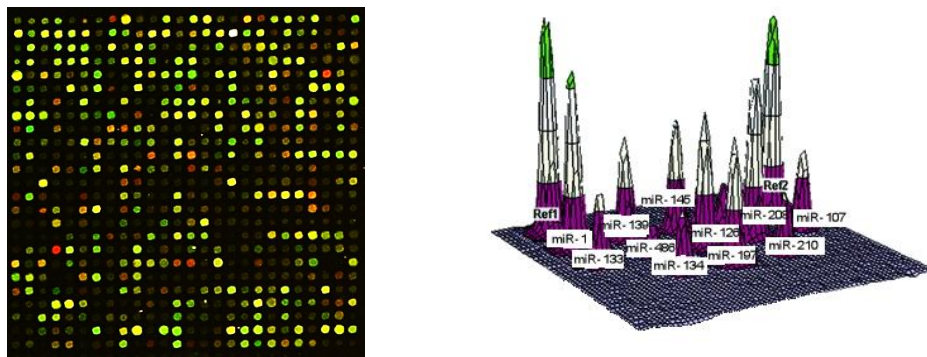


Figure 5 – Microarray fluorescence image and analysis. On the left: example of the output of a microarray experiment (target molecules labelled with red and green fluorescent dyes), adapted from (Reinke, 2006). On the right: Graphical representation of the analysis of a microarray experiment, where different levels of RNA expression, corresponding to different spots, can be distinguished by the height of the peaks, adapted from (FitzGerald, et al., 2005).

An experiment to profile the circulating miRNAs in both healthy and cancerous individuals will now be described. This example was borrowed and adapted from (Conzone & Pantano, 2004). During such an experiment, RNA is first extracted from the samples (source materials will be discussed later) and then labeled with dissimilar fluorescent dyes (the healthy targets can be labeled with a green dye, while the cancerous targets are labeled with red). After labeling, the healthy and cancerous targets are combined and applied to the surface of a DNA microarray, initiating the hybridization process. The labeled targets begin to form strong hybrids with complementary probes that are located on the array surface. Hybridization occurs when the sequences of the target and probe are complementary, resulting in strong hydrogen bonding between the target and probe. Non-complementary targets and probes do not form such strong hybrids and are subsequently removed from the array surface after a stringent

washing. A scanning process is conducted after hybridization and washing to image the red and green dyes, which represent labeled targets that have hybridized with their probe complements on the microarray surface. Spots fluorescing strongly in the green or red channels are indicative of high miRNA concentrations on the healthy or cancerous samples, respectively, while spots exhibiting a yellow appearance indicate minimal difference (see Figure 5 for an example of such a scan). After scanning, the image can be analyzed quantitatively to characterize the differences in miRNA expression corresponding to the healthy and cancerous individuals.

In contrast to mRNA profiling technologies, miRNA profiling must take into account the difference between mature miRNAs and their precursors, and should also distinguish between miRNAs that differ by as little as a single nucleotide. This represents a challenge for the probe design, as reviewed by Yin et al., in 2008, upon which this paragraph is based. In microarrays, either synthetic oligonucleotides or complementary DNA (cDNA) fragments are used as capture probes. An ideal probe should have high specificity and high affinity for the target. Adenine (A)- and thymine (T)-rich probe sequences frequently exhibit lower hybridization intensities than high guanine (G) and cytosine (C) content probe sequences. This happens because A forms a base pair with T by two hydrogen bonds while C forms a base pair with G by three hydrogen bonds, making it more stable. However, the sensitivity of A/T-rich probe sequences in arrays can be enhanced by the introduction of nucleotide analogs that improve the overall duplex stability. Experiments showed that the substitution of deoxyadenosine (dA) and deoxythymidine (dT) in 10 nt probe arrays with the 2'-O-methyl-2,6-diaminopurine and 2'-O-methyl-5-methyluridine analogs could increase the relative hybridization intensity two- to threefold.

The melting temperature (T_m) is the temperature at which half of the DNA strands are denatured as single-stranded DNA (ssDNA). The T_m of miRNA usually varies between 45 °C and 74 °C. (Yin, et al., 2008) If a specific hybridization temperature (e.g. 55 °C) is set for the entire set of miRNAs, capture probes with lower T_m values will yield lower signals, whereas capture probes with higher T_m values will display impaired nucleotide discrimination and lower specificity. To overcome this problem, locked nucleic acid (LNA)-modified capture probes can be employed instead of simple DNA probes. (Castoldi, et al., 2006) An LNA, as explained in detail by Doessing et al., in 2011, is a ribonucleoside homologue that features a 2'-O,4'-C-methylene bridge, which locks the ribose moiety in the C3'-endo conformation, making LNA a RNA mimic. In duplexes, LNA causes a local reorganization of the phosphate backbone. Replacing every third residue or more with its corresponding LNA moiety yields a near-canonical A-form heteroduplex. By pre-arranging the bases for better stacking, the enthalpy loss is increased upon duplex formation, which translates into very high thermal stability of LNA-modified duplexes. Introduction of LNA into the DNA strand of a DNA:RNA duplex has been shown to increase the T_m between 1–8 °C per each LNA moiety incorporated (compared to the unmodified duplex). Modification of the RNA strand in a similar heteroduplex has led to increases in T_m of 2–10 °C per LNA moiety. These results showed that LNA-modified capture probes with normalized melting temperatures were more sensitive than normal DNA capture probes and allowed accurate and sensitive monitoring of the expression of miRNAs without prior need for RNA size fractionation and/or amplification. (Doessing & Vester, 2011)



Figure 6 – RNA (on the left) and LNA (on the right) monomer structures. Adapted from (Doessing & Vester, 2011).

Other authors indicate that the application of 2'-O-(2-methoxyethyl)-modified nucleotides as capture probes could facilitate detection of miRNA. (Beuvink, et al., 2007) In a different study, to balance the Tm, it has been suggested that increasing or reducing the length of probes according to physicochemical traits of the particular miRNA sequence of interest might suffice to provide accurate and sensitive array-based analysis. (Wang, et al., 2007) In addition, to improve the specificity and help distinguish the targeted miRNA from unintended potential targets, Wang et al. showed that a hairpin structure incorporated onto the 5' end of the probe could destabilize hybridization to larger RNAs, such as miRNA precursors.

Besides probes that are complementary to the sense and antisense strands of miRNAs, different control probes are also required. Positive controls are a way to establish parameters that result in successful detection of target RNA. Generally, an oligonucleotide targets a highly expressing RNA (Reid et al. state that some circulating miRNAs are systematically expressed in healthy individuals), ensuring that the target RNA is expressed at the expected levels. Negative controls are crucial for distinguishing sequence-specific hybridization from non-specific effects in the array experiment. A negative control could be an miRNA probe designed to have no known target, or a target that is known not to be expressed in the particular sample being assessed. The use of internal control spots might also help to ensure the quality of the data and can help in calibrating the results of an analysis. Using a target that is complementary to the immobilized internal control probe, the quality of the microarray chip can be assessed. External controls (spike-in control) are RNA molecules that are chemically synthesized in vitro and are added to the biological samples in varying concentrations. The spike-ins can be used to measure the gain or loss of signal during each step of the sample preparation process (including total RNA isolation, fractionation of miRNA, labeling and others) and can address process-related losses of miRNA. Sample size control probes are designed to be complementary to the loop regions of precursor RNAs and are used to identify whether mature miRNAs or their precursors bind to the corresponding probes. In addition to different controls for data quality control, repeated spotting of the same probe on an array has been shown to increase precision of the measurements if the spot intensities are averaged. It can also minimize problems caused by scratches, dust and other mishaps that can contaminate the surface of microarray slides.

Common transcripts that are mutually represented among the various microarray platforms can be used to compare the expression differences between different arrays. This aspect will facilitate cross-platform comparisons of miRNA expression, and potentially lead to robust analyses in clinical miRNA

expression studies. Finally, northern blot and qRT-PCR analysis are frequently used for data normalization, validation and comparison. (Koshiol, et al., 2010)

1.3.1.2. Quantitative Reverse-Transcription Polymerase Chain Reaction

Direct hybridization of samples onto an oligo array may require a large amount of miRNA, but some samples provide only a small and limited amount of RNA. (Kong, et al., 2009) Polymerase chain reaction (PCR)-based approaches have been developed to address this issue. (Schmittgen, et al., 2004)

The first step in the qRT-PCR of miRNAs is the accurate and complete conversion of RNA into cDNA by reverse transcription. This step is challenging since the template (miRNA) has a limited length, there is no common sequence feature to use for the enrichment and amplification of miRNAs, and also the mature miRNA sequence is present in the miRNA precursors. (Benes & Castoldi, 2010) To date, two different approaches to reverse transcribe miRNAs have been utilized. MiRNAs are either reverse transcribed individually by using miRNA-specific reverse transcription primers, or first tailed with a common sequence and then reverse transcribed using a universal primer. The use of miRNA-specific primers (MSPs) decreases background, whereas universal reverse transcription is useful when several different miRNAs need to be analyzed from a small amount of starting material. These reverse transcription alternatives will be compared in the next paragraphs, based on the review by (Benes & Castoldi, 2010)

MSPs can be annealed to miRNAs to prime reverse transcription. The resulting cDNA is then used as a template for quantitative PCR (qPCR) with one MSP and a second universal primer. While the 3'-end of the MSP has to be complementary to the miRNA, there are two different approaches to design the 5'-end of a MSP: with either a stem-loop or a linear structure. Stem-loop primers are designed to have a short single-stranded part that is complementary to the 3'-end of miRNA, a double-stranded part (the stem) and the loop that contains the universal primer-binding sequence. Stem-loop primers reduce annealing of the primer to miRNA precursors, increasing the specificity of the assay. (Chen, et al., 2005) On linear primers, the 3'-end complements the target miRNA, to enable reverse transcription, while the 5'-end of the primer encodes a universal sequence that is used to achieve qPCR amplification. Although linear primers are simpler to design, these may not discriminate between mature and precursor miRNAs.

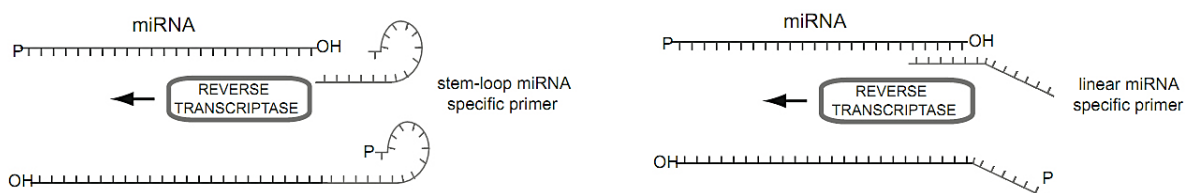


Figure 7 – Reverse transcription of miRNA using specific primers: stem-loop primer (left) and linear primer (right). Adapted from (Benes & Castoldi, 2010).

In an alternative approach, the 3'-ends of miRNAs are elongated to provide them with a common tail. Poly(A) polymerase is used to add, in a template independent fashion, adenosine nucleotides to the 3'-end of RNA. A primer consisting of an oligo (dT) sequence with a universal primer-binding sequence at its 5'-end is then used to prime reverse transcription and to amplify the target sequences in the qPCR reaction. Recently, Benes et al. developed a novel approach to synthesize cDNA from miRNA, named miQPCR, which exploits the activity of T4 RNA Ligase 1 (single-stranded RNA ligase) to covalently attach the 3'-hydroxyl group of mature miRNAs to the 5'-phosphate group of a RNA/DNA linker adaptor, which in turn contains a universal primer-binding sequence. The extended miRNAs are then reverse transcribed by using a universal primer complementary to the 3'-end of the linker. According to the authors, using T4 RNA ligase1 may increase the specificity, sensitivity and the efficiency of reverse transcription and of qPCR. (Benes & Castoldi, 2010)

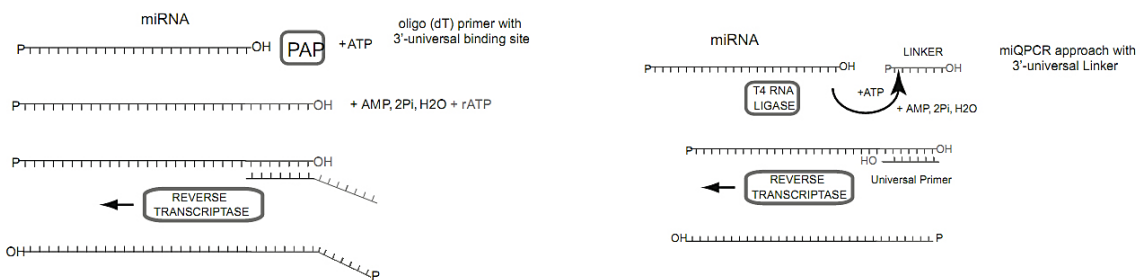


Figure 8 – Universal reverse transcription of all the mature miRNAs contained in the sample by enzymatic tailing of the miRNAs by using Poly(A) Polymerase (left) or T4 RNA Ligase (right) Adapted from (Benes & Castoldi, 2010).

The specificity and sensitivity of qPCR assays are dependent upon primer design. (Benes & Castoldi, 2010) The miRBase database can be used to analyze the sequence of the miRNA under evaluation, with important factor to consider being the GC content and the existence of closely related family members. As discussed in section 1.3.1.1, individual miRNAs have highly heterogeneous GC content, which results in a large interval of predicted Tm against the primer. If the predicted Tm is high (e.g., >65 °C), then shortening the length of the primer can be used to increase specificity. (Benes & Castoldi, 2010) However, if the predicted Tm between the MSP and the target sequence is low, then the inclusion of LNA moieties or other nucleotide analogues on the primer should be considered (the use of LNA and other nucleotide analogues was already discussed in section 1.3.1.1).

In conventional PCR, the amplified DNA product (amplicon) is detected after a given number of amplification cycles (after the reaction has finished), by visualizing the DNA product on an agarose gel. In contrast, in qRT-PCR, the accumulation of amplification product is measured as the reaction progresses, that is, in real time, with product quantification after each cycle. (Bio-Rad Laboratories, s.d.) The amount of amplification product is monitored, in real-time, by the detection of a fluorescent reporter molecule whose signal intensity correlates with the amount of DNA present in each cycle of amplification. (Benes & Castoldi, 2010) A number of fluorescent technologies exist for performing qPCR, such as SYBR Green I, TaqMan probes, Molecular Beacons, Light Upon eXtension (LUX) and

HybProbes (LightCycler), however, to date only SYBR Green I (SG) and TaqMan probes have found application to miRNA detection. (Benes & Castoldi, 2010)

SG is an intercalating dye with favorable photophysical properties, temperature stability, selectivity for dsDNA and high sensitivity. SG assays for the quantification of dsDNA in solution can be optimized to result in easy, robust and reliable one-step procedures that display a dynamic linear range of up to four orders of magnitude using a single dye solution. (Zipper, et al., 2004) Importantly, SG cannot discriminate between different PCR products and binds to all dsDNA, including non-specific products such as primer-dimers. This limits the accurate detection of the target sequence and requires methodologies that assess the specificity of the amplification products. (Benes & Castoldi, 2010) A melting point analysis, also referred to as a dissociation curve analysis, is frequently used to monitor the homogeneity of the qPCR products. During this procedure, the fluorescence intensity emitted by SG intercalated into PCR products is recorded at temperatures rising in small increments. This temperature rise gradually denatures dsDNA, inducing a consequent reduction of the fluorescent signal, which appears as a sharp drop in signal intensity when both strands separate completely. (Shi & Chiang, 2005) As the T_m of a DNA duplex is dependent upon length and base composition, the number of points of inflection in the melting curve indicates the number of PCR products (including the primer-dimers) generated. An acceptable dissociation curve has a single peak (one PCR product), while the occurrence of multiple peaks indicates the presence of non-specific amplification products. (Benes & Castoldi, 2010)

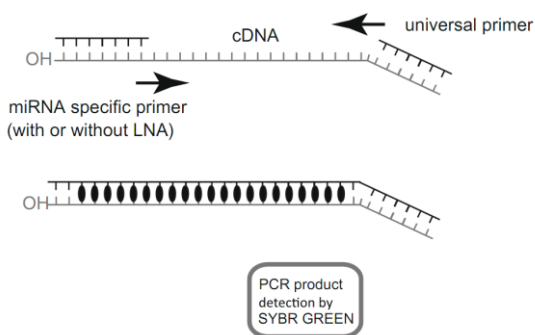


Figure 9 – Detection of the amplicon by the use of the SYBR Green intercalator. Adapted from (Benes & Castoldi, 2010).

Another possibility to detect amplification products is the use of dual-labeled hydrolysis probes, known as TaqMan probes. TaqMan probes, which are designed to hybridize to an internal stretch of the amplicon, have a reporter dye attached to the 5' end and a quencher dye attached to the 3' end. (Biosoft, 2014) The close proximity of the fluorescent reporter to the quencher molecule prevents the emission of fluorescence. Taq polymerase extends the outside primer and then reaches the 5' end of the TaqMan probe, where upon the 5' → 3' exonuclease activity of Taq polymerase hydrolyses base by base the TaqMan probe, and in consequence the fluorescent probe is no longer in close proximity to the quenching group. This results in an increase of fluorescence that is proportional to the amount of PCR products generated, allowing accurate quantification of the amplified target. (Benes & Castoldi, 2010) Importantly, even if primer-dimers or other non-specific amplification products form, they will not generate any fluorescent signal.

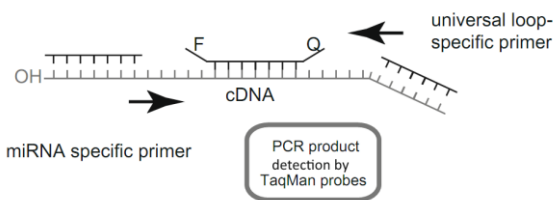


Figure 10 – Detection of the amplicon by TaqMan probes. Adapted from (Benes & Castoldi, 2010).

Comparison of miRNA expression between different samples requires standardization and normalization. As numerous variables inherent to a qRT-PCR experiment need to be controlled in order to differentiate experimentally induced variation from true biological changes, the use of multiple reference genes is accepted as the gold standard for qRT-PCR data normalization. (Mestdagh, et al., 2009) In the case of miRNA profiling, only few candidate reference miRNAs have been reported: miR-191 and miR-103, among others, were found to be highly consistent in their expression across 13 normal tissues and five pair of distinct tumor/normal adjacent tissues. (Peltier & Latham, 2008) Generally, other small noncoding RNAs are used for normalization, including small nuclear RNAs (U6, for example) and small nucleolar RNAs (U24 and U26, for example). (Mestdagh, et al., 2009) However, it has been suggested by Mestdagh et al. that the use of the mean expression value of all expressed miRNAs in a given sample as a normalization factor for miRNA qRT-PCR data outperforms the currently adopted approach based on small nuclear/nucleolar RNAs in terms of better reduction of technical variation and more accurate appreciation of biological changes

The major advantages of qRT-PCR over microarrays are the sensitivity of the qPCR assays, a considerably larger dynamic range compared to microarray analysis and a convenient requirement for low amounts of starting material (in the range of nanograms of total RNA). (Benes & Castoldi, 2010) However, the analysis of known miRNAs expression using qRT-PCR is both time and reagent consuming. Recently, different approaches to perform parallel reverse transcription for a large number of miRNAs contained in a single sample have been reported, bringing the possibility of high-throughput analysis. (Tang, et al., 2006) (Moltzahn, et al., 2011) (Chen, et al., 2009)

It is considered good practice to profile miRNAs by microarray followed by validation with qRT-PCR. (Koshiol, et al., 2010) However, there are no standard guidelines for conducting and reporting such validation. For example, some authors report validation by qRT-PCR for some miRNAs and by Northern blot for other miRNAs, or report validation of precursor but not mature miRNAs. (Koshiol, et al., 2010) Furthermore, there is no standard as to which internal control should be used for the normalization of qRT-PCR, which can result in erroneous conclusions, as discussed above. Standardized guidelines would aid the interpretation of miRNA data by creating transparency in reporting.

1.3.1.3. Northern Blotting

The NB technique was developed in 1977, with the purpose of transferring electrophoretically separated RNA species to a solid support (diazobenzyloxymethyl-paper) and detecting specific species by hybridization with radioactive complementary DNA or RNA. (Alwine, et al., 1977) This classical technique is shortly described on this sub-chapter because many studies still use it as a reference technique for validation, as mentioned before.

A typical NB protocol for the separation and identification of miRNAs is as follows. (Tran, 2009) First, total RNA is isolated from the sample. Typically, 10 µg of total RNA are prepared in 2 X TBE urea sample buffer. The samples are heated at 70 °C for 5 min and loaded onto a 15% (w/v) polyacrylamide gel containing TBE-urea. The application of a high percentage gel is critical for the separation of both the precursor and mature miRNA sequences. Then, electrophoresis is performed on the gel (a typical voltage is 180 V, with a run time between 60–90 min) in order to separate the RNA samples by size. After electrophoresis, the gel is rinsed and RNA is transferred onto a nylon membrane (1.5 hours at 20 V). The nylon membrane is exposed to UV light or baked (80 °C for four hours), allowing the cross-linking of the RNA to the membrane. The membrane can be probed immediately or stored at -20 °C until needed. A DNA probe is designed to be complementary to the mature miRNA of interest, and then the probes are 32P radiolabelled by end labelling using the forward reaction with T4 polynucleotide kinase (chemiluminescence may be used for detection instead of radioactivity). A prehybridization step may be performed. The probe is added to the prehybridization solution and the membrane hybridized for at least 2 hours at 37 °C with rotation. The membrane is then washed and exposed to a phosphorimaging screen. The image of the RNA bands on the membrane is then acquired and processed (Figure 11).

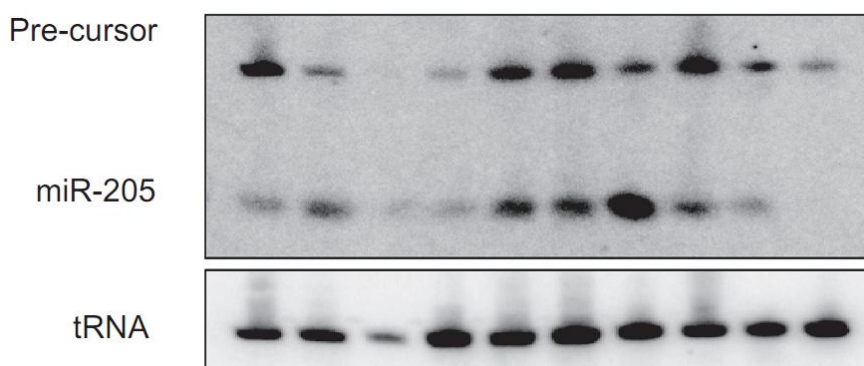


Figure 11 – Detection of mature and pre-cursor miR-205 using NB. tRNA_{val} is used as a RNA loading control. Adapted from (Tran, 2009).

NB detection for examining single gene miRNA expression and validating array and qRT-PCR results is a well-established and reliable method. (Tran, 2009) (Schmittgen, et al., 2004) However, NB as a tool to profile the expression of miRNAs is finding less and less use due to the development of

more sensitive, high-throughput techniques, such as the qRT-PCR and the microarrays. (Schmittgen, et al., 2004) An advantage of NB is that it allows the determination of the size of an RNA at the same time that it provides information on the expression level. Furthermore, the probes designed to hybridize to the mature miRNA also detect the pre-miRNA simultaneously on the blot. (Schmittgen, et al., 2004) In addition, the membrane can be stripped and re-probed for the expression of a different miRNA gene (usually, the membrane can be used 3 times before the quality of the RNA is compromised). (Tran, 2009) The use of pre-cast gels reduces reagent preparation time and provides consistency in the small RNA (sRNA) separation, and if a small transfer unit is used to transfer the RNA from the gel to the membrane, there is a significant reduction in the volume of reagents needed. (Tran, 2009)

1.3.1.4. Next-Generation Sequencing

Platforms such as microarray and qRT-PCR can only identify known sequences, which makes them good miRNA profiling tools but with little utility for miRNA discovery. NGS allows both discovery of new miRNAs and confirmation of known miRNAs in a high-speed, high-throughput fashion without the need for gels or the ambiguity in data interpretation inherited by other methods. (Koshiol, et al., 2010)

The history of DNA sequencing started in 1977, when Frederick Sanger developed a DNA sequencing technology based on the chain-termination method (also known as Sanger sequencing), and Walter Gilbert developed another sequencing technology based on chemical modification of DNA and subsequent cleavage at specific bases. (Sanger, et al., 1977) (Maxam & Gilbert, 1977) Because of its high efficiency and low radioactivity, Sanger sequencing was adopted as the primary technology in the first generation of laboratory and commercial sequencing applications. At that time, DNA sequencing was laborious. (Liu, et al., 2012)

The milestones of NGS development were shortly reviewed by Liu et al., in whom this paragraph is based. After years of improvement, Applied Biosystems introduced the first automatic sequencing machine, AB370, in 1987, based on capillary electrophoresis. AB370 could detect 96 bases one time, 500 kb a day, and the read length could reach 600 bases. The current model, AB3730xl, can output 2.88 M bases per day and read length could reach 900 bases since 1995. The human genome project greatly stimulated the development of powerful novel sequencing instruments to increase speed and accuracy, while simultaneously reducing cost and manpower. Following the human genome project, 454 was launched by 454 in 2005, and Solexa released Genome Analyzer the next year, followed by SOLiD provided from Agencourt. These are the three most typical NGS systems, sharing good performance on throughput, accuracy, and cost, compared with Sanger sequencing. These founder companies were then purchased by other companies: in 2006 Agencourt was purchased by Applied Biosystems, and in 2007, 454 was purchased by Roche, while Solexa was purchased by Illumina. At the present day, these are still the manufacturers of the three most used platforms for NGS, which are compared on Table 1. (Liu, et al., 2012) (Koshiol, et al., 2010)

The Illumina Genome Analyzer system currently is the most widely-used, short-read sequencing platform. (Liu, et al., 2011) It applies the sequencing-by-synthesis method. After reverse transcription of the miRNAs, the DNA samples are randomly sheared into fragments, then ligated to oligonucleotide adapters at both ends. Single-stranded DNA fragments are attached to reaction chambers and are extended and amplified by bridge PCR amplification with fluorescently-labeled nucleotides for sequencing.

The 454 Genome Sequencer uses the principle of pyrosequencing. (Koshiol, et al., 2010) Sheared DNA fragments are ligated to specific oligonucleotide adapters and are amplified by emulsion PCR on the surfaces of agarose beads. (Liu, et al., 2011) The current maximum read length of the 454 platform is 600 bp, which is the longest short-read among all of the NGS platforms. Thus, the 454 Genome Sequencer FLX is best suited for applications requiring longer reads.

The Applied Biosystems SOLiD sequencer uses the sequencing-by-ligation approach. It amplifies sheared DNA fragments by an emulsion PCR approach with small magnetic beads. It may offer the best data quality, but the DNA library preparation procedures prior to sequencing currently take five days which is both tedious and time consuming. (Liu, et al., 2011)

Table 1 – Comparison of the main next-generation sequencing platforms. Based on (Liu, et al., 2011).

Platform	Technology	Amplification	Read Length	Mbases/run	Time/run	Comments
Illumina	Sequencing-by-synthesis	Bridge PCR	35-150 bp	1300 Mb	4 days	Most widely used
Roche 454	Pyrosequencing	Emulsion PCR	400 bp	100 Mb	7 hours	Longer reads, fast run, higher cost
SOLiD	Ligation-based sequencing	Emulsion PCR	75/35 bp	3000 Mb	5 days	Good data quality

A NGS experiment generates huge amount of sequence data. The key process in NGS data analysis is to align the huge amount of short reads to a given genome. A variety of algorithms and software packages have been specifically developed for dealing with millions of NGS short-read alignments. When it comes to NGS data analysis for expression profiling of miRNAs, the base idea is to align the NGS short reads to a known reference sequence database. The most important and popular miRNA databases include miRBase, deepBase, microRNA.org, miRGen 2.0, miRNAMap, and PMRD. There are several web servers (such as miRAnalyzer and miRCat) and standalone programs (such as miRDeep and miRExpress) for miRNA expression profiling and novel miRNA discovery. (Liu, et al., 2011)

The comparison of NGS expression analysis with different microarray platforms points to a higher sensitivity in the detection of transcripts with low expression and higher expression changes by the sequencing approach. (Motameny, et al., 2010) Cross hybridization effects do not occur and even fragments that differ by a single nucleotide can be distinguished by NGS, in contrast to microarray or qRT-PCR experiments. miRNA family members and precursors can be easily identified by NGS. Sequencing is independent of predesigned probes, thus making it very suitable for the discovery of new

miRNAs. Nevertheless, deep sequencing is a relatively novel approach and the associated computational analysis tools are still in their infancy and need to be improved to standardize normalization, mapping and thresholding. (Motameny, et al., 2010) To ensure sufficient light signal intensity for accurate detection of each added nucleotide, NGS methods typically amplify the fragments through emulsion PCR or library generation followed by PCR-based cluster amplification. (Koshiol, et al., 2010) However, amplification can result in sequence errors and some sequences may be preferentially amplified, limiting the ability to accurately quantify relative abundance. (Willenbrock, et al., 2009) These methods can also be less accurate in areas of identical bases. (Koshiol, et al., 2010) Other limitation of NGS is the high cost of instruments and reagents, although each sample can be bar coded, allowing samples to be mixed and run simultaneously to reduce cost. A third generation of sequencing technologies currently under development could eventually provide lower cost options. To end this sub-chapter regarding miRNA profiling techniques, Table 2 summarizes the main features of the three most used techniques: microarrays, qRT-PCR and NGS. For circulating miRNA profiling, qRT-PCR is the most suited given the lower amount of starting material required.

Table 2 – Summary of the main features of microarrays, quantitative real-time reverse transcription PCR (qRT-PCR) and next-generation sequencing (NGS) as tools for miRNA profiling and discovery. For more details on the normalization strategies, see (Meyer, et al., 2010).

	Microarray	qRT-PCR	NGS
Principle	Hybridization	PCR Amplification	Sequencing
Throughput	High	Medium to High	Ultra High
Costs	Economic	Economic	Comparatively High
Required Amount of DNA	100 ng - 10000 ng	10 ng – 700 ng	250 ng - 10000 ng
Data Generation	Up to more than 2 days	1 day	Up to more than 1 week
Limit of Detection	10^{-15} mol - 10^{-18} mol	10^{-22} mol	10^{-15} mol
Dynamic Range	10^3 - 10^4	10^5	10^4 - 10^7
Time Expenditure on Data Analysis	Moderate	Low	High
Memory Capacity Requirements	Low	Low	High
Preferential Application	Relative and absolute quantification of miRNA; miRNA biomarker identification; routine application	Relative and absolute quantification of miRNA; validation of other miRNA profiling approaches	De novo identification of sRNAs; simultaneous relative quantification of different sRNA transcripts; picturing the sRNA transcriptome
Examples of Normalization Strategies	Quantile; LOESS; Variance stabilization; Invariant-based; Scaling (Z-score, mean, median, etc)	Invariant-based (e.g. stable reference small non-coding RNAs); Plate normalizing factor; Global mean expression	Quantile; Trimmed mean of M values

1.3.2. Source Material for Circulating microRNA Profiling

Human tissue is the source of material for miRNA expression profiling. Important variables in tissue processing include tissue procurement, fixation, embedding, and RNA extraction method. In the scope of this thesis, in which a novel POC miRNA detection technique is proposed, the miRNA source of interest is blood, given the low invasiveness for its collection.

Human plasma and serum are commonly used matrices in biological and clinical studies, but they are not identical. The use of the wrong matrix (plasma in place of serum or vice-versa) can lead to improper diagnosis. (Yu, et al., 2011) Both plasma and serum are derived from full blood that suffered different biochemical processes after blood collection. If the blood sample is withdrawn in the presence of an anticoagulant, such as EDTA, heparin or sodium citrate, and centrifuged to remove cellular elements, a plasma sample is obtained. In the absence of anticoagulant, the blood clots and it can be centrifuged immediately to remove the fibrin clot and cellular elements or allowed to stand for period of time so that clot retraction occurs, allowing the serum extraction. (Lundblad, 2003)

Serum is qualitatively different from plasma in that the bulk of the fibrinogen has been removed by conversion into a fibrin clot, together with the platelets, which have been either physically bound in the fibrin matrix, or activated to form aggregates, or both. Varying amounts of other proteins are also removed into the fibrin clot. (Lundblad, 2003) With regard to miRNA, there is evidence that higher miRNA concentrations are found in serum samples compared to the corresponding plasma samples. (Wang, et al., 2012) The higher RNA concentration in serum suggests that RNA may be released from cells during the coagulation process due to stress or cell lysis. Also, the platelets were found to contain significant amounts of RNA, which might also be released into the serum during the coagulation process. (Wang, et al., 2012) Plasma may be the sample of choice in studying circulating miRNAs, since RNA released during the coagulation process may change the true repertoire of circulating miRNA. However, if PCR-based techniques are to be used, serum may be best suited, given that the proteins present in plasma may interfere with the amplification process.

1.3.3. Storage, Preparation and Enrichment of microRNAs

After the sample collection and plasma or serum preparation according to standard protocols, the miRNAs are extracted prior to profiling. The storage and preparation of miRNAs from samples are crucial for expression analysis. (Yin, et al., 2008)

Issues related to the miRNA stability and storage were reviewed by (Schöler, et al., 2010). In contrast to other RNA molecules, mature miRNAs seem to exhibit high stability in the circulation system. Even after incubation at room temperature for up to 24 hours, miR-15b, miR-16, and miR-24 were detectable in serum without any obvious degradation. Furthermore, isolated miRNAs are not affected by different storage temperatures, as investigated for storage at -20 °C and -80 °C. Even under extreme conditions, endogenous miR-15b, miR-16, and miR-24 conserved their high stability, and multiple

freeze-and-thaw cycles did not impair their structure. However, these findings do not exclude variations in stability within the various miRNA species, as only a few miRNAs were tested. To minimize variability in miRNA-level detection caused by biases that can be easily avoided, a standardized protocol should be used. Several factors should be matched in study design: type of collection tube, time interval between blood collection and serum preparation, and choice of anticoagulants, as heparin, for example, interferes with PCR. (Schöler, et al., 2010)

One of the major challenges in miRNA or total RNA purification is the large amount of soluble proteins in plasma and serum, possibly interfering with hybridization- or PCR-based miRNA quantification techniques. (Schöler, et al., 2010) A standardized miRNA purification protocol would simplify comparisons between different experiments. First, the total RNA is extracted from the sample, using a spin column based kit like miRVana (Ambion) and miRNeasy (Qiagen), which allow also the preparation of the sRNA fraction, or, alternatively, TRIzol preparation following ethanol precipitation. (Motameny, et al., 2010) For removing remaining proteins, several groups performed one or more additional phenol/chloroform extraction steps with or without proteinase K incubation. (Schöler, et al., 2010) Standard column based RNA preparation kits, common for mRNA preparation, should be avoided because this normally leads to the loss of smaller RNA molecules. (Motameny, et al., 2010)

The direct use of total RNA to profile miRNA expression can limit sensitivity because the relative abundance of sRNAs in a total RNA sample is ~0.01%. (Yin, et al., 2008) miRNA features low molecular weight and low abundance, and hence miRNA enrichment is an important step for the expression measurement. Several methods have been established that addressed sRNA enrichment, as reviewed by (Yin, et al., 2008). One method uses the new technology of ion pair reverse-phase chromatography, which has been shown to selectively enrich and separate the less abundant sRNAs from the more abundant higher molecular weight ribosomal RNA (rRNA) species. Ambion Inc. developed the mirVana™ miRNA Isolation Kit and a rapid column gel electrophoresis (flashPAGE™ Fractionator), Invitrogen created the PureLink™ miRNA Isolation Kit, and Millipore developed the Microcon1 YM-100 for sRNA enrichment.

In addition, sRNAs may be isolated from total RNA using conventional denaturing gel electrophoresis. It is useful to not only isolate the sRNAs because, in this case, the rRNA fraction cannot be used for an RNA integrity analysis. It is essential to confirm the quality of the RNA before profiling to make sure that degradation products do not influence the results. To extract the miRNA fragments from the total RNA, a size selection can be performed: the total RNA is run on an agarose gel and the band corresponding to the size of miRNAs is cut out for further processing. This procedure excludes all bigger fragments, including all mRNAs and also rRNAs from the samples. (Motameny, et al., 2010) Concentration and quality of RNA is also frequently assessed by absorbance spectrometry. (Kruhøffer, et al., 2007) (Patnaik, et al., 2012)

Using the techniques above described, RNA molecules of ~200 nucleotides and less can be efficiently purified from the larger RNA species and sRNAs <40 nucleotides can also be highly enriched. These tools have proved invaluable for characterizing miRNA processing, facilitating the detection of miRNAs and avoiding the interference from larger RNAs. (Yin, et al., 2008)

1.4. Microfluidics and Lab-on-a-Chip

After reviewing the aspects related to the analyte (miRNA) as well as the state of the art techniques for its detection and concentration measurement, the subject of microfluidics will now be introduced. This subject is of high relevance given that the work of this thesis uses a microfluidic approach towards the development of a lab-on-a-chip (LOC) device for POC detection of miRNAs.

1.4.1. Introduction to Micro Total Analysis Systems

It has been more than 20 years since the first micro total analysis systems (μ TAS) papers were published. Initial reports of these devices, which are also commonly referred to as LOC, labchips, microchips, or microfluidic devices, generally focused on separations and the development of a variety of functional elements for sample manipulation and handling. (Culbertson, et al., 2014) One of the greatest potentials of μ TAS, however, has always been in the integration of multiple functional elements to produce truly sample-in/answer-out systems. In the past decade, the march toward developing such integrated devices has accelerated significantly. Many μ TAS reported now are quite sophisticated with multiple sample handling and processing steps that are highly integrated and often automated. μ TAS have found a major niche in the areas of biological and biomedical analyses, especially cellular and nucleic acid analysis. This focus on biological applications reflects the capabilities of these devices to precisely and accurately handle picoliter volumes of materials and to integrate cell transport, culturing, or trapping with reagent delivery and on-chip detection. (Culbertson, et al., 2014)

One of the greatest challenges in modern medicine is the ability to provide accurate diagnostic laboratory tests in developing countries and in remote areas where conventional analytical laboratories are lacking. Imagine running a clinic in a remote area of rural Africa, the Canadian Arctic, on a military field base or even in a small rural community in Ontario and having the ability to provide accurate, rapid, POC diagnostic lab tests without the infrastructure of a full analytical laboratory! As futuristic as this idea seems, the application of microfluidics engineering to the development of medical diagnostic tests is very much a reality. (MacPherson & Ravichandiran, 2011)

The study of fluid motion in microsystems is denoted as microfluidics. (Bruus, 2008) There are several advantages of scaling down standard laboratory setups by a factor of 1000 or more, from the decimeter scale to the 100 μ m scale. One obvious advantage is the dramatic reduction in the amount of required sample. A linear reduction by a factor of 10^3 amounts to a volume reduction by a factor of 10^9 , so, instead of handling 1 L or 1 mL a LOC system can easily deal with as little as 1 nL or 1 pL. Such small volumes allow for very fast analysis, efficient detection schemes, and analysis even when large amounts of sample are unavailable. To handle small volumes, it is possible to develop compact and portable systems that might ease the use of bio/chemical handling and analysis systems tremendously. (Bruus, 2008) Examples of such devices are depicted in Figure 12. Significant work, however, is still needed for most of these platforms in terms of substrate materials, miniaturization or elimination of external fluidic control elements, chip-to-real-world interfacing (integration), detection, and throughput.

Finally, the development of label-free detection technologies remains of interest. (Culbertson, et al., 2014)

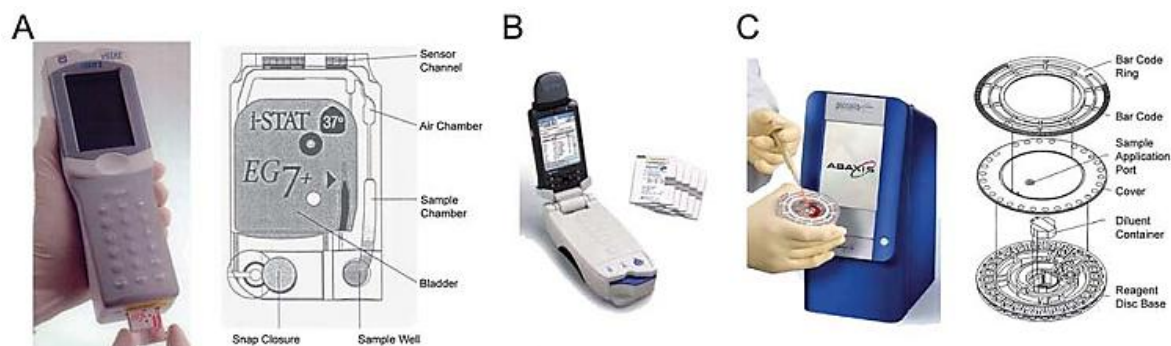


Figure 12 – Pictures and schematics of examples of microfluidic-based POC platforms: (A) i-STAT (Abbott), (B) Epochal and (C) Abaxis. Adapted from (Chin, et al., 2012).

1.4.2. The Main Functional Modules

One of the key advantages of μ TAS is the ability to integrate multiple functional elements into a single compact device, such as pumping, flow control, filtering, separation, concentration and detection.

Fluid flow and control in microfluidic channels is of particular importance. There are many methods to generate fluid flow in μ TAS, including external pumping and active or passive on-chip pumping methods. Most pneumatic pumping schemes require the use of off-chip pressure sources and solenoid valves. External syringe pumps may also be used. Moving some of that equipment on-chip has significant advantages in terms of finer flow control and better multiplexing. Redox-magnetohydrodynamics is an interesting method of generating pumping on-chip, but requires the use of high concentrations of redox species in order to work well and this can limit the applications for which it can be used. (Weston, et al., 2010) The use of molecular motors to drive flow on nano- and microfluidic devices is an alternative due to their small size, but there are important constraints imposed by sample composition and device design that apply to both kinesin–microtubule and actomyosin driven applications. (Korten, et al., 2013) An alternative is to rely on passive pumping to control fluids. There is some skepticism that passive capillary flow can actually be used for well-controlled assays involving the use of multiple channels and sequential processing steps. Such capabilities, however, were recently demonstrated successfully. (Novo, et al., 2013) Another possibility is to isolate fluids in poly(dimethylsiloxane) (PDMS) microcompartments, in which the pressure of the liquid is stored in the elastic deformation of the walls and ceiling of the compartments. Fluids can be stored under pressure in these structures for months and when the valves are opened, the walls and ceiling push the fluid out of the compartments into microfluidic channels. Other alternative for fluid flow in microfluidic devices is to spin the device, generating a centrifugal force. The general limitation with such devices is that the fluid always flows toward the edge of the disk. Finally, the electroosmotic pumping mechanism offers a number of advantages such as creation of constant pulse-free flows and elimination of moving parts. The flow rates and pumping pressures match well with those needed in μ TAS and the common materials

and fabrication technologies make it readily integrateable with LOC devices. (Edwards, et al., 2007) (Wang, et al., 2009) (Wang, et al., 2014)

Besides flow control and pumping, other functions are usually necessary in order to perform a LOC analysis. Mixing can be an issue in microfluidic devices due to the low Reynolds numbers (laminar flow). A considerable amount of effort has been directed to the development of both passive and active methods to increase the speed of mixing. The ability to generate stable chemical gradients is critical to a variety of biological analyses where concentration effects on cell physiology need to be investigated. The ability to concentrate an analyte in a controlled manner is very important but difficult to implement on microfluidic devices. Filtering can be used to concentrate particles and the ability to select particles based upon size is also crucial to many biologically based μ TAS experiments. As an example, electrophoresis and dielectrophoresis can be used to concentrate and sort charged particles or dielectric particles, respectively, from the bulk of the fluid. (Puchberger-Enengl, et al., 2011) (Kuczenski, et al., 2011)

The ability to perform miniaturized chemical analysis is only useful if the analytes can be detected at analytically or clinically relevant levels. A wide variety of detection techniques have been reported, as reviewed by (Culbertson, et al., 2014). Electrochemical detection is of particular interest with μ TAS because electrodes and detection electronics can be miniaturized and have low power requirements. Amperometric detection is the most popular electrochemical technique integrated with microfluidic devices. Other hypothesis is the use of standoff detectors, as they do not have to make physical contact with the analyte in order to detect it. Capacitively coupled contactless conductivity detectors are examples of standoff detectors with a variety of potential analyte, cell, particle, and droplet detection applications. Impedance detectors are also very commonly used biosensors because of their compact nature and minimal power requirements. Optical interrogation techniques are frequently used for the detection of analytes on μ TAS devices, especially fluorescence techniques, due to their high selectivity and sensitivity. Fluorescent labels are typically small molecules or proteins that can be excited at a particular wavelength and emit at a longer wavelength. Their use is common in biology and chemistry due to the simplicity of the method, but their drawbacks include potential pH sensitivity and susceptibility to photobleaching over time. (Rivet, et al., 2011) For example, fluorescent lifetime and FRET approaches may be used. Fluorescent lifetime measurements were shown to improve the data quality compared to intensity-based approaches. In other applications, fluorescently tagged aptamers interact with the target, causing the release of the quencher, resulting in increased fluorescence. For some compounds, direct detection is inconvenient and so indirect detection techniques have been developed. To overcome photobleaching and pH sensitivity issues of traditional fluorescence labels, quantum dots are used to provide better stability and a higher signal. Alternatively to fluorescence, chemiluminescence techniques may be used. Nanoparticles, including magnetic and gold particles coated with antibodies or aptamers can be used as labels for the separation and detection of cells and specific biomolecules. Magnetic particles may be used for cell sorting or trapping and for the detection and quantification of biomolecules. (Rivet, et al., 2011) While the above techniques provide good sensitivity and selectivity, most molecules are either not fluorescent or difficult to label and, therefore, label-free detection techniques are highly sought after. (Culbertson, et al., 2014)

1.4.3. Considerations on the Fabrication of Microfluidic Devices

PDMS is by far the most popular material for the fabrication of microfluidic devices due in most part to easy fabrication and low cost. PDMS devices are commonly molded against a SU-8 (photoresist) template. However, PDMS is quite hydrophobic and difficult to wet, will absorb hydrophobic analytes, can be toxic to some cell types, and generates a low electroosmotic flow. (Culbertson, et al., 2014) As such, considerable effort has been invested in developing coatings for PDMS to modify its surface properties.

While PDMS is the most common microfluidic substrate material, a variety of other materials is also used. Glass, while more expensive than PDMS in both materials and processing costs, still has some advantages in terms of known surface chemistries, transparency, and high thermal conductivities. Glass devices are generally fabricated using a combination of photolithographic and wet-etching processes followed by thermal annealing to form closed channels, but this is a time-consuming process. Other polymers rather than PDMS, such as poly(methylmethacrylate) (PMMA) and cyclic olefin copolymers, are more amenable to high-volume manufacturing techniques, such as hot embossing and injection molding. Polystyrene devices are likely to become more popular in the near future for cell-based assays because the interactions between polystyrene and cells are well understood and biologists are more comfortable using the material. For highly corrosive materials, special polymers such as poly(vinylidene fluoride) must be used. (Culbertson, et al., 2014)

Most microchip fabrication methods require the substrate containing the microchannel manifold to be bonded to a nonpatterned flat substrate in order to form sealed channels. Microfluidic bonding techniques may be categorized as either indirect or direct, as reviewed by (Tsao & DeVoe, 2009). Indirect bonding involves the use of an adhesive layer (glue or UV-cured adhesive resins) to seal the two substrates and encapsulate the microchannels while direct bonding methods mate the substrates without any additional materials added to the interface. Direct bonding may consist of thermal fusion bonding, solvent bonding, localized welding or surface treatment and modification. In thermal fusion bonding, polymer substrates are heated to a temperature near or above the glass transition temperature of one or both of the substrate materials, while applying a pressure to increase mating contact forces. Solvent bonding of thermoplastics takes advantage of polymer solubility in selected solvent systems to achieve entanglement of polymer chains across the interface. Localized welding consists on the use of ultrasounds, microwaves or infrareds to deliver energy to induce heating and softening at the interface of the mating parts. Finally, surface treatment and modification may be performed in order to increase the surface energy, improving the wettability between mating surfaces, enabling more intimate contact and enhancing mechanical interlocking and interdiffusion of polymer chains between the surfaces. Surface treatment may be achieved by solvent or acid treatments, plasma treatments, UV exposure or UV/Ozone treatment. (Tsao & DeVoe, 2009)

1.4.4. Review of microRNA Detection on Microfluidics

Some of the efforts towards miRNA profiling in microfluidics consist on the miniaturization and automation of conventional laboratory techniques (e.g. qRT-PCR), with low novelty regarding detection principles. For example, it was shown that miRNA expression profiling and validation are possible using a high throughput qRT-PCR method in microfluidics. (Jang, et al., 2011) The authors compared miRNA expression levels measured by the Fluidigm 96.96 Dynamic Array with those obtained from the Affymetrix miRNA GeneChip. Fluidigm Dynamic Array integrated fluidic circuits have an on-chip network of microfluidic channels, chambers, and valves that automatically assemble individual PCR reactions, decreasing the number of pipetting steps required by up to 100 fold. (Fluidigm Corporation, 2014) Using the same platform, other authors have identified diagnostic and prognostic miRNA signatures in serum of prostate cancer patients. (Moltzahn, et al., 2011) A different platform, but with similar philosophy, is the febit's Geniom miRNA Biochip and the Geniom RT Analyzer, which enable minimally invasive, automated patient miRNA biomarker profiling from easily accessible clinical samples such as blood. (Lange, 2010) The Microfluidic Primer Extension Assay allows the direct use of sample RNA without prior treatments. Following the application of isolated sample RNA, the labelling step is performed on-chip, with the Klenow fragment of DNA polymerase I added directly into the channels of the Geniom Biochip for specific elongation and labelling of hybridized miRNAs.

Other approaches take advantage of the microfluidic scale phenomena (e.g. laminar flow), leading to the development of original ideas for the detection of biomolecules in microfluidic systems. Recently, a new method for rapid and sensitive miRNA detection from a small sample volume, using a power-free microfluidic device, driven by degassed PDMS, has been published. (Arata, et al., 2014) The incubation time was shortened because the device conveyed sample molecules right straight to the surface-immobilized probe DNAs by hydrodynamic force. Two key technologies were tested: one relies on sandwich hybridization, while the other is based on laminar flow-assisted dendritic amplification, which increases the fluorescent signal by supplying two amplification reagents from laminar streams to surface-bound molecules. Utilizing both technologies, miRNA detection was possible with a 0.5 pM detection limit from a 0.5 µL sample corresponding to 0.25 attomoles, with a detection time of 20 min.

Microfluidics have also proven to be an interesting platform for cell studies. For example, relative miRNA changes have been studied at single cell resolution using a 10-chamber microfluidic chip platform. (Wu, et al., 2013) Flow fluorescent in situ hybridization using locked-nucleic acid probes was combined with rolling circle amplification to detect the presence and localization of miRNA. The biggest advantage was the capability to multiplex the detection of miRNAs with protein immunostaining in the same cell, and preserve the cell-to-cell heterogeneity within the population.

Electrokinetic phenomena can play important roles in microfluidics, as they can be applied to fluid pumping, separation processes and detection. One such application is a two-stage hybridization assay that detects let-7a miRNA in 15 minutes, with single-nucleotide specificity, while processing only 5 ng of total RNA. (Garcia-Schwarz & Santiago, 2013) This assay uses isotachophoresis (ITP) to speed up hybridization kinetics between target molecules and fluorescent reporters, and a photopatterned functionalized hydrogel to purify reaction products following hybridization. ITP is an electrokinetic

technique that uses a heterogeneous buffer system, composed of leading (LE) and trailing (TE) electrolytes, to perform more than 10 000-fold focusing. ITP is utilized to extract, mix, and preconcentrate RNAs and reporters from the TE reservoir and into the focused ITP zone (at the LE–TE interface), where they hybridize at high concentration. Following hybridization, the ITP zone migrates into a purification region that contains a hydrogel decorated with capture oligonucleotides complementary to the reporters. Unhybridized reporters bind to the capture probes and become immobilized, while reporters hybridized to microRNAs remain focused in ITP and can be detected downstream (reporters are labelled with a fluorophore to allow for optical detection).

A different application of electrokinetics is the measurement of streaming currents or potentials inside a microchannel, rather than using fluorescence detection. Fluorescence detection techniques require the labelling of the target molecules (miRNAs) with fluorophore molecules (or quantum dots) or, alternatively, the use of sandwich hybridization schemes (miRNAs hybridize with a capture probe immobilized on the surface and then a fluorescently labelled reporter probe is run) or the inclusion of intercalators in the probe-target hybrid. Besides, the optical detection system may be expensive and difficult to integrate with the microfluidic chip. Thus, the use of a label-free, microfluidic-integrated detection technique is highly desirable. In a work developed at INESC-MN's facilities, label-free electrical detection of surface DNA immobilization and hybridization via streaming current measurements were demonstrated. (Martins, et al., 2011) Streaming currents generated by the flow of deionised water through a PDMS microchannel sealed on glass were measured using integrated Au electrodes. This technique was sensitive to the density and polarity of the charge on the channel surface, allowing the recognition of DNA hybridization and distinguishing between assays with complementary and non-complementary DNA strands. Later, more experiments with integrated miniaturized electrodes were performed. (Martins, et al., 2013) The experiments using solutions with different salt concentrations and different electrode materials showed that the measured electrical current depends on the electrode material and in general differs from the real value of the streaming current. An equivalent circuit model was proposed, as well as potential sources of error that can affect the streaming current measurements and suggestions on how to correct the measured values. These works on streaming currents in microfluidics, measured with integrated, planar, polarizable electrodes constitute the foundation of the work of this thesis.

1.5. The Goals of This Thesis

It was demonstrated by Martins et al., in 2011, that it is possible to use streaming currents for the detection of ssDNA target hybridization to ssDNA probe immobilized on a microchannel wall. However, these streaming current measurements were performed with deionized (DI) water, which is a very stringent condition for the probe-target hybrid, leading to the loss of captured target during the readings. Later, it was explained how to perform streaming current measurements with saline solutions, but this was not applied to the detection of DNA hybridization. The main goal of this thesis was to explore the transient streaming current measurements in microfluidic channels for the detection of DNA hybridization, with the motivation and long-term goal being the miRNA detection in physiological concentrations (fM).

In parallel with the streaming current measurements, fluorescence measurements were performed at each step of the protocol. Inspired by the thesis of (Silva, 2013), differently labelled probe and target oligonucleotides were utilized. By using a probe and a target labelled with different fluorophores, it was possible to assess both the probe immobilization and target hybridization at each step of the experiments.

Different probe immobilization schemes were to be tested, namely electrostatic and covalent immobilizations. After the target hybridization, the streaming current (and fluorescence) measurements were performed with phosphate buffer (PB). The PB concentration was optimized in order to yield the best complementary/non-complementary signal ratio.

Other goal was the determination of the limit of detection of the streaming current detection system. To improve the detection of lower target DNA concentrations and to try to lower the limit of detection, different surface blocking agents were tested and static incubation conditions were compared with flow incubation conditions. In addition, to better characterize the system, the density of probe and target DNA molecules on the surface were estimated.

Finally, important suggestions for the improvement of the system are presented. These suggestions go towards an integrated system that accepts a blood sample, processes it, preconcentrates the analytes and performs the detection, using an on-chip, non-mechanical pumping system. All this should be easily integrateable with an electronic system for control, processing and result readout.

2. Electrokinetics in Microfluidics

The streaming current (or the streaming potential), which will allow the detection of the hybridization of the target DNA, is one of the four electrokinetic phenomena that are often considered in microfluidics, as shortly resumed by (Bruus, 2008). Electrophoresis is the movement of a charged surface relative to a stationary liquid, induced by an applied electric field. Electroosmosis is the movement of liquid relative to a stationary charged surface, induced by an applied electric field. Sedimentation potential is the electric potential created when charged particles are made to move relative to a stationary liquid. Streaming potential is the electric potential created when a liquid is made to move relative to a charged surface.

2.1. Historic Background

(Abaza, 1966) described and cited the authors behind the discovery of electrokinetic phenomena, which were observed as far back as the beginning of the 19th century. In 1808, Reuss (cited by (Abaza, 1966)) discovered that flow through a capillary element can be induced by the application of an electric field. About half a century later, in 1852, Wiedmann performed a number of quantitative experiments and stated that the volumetric flow transported through porous materials by galvanic current is directly proportional to the intensity of the applied current. In 1859, Quincke discovered the phenomena of streaming potential which is the converse of electroosmosis. His experiments showed that when fluid was forced through a diaphragm, the voltage developed across the diaphragm was proportional to the pressure differential causing the flow. Those previous findings, together with the development of the hydrodynamic and electric theories, led to the basic theoretical treatment by Helmholtz and what is known in Colloidal Science as Helmholtz theory.

In 1879, Helmholtz developed the double layer theory which related the electrical and fluid flow parameters of electrokinetic transport. In 1910, Gouy introduced a more realistic concept of the potential and charge distribution in the fluid adjacent to the solid wall. In 1921, Smoluchowski reinvestigated the theory of Helmholtz. In 1924, Stern suggested a type of double layer which is a combination of the simple Helmholtz fixed layer with the Gouy diffuse layer. From that time on, the field of electrokinetics received contributions from many scientists and research workers, especially those in the field of Colloidal Science who gave valuable information on the electrochemical double layer.

2.2. The Origin of the Surface Charge

When discussing electric phenomena inside a microchannel, first of all, there is the question of the origin of the surface charges. Most materials gain a surface electric charge when they are brought into contact with an aqueous solution. This may be due to one of the following reasons (Li, 2004): ions

of different signs may have different affinities for two phases, or there may be the ionization of surface groups when brought into contact with the fluid.

If ions of different signs have different affinities for two phases, it may be due to the distribution of anions and cations between two immiscible phases, or due to the preferential adsorption of certain type ions (from an electrolyte solution) to a solid surface. For example, surfactant ions specifically adsorbed on a surface result in a positively charged surface if the surfactant is cationic, and a negatively charged surface if the surfactant is anionic. Also, the differential solution of one type of ion over the other may occur: when ions dissolve preferentially, leaving a negatively or positively charged surface.

The second possibility for the development of surface charge is the ionization of surface groups (Li, 2004). If a surface has acidic groups (e.g., COOH on the surface), the acidic groups dissociation (e.g., COO^- on the surface and H^+ in the aqueous solution) will result in a negatively charged surface. If a surface contains basic groups (e.g., OH on the surface), the dissociation of the basic groups (e.g., release of the OH groups in the aqueous solution) will generate a positively charged surface. In both cases, the magnitude of the surface charge depends on the acidic or basic strength of the surface groups and on the pH of the solution. Decreasing pH will reduce the surface charge for a surface containing acidic groups. Increasing pH will reduce the surface charge for a surface containing basic groups. The surface charge can thus be reduced to zero (isoelectric point). For example, most metal oxides can have either positive or negative surface charge depending on the bulk pH.

The substrates employed in the current work are glass and PDMS. Glass acquires a negative charge when in contact with water mainly due to the dissociation of silanol groups (Grier, 2001):



Additionally, after the treatment used to seal the glass against the PDMS surface, the inner surface of the channel will be negatively charged by hydroxyl groups at the surface.

2.3. The Electric Double Layer

As explained before, the solid surface will acquire a charge when in contact with the liquid phase. In the case of glass in contact with DI water, it will be a negative charge. The solution is electrically neutral, having an equal number of cations and anions. However, due to the surface charge at the solid phase, a number of oppositely charged ions (counterions) will be attracted to the region near the surface (electrostatic attraction) and the ions of the same charge (coions) will be repelled away from the surface, which results in a positive net charge in this region. The concentration of counterions decreases with the distance from the surface while the coion concentration increases with the distance from the surface. In the bulk of the solution, far from the surface, the counterion and coion concentrations are the same and the resulting charge is zero. In the case of glass, because the surface acquires negative charge, the counterions are positively charged. The surface charge in the solid phase is

balanced by the counterions in the liquid phase. Electric double layer (EDL) is the name usually given to the charged surface of the solid plus the balancing counterion layers in the liquid.

The counterions closer to the surface charges will be strongly attracted to the surface, forming a layer (compact layer) that is immobile (see Figure 13). As the distance from the surface increases, the electrostatic attraction is weaker, making these counterions mobile (diffuse layer). The boundary between the compact and the diffuse layer is usually referred to as the shear plane. Usually, the liquid velocity is considered to be zero at this plane. The surface potential is difficult to measure, but the potential at the shear plane, which is called the zeta (ζ) potential, is often considered as an approximation to the surface potential.

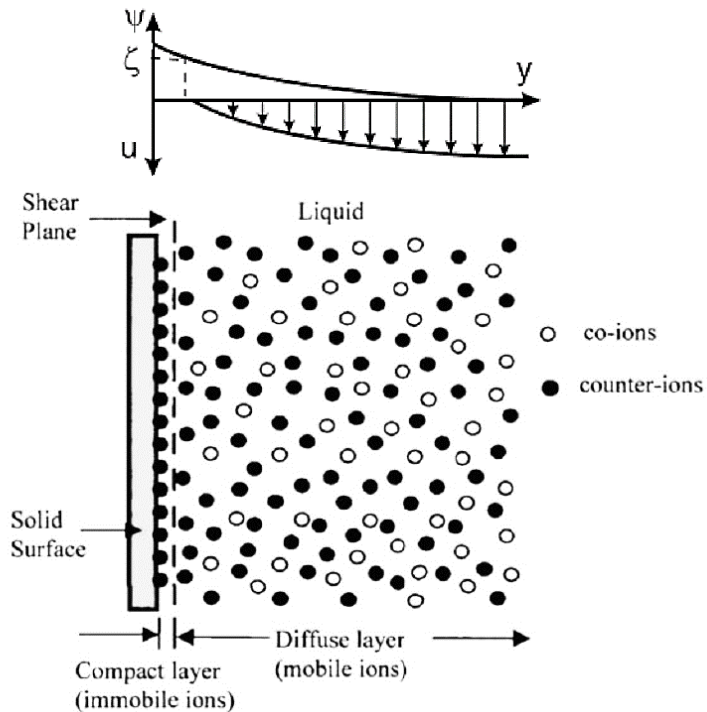


Figure 13 – Potential (Ψ) and flow (u) profiles as a function of the distance (y) from the solid surface (top) and representation of the respective electric double layer in the vicinity of a flat surface (bottom).

Adapted from (Li, 2004) and (Kirby & Hasselbrink, 2004).

2.4. Streaming Current and Potential in Microfluidics

Since the diffuse layer (Debye layer) has a net charge density, if a flux is established inside the microchannel, it will drag the mobile counterions, generating a net current known as streaming current. The streaming current is usually measured by an ammeter with very low internal resistance connected to two electrodes, one at the inlet and the other at the outlet of the microchannel. The current induced by the flow is given by:

$$I_S = \int_A \rho \vec{u} dA \quad (2)$$

where the integral is taken over A, the cross-sectional area of the microchannel. \vec{u} is the flow profile and ρ is the charge density at the surface. In general, one must solve the Poisson-Boltzmann equation to get ρ and the Stokes equations to get \vec{u} , for each individual geometry. In the limit of Debye-Hückel linearization and Debye layers that are thin compared to channel diameter or height, a simplified approximation is possible. (Kirby & Hasselbrink, 2004) As long as the flow is laminar, the streaming current (I_S) dependency on the pressure drop (ΔP) is given by:

$$I_S = \frac{\varepsilon_0 \varepsilon_r A}{\mu L} \zeta \Delta P \quad (3)$$

where A is the channel cross-section and ζ is the zeta-potential characteristic of the solution and solid in contact. If, instead of closing the external circuit through an ammeter, one connects the electrodes to a voltmeter (with very high internal resistance), the counterions will accumulate at the outlet of the microchannel, developing a difference of potential (streaming potential) between the extremes of the channel. The streaming potential ($\Delta\phi$) is related to the pressure drop (ΔP) by the Smoluchowski equation (Kirby & Hasselbrink, 2004):

$$\Delta\phi = \frac{\varepsilon_0 \varepsilon_r}{\mu \sigma} \zeta \Delta P \quad (4)$$

where σ is the channel conductivity. In a rectangular cross-section microchannel, for a steady, fully developed laminar flow, the pressure drop (ΔP) and the flow (Q) are related via (Sze, et al., 2003):

$$\Delta P = \frac{12 \mu L}{h^3 w} Q \quad (5)$$

where L, h and w are, respectively, the length, height and width of the channel and μ is the dynamic viscosity of the solution. Replacing ΔP by Q in (3) and (4), using (5), the streaming current and potential as a function of the flux (Q) are given, respectively, by:

$$I_S = \frac{12 \varepsilon_0 \varepsilon_r}{h^2} \zeta Q \quad (6)$$

and

$$\Delta\phi = \frac{12 \varepsilon_0 \varepsilon_r L}{\sigma h^3 w} \zeta Q \quad (7)$$

According to (5) and (6), the ζ -potential can be calculated from the slope of the streaming current vs flux or the streaming potential vs flux representations.

In a streaming current experiment, the counterions are constantly being pumped into the inlet and depleted in the outlet (Figure 14). The streaming current flows with the liquid, along the channel, while two other phenomena neutralize it. (Martins, et al., 2013) The first is the faradic current that flows through the electrodes and low impedance external circuit, originated by electrochemical reactions at the electrode surfaces. The second is an ionic conduction current which flows along the microchannel, in the opposite direction of the streaming current, due to the induced electric field in solution acting on the ions inside the microchannel. For charge conservation, the streaming current must be equal to the sum of these two currents.

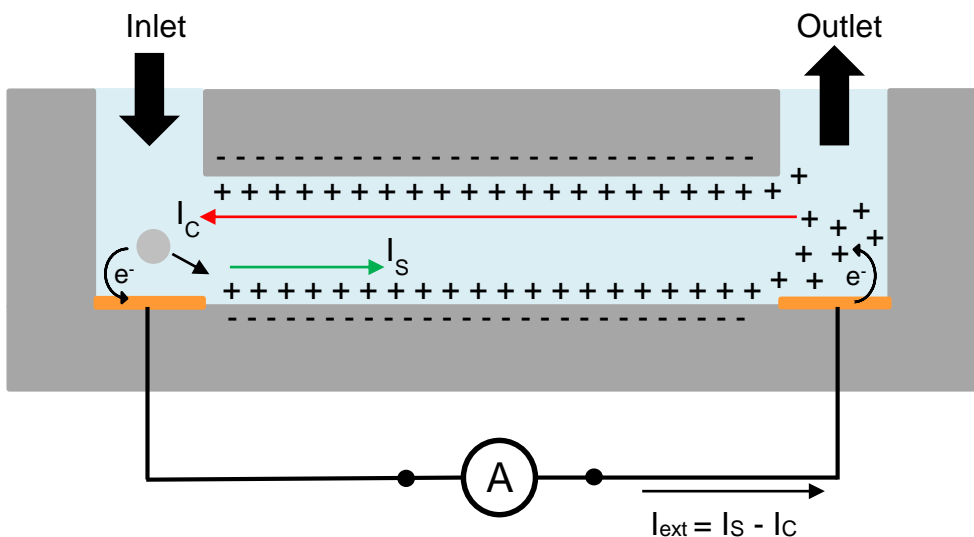


Figure 14 – Schematic of the streaming current (I_s), conduction current (I_c) and external (faradic) current (I_{ext}), established during a streaming current experiment inside a microchannel. For charge conservation, $I_s = I_c + I_{ext}$.

The value of the faradic current, measured by the ammeter, is proportional to the exchange current density, which reflects the intrinsic rates of electron transfer between the analyte and the electrode. This parameter depends on the material properties of the electrode and on the nature of the electroactive species in solution. On the other hand, the conduction current magnitude is inversely proportional to the electrical resistance of the electrolyte inside the microchannel.

Ag/AgCl standard electrodes have a very high exchange current density, hence any imbalance of charge between the microchannel reservoirs instantly induces redox reactions at the electrodes, keeping the solution in the reservoirs neutral. (Martins, et al., 2013) The conduction current is negligible and the faradic current balances perfectly the streaming current. With these non-polarizable electrodes, the external current (faradic current) is equal to the streaming current. The opposite case occurs when streaming current measurements are affected by electrode polarization. Polarizable electrodes have a lower exchange current density. Then, the conduction current dominates over the faradic current. Under these circumstances, the externally measured current is smaller than the streaming current.

The electrode characteristics have an impact on the accurate streaming current measurement. This implies that the current values recorded with an ammeter have to be adequately treated in order to yield the real streaming current values. Such treatment is discussed below, in section 3.5.

3. Experimental Methods

The microdevice fabrication, general experimental methods, equipments used and result treatment principles are described on this chapter. The experimental work was performed at INESC MN's facilities. INESC MN (INESC Microsistemas & Nanotecnologias) is a private, non-profit research and development institute created in January 2002, from the former Solid State Technology group of INESC. INESC MN operates a Class 100/10 cleanroom with optical and e-beam lithography allowing nanoscale device fabrication. The research group in which this project was developed is dedicated to microelectromechanical systems and to the optical detection of biomolecules using microfluidic structures, with the goal of developing LOC devices.

3.1. Solution Preparation

A 1.0 M potassium chloride (KCl) stock solution was prepared by dissolving the salt crystals (Sigma-Aldrich 60130) in DI water from INESC MN facilities. To perform mass measurements, a Scientech SA 80 analytical scale was used. All other KCl solution were prepared by sequential dilution from the stock solution. All PB solutions were prepared from a 1.0 M PB stock (Sigma-Aldrich P3619 potassium phosphate buffer, pH=7.4 at 25 °C), by sequential dilution, using DI water. Phosphate buffered saline (PBS) was prepared by dissolving one tablet (Sigma-Aldrich P4417) in 200 mL of DI water, yielding 0.01 M phosphate buffer, 0.0027 M potassium chloride and 0.137 M sodium chloride, pH=7.4, at 25 °C.

In order to silanize the surface, a 2% (v/v) solution of (3-Aminopropyl)triethoxysilane (APTES) in acetone was prepared from a 99% APTES stock solution (Acros Organics 430941000). The 2% working solution was prepared prior to use and then discarded because the APTES starts to polymerize.

Two surface blocking agents were tested in this work, namely bovine serum albumin (BSA) and salmon sperm DNA. The 2% (w/w) BSA solution in PBS was prepared from a Sigma-Aldrich A7906 stock. The BSA solution was stored at 5 °C and used for several experiments. The salmon sperm DNA working solution, with 100 µg/ml concentration, was prepared by dilution of the 10 mg/ml stock (Stratagene Sonicated Salmon Sperm DNA, CAT#201190-81) in 100 mM PB. Salmon sperm DNA working solution was stored at -20 °C and thawed prior to use.

3.2. DNA Oligonucleotides

In order to explore the streaming current as a detection method for the hybridization of DNA to electrostatically immobilized DNA probes, synthetic DNA oligonucleotides (synthesized by STAB VIDA Genomics LAB, Caparica) were used as probe, complementary target and non-complementary target (negative control). DNA was used instead of RNA because the former has higher chemical stability. The oligonucleotides were purified with a high performance liquid chromatography (HPLC) technique by the

manufacturer and labeled with fluorescent dyes upon synthesis. This way, the fluorescence readings could be correlated with the streaming current readings. The probe oligonucleotides were labelled with 6-FAM (similar to FITC in both molecular structure and spectral properties), while the target oligonucleotides were labelled with DY560. These fluorophores have distinct excitation and emission bands, and upon the use of proper microscope filters, the probe and target oligonucleotides could be imaged separately, in order to measure the “amount” of probe and target on the surface. FRET effects were neglected. The fluorescence microscope filters employed are described on section 3.6.

For the experiments to be closer to the biomedical application the complementary target sequence corresponds to the mature sequence of miR-122 (hsa-miR-122-5p according to miRBase.org, release 20), an miRNA that is upregulated in cases of liver injury and also in heart failure. The probe is the reverse complementary (antiparallel) sequence of miR-122. For negative control (non-complementary target), the sequence of miR-375 (hsa-miR-375 according to miRBase.org, release 20) was used.

The DNA pellets were suspended in DI water and stored at -20 °C. The working solutions, with different final concentrations, were prepared with PB, by sequential dilution from the stock, aliquoted and stored at -20 °C prior to use. Special care was taken regarding the light exposure of the solutions to avoid photobleaching prior to and during the experiments.

Table 3 – Name, sequence and modifications (Mod.) of the oligonucleotides used in this work.

Oligonucleotide Name	Used as	Sequence	3' Mod.	5' Mod.
miR-122 Probe	Probe	5' - caaacaccattgtcacactcca - 3'	None	6-FAM
miR-122 Target	Complementary Target	5' - tggagtgtgacaatggtgttg - 3'	None	DY560
miR-375 Target	Non-Complementary Target (Negative Control)	5' - ttgttcgttcggctcgctga - 3'	None	DY560

3.3. Surface Functionalization Protocol

The complete, typical protocol used in this work for the functionalization of the inner surface of the microchannels is presented here for clarity, but other variations were also tested (these variations are explained near the corresponding results, on the results section). This protocol is based on the one used by (Martins, et al., 2011).

The surface functionalization provides the microchannel with biorecognition capabilities (Figure 15 illustrates the rationale). An unused channel was washed with DI water at 5 µl/min for 15 min and then a 2% (v/v) solution of APTES in acetone was injected inside the channel and incubated for 2 h, without flow. The APTES reacts with the hydroxyl groups on the surface, forming siloxane covalent bonds. The channel was then washed with acetone for 10 min and DI water for 15 min, both steps at 10 µl/min. The amine group of the APTES ($pK_a \sim 10$) dissociates when in contact with aqueous solutions at pH~7. (Gubala, et al., 2013) The APTES-covered channel will then be positively charged upon contact with the PB and PBS solutions (pH=7.4).

The APTES positive charge is used to electrostatically immobilize the ssDNA probe, given that the DNA backbone, composed of phosphate groups, confers the DNA with a net negative charge. A nucleoside monophosphate has two ionisable hydroxyl groups of $pK_a < 1$. At pH-7, a terminal phosphate group contributes with two negative charges and an internucleoside phosphate diester with one. (Blackburn, et al., 2006) In order to be stable, the DNA interacts with the counterions in solution, which partially shield this negative charge. The ssDNA probe was electrostatically immobilized by injecting a 5 μ M solution of ssDNA probe in the channel and incubating it for 1 h and 30 min without flow. The channel was then flushed with 100 mM PB for 10 min at 5 μ L/min to remove non-immobilized ssDNA probe.

Supposing that the APTES and the probe may not cover the surface completely, a surface blocking agent should be used (BSA, for example). A 2% BSA solution in PBS was inserted in the channel and incubated for 1 h. Afterwards, the channel was washed with PBS for 10 min at 5 μ L/min to remove BSA not bound to the surface.

Finally, the solution containing the ssDNA target (either complementary or non-complementary) was inserted in the channel and incubated for 1 h and 30 min without flow, followed by washing with 100 mM PB for 5 min at 5 μ L/min to remove non-hybridized target.

Usually, both the streaming current and the fluorescence were measured after each of the previously described steps. The methods used for each of these type of measurements are described ahead (sections 3.5 and 3.6)

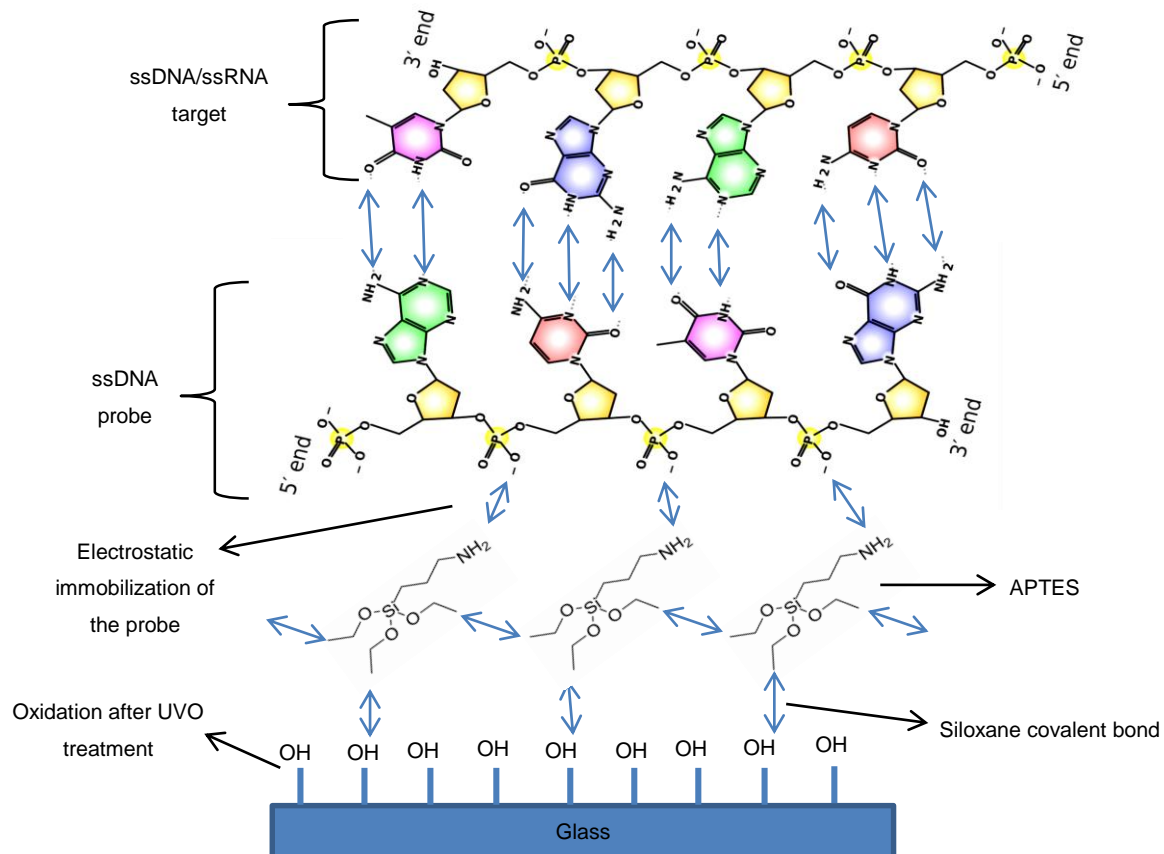


Figure 15 – Surface functionalization protocol illustration.

3.4. Microfluidic Device Fabrication

The fabrication of a microfluidic device for electrokinetic and fluorescence measurements comprised several steps, namely hard mark fabrication, SU-8 mold fabrication, PDMS microchannel fabrication, electrode deposition on glass and, finally, the microfluidic device bonding (sealing) and connection to ancillary devices. These steps will be described on the next subchapters. For detailed step-by-step protocols regarding the microfabrication processes, please refer to the run sheets on the Annexes section.

3.4.1. Hard Mask Fabrication

One easy way to fabricate PDMS microchannels is by casting, using a mould. In this case, the mould consisted of a SU-8 (photoresist) layer patterned with the shape of the microchannels, inlets and outlets. In order to expose and pattern the SU-8 mould, it is practical to use a hard mask because it can be used several times to make moulds when needed. The hard mask fabrication will now be described.

The glass substrate (CORNING), with a thickness of 0.5 mm, was washed for 30 min in Alconox (detergent) solution with ultrasounds, followed by a 30-minute wash in DI water with ultrasounds, both steps at 65 °C. The substrate was then rinsed with isopropyl alcohol (IPA) and blown dry with compressed air.

The next step was the deposition of an aluminium thin film (1000 Å thickness) on the glass substrate (Figure 18, Step 1). This was achieved by magnetron sputtering, using a Nordiko N7000 machine. Electrically neutral Argon atoms are introduced into a vacuum chamber. A DC voltage is placed between the target and substrate which ionizes Argon atoms and creates a plasma in the chamber, consisting of ions and electrons. These Argon ions are now charged and are accelerated to the anode target. Their collision with the target ejects target atoms (aluminium), which travel to the substrate (glass) and eventually settle (Figure 16). Electrons released during Argon ionization are accelerated to the cathode substrate, subsequently colliding with additional Argon atoms, creating more ions and free electrons in the process, continuing the cycle. The plasma is contained near the target (aluminium target) due to a magnetic field.

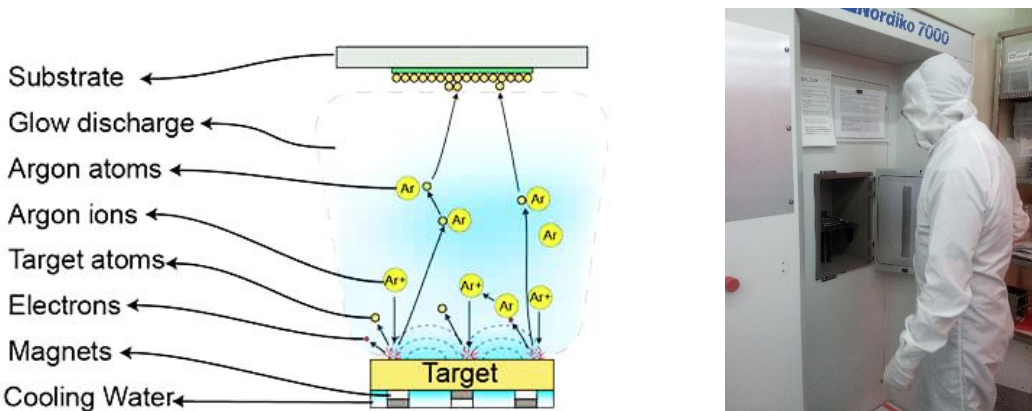


Figure 16 – Basic components of a magnetron sputtering system (left) and Nordiko N7000 deposition system at INESC MN cleanroom (right). Image on the left adapted from (Micro Magnetics, 2014).

After the aluminium deposition on glass, the sample was patterned using lithography. First, the sample was subjected to a hexamethyldisilazane (HDMS) vapour prime to improve photoresist adhesion to the aluminium. The sample was then coated with a 1.5 μm -thick layer of positive photoresist, in a Silicone Valley Group (SVG) automatic track that coated, spun and baked the photoresist on the sample (Figure 18, Step 2). The photoresist was then exposed using a direct write laser (DWL) system in order to pattern the microchannel shape on the hard mask (Figure 18, Step 3). The DWL consists on a motorized stage that moves the sample while a laser unit exposes the sample, point by point. This technique is very practical for prototyping. The areas exposed by the laser were dissolved upon photoresist development (Figure 18, Step 4), which was also performed on the SVG track. The AUTOCAD design of the hard mask, identical to the one used by (Martins, et al., 2011), is depicted in Figure 17.

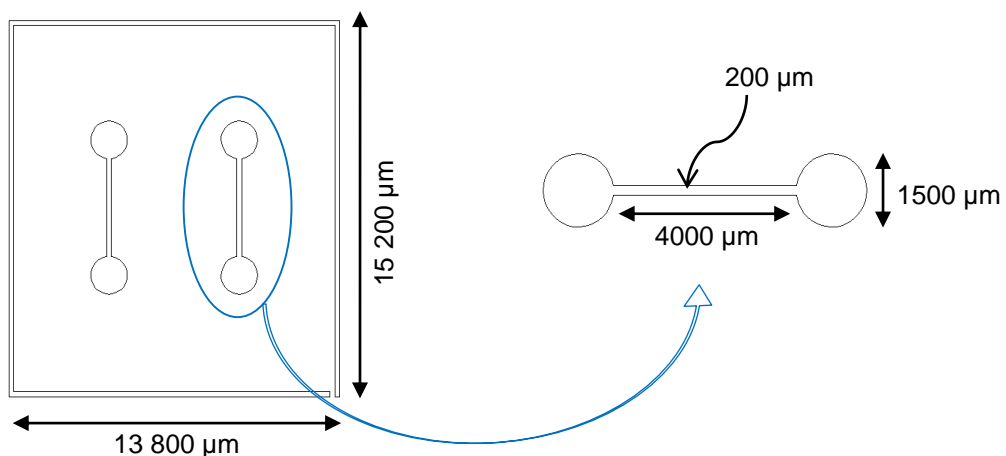


Figure 17 – AUTOCAD design of the microfluidic chip (top view), containing two microchannels (left), and detail of the microchannel (right), including dimensions. Design as by (Martins, et al., 2011).

The last step for the hard mask fabrication was the aluminium wet etch. Wet etching using an aluminium etchant (Technic Aluminium Etchant Micropur MOS) results in an isotropic and selective etching of the aluminium areas not covered by the photoresist (Figure 18, Step 5). After the aluminium dissolution on the intended areas, the photoresist was removed using an appropriate solvent (Microstrip 3001 by Fujifilm) and the hard mask was cleaned with IPA, DI water and blown dry (Figure 18, Step 6). The pictures of the real samples during and after processing are in Figure 19.

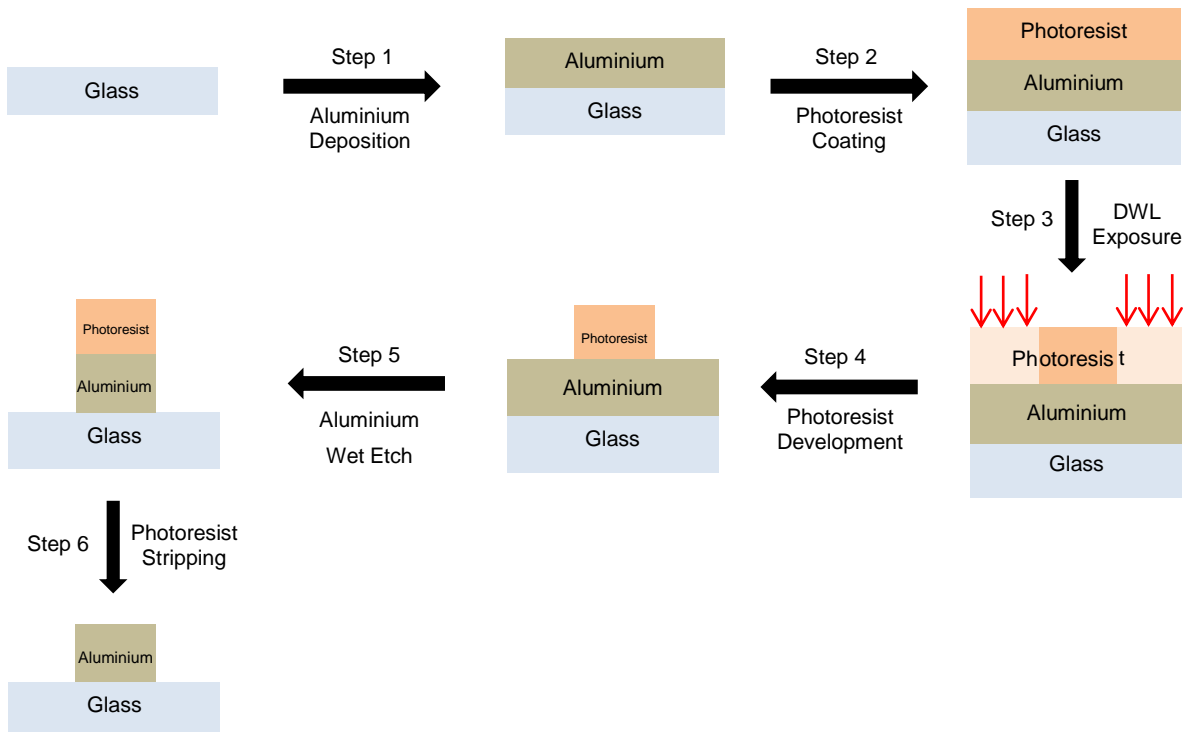


Figure 18 – Hard mask fabrication flowchart (side view). Dimensions of materials not to scale.

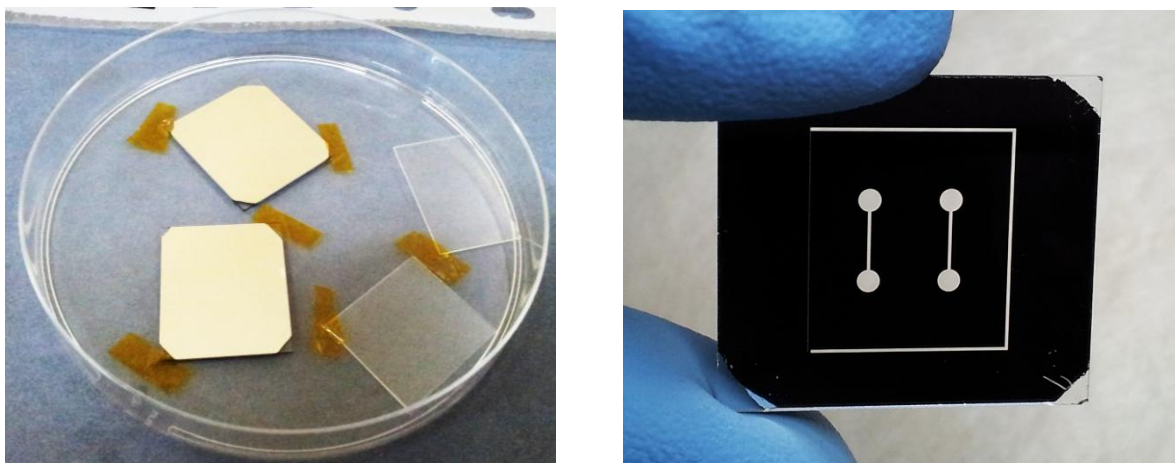


Figure 19 – Glass samples with and without aluminium (left) and complete hard mask with the shape of two microchannels patterned on it (right). This hard mask will be used to expose a layer of SU-8 photoresist and create the mould for the PDMS microchannel fabrication.

3.4.2. SU-8 Mould Fabrication

Using the hard mask previously fabricated, a SU8 (photoresist) mould was defined in order to make it possible to manufacture the PDMS microchannels. A piece of silicon wafer, used as substrate, was cleaned with acetone, alconox, DI water and IPA (similarly to the glass cleaning). SU-8 2015 (MicroChem), which is a negative photoresist, was poured on the substrate and then, using a Laurell WS-650MZ-23NPP/LITE automatic spinner, a uniform layer of photoresist was spread across the substrate (Figure 20, Step 1). The thickness of this layer defines the height of the microchannels (20

μm). The SU-8 was then baked in a Stuart hotplate, mounted below the hard mask and exposed to UV light in order to pattern the shape of the microchannels (Figure 20, Step 2). Upon development with propylene glycol monomethyl ether acetate (PGMEA) (Sigma-Aldrich 484431), the non-exposed areas of the SU-8 were dissolved (Figure 20, Step 3). After rinsing with IPA and baking, the mould was ready to use. Multiple moulds were prepared in order to allow the fabrication of several PDMS devices at once.

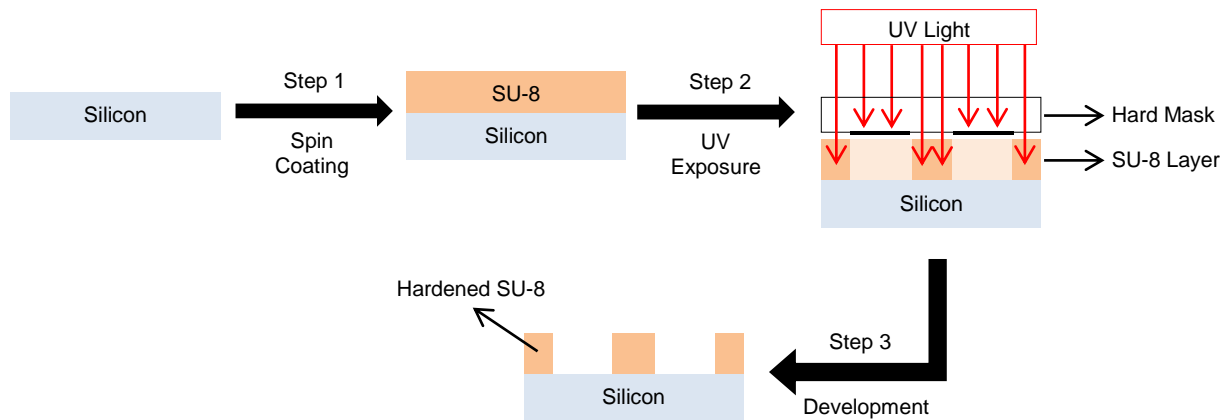


Figure 20 – SU-8 mould fabrication flowchart (side view). Dimensions of materials not to scale.

3.4.3. PDMS Microchannel Fabrication

To manufacture PDMS microchannels, the SU-8 mould was glued to the bottom of a petri dish where liquid PDMS was poured and cured (see Figure 21 for the process illustration). PDMS is an elastomer that is prepared by mixing the base component with the curing agent (SYLGARD® 184 silicone elastomer by DOW CORNING) in a proportion of 10:1 (w:w). After mixing both components thoroughly by hand, the mixture was degassed in vacuum for 40 min to remove air bubbles, poured into the Petri plate/mould and allowed to cure at 70 °C for at least 2 hours in a Memmert oven. The PDMS chip was then cut and separated from the mould (Figure 22). The inlet and outlet holes were manually punched using a blunt end syringe needle, allowing the connection of inlet and outlet tubes and adapters.

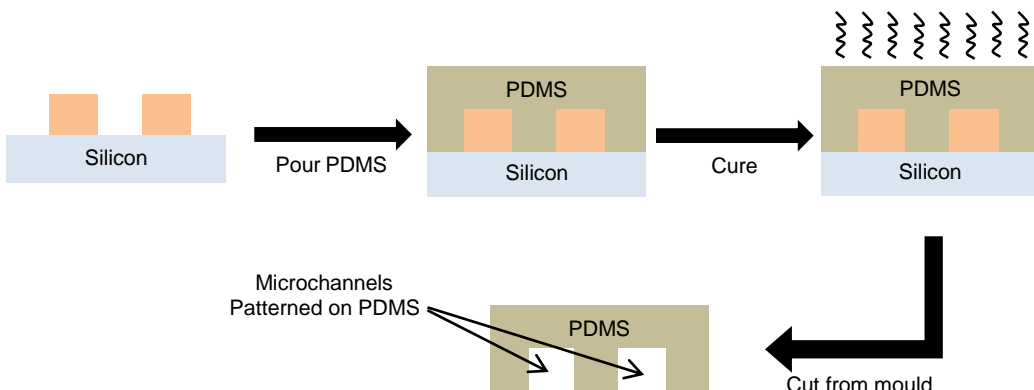


Figure 21 – Flowchart of the PDMS fabrication by casting on a SU-8 mould (side view). Dimensions of materials not to scale.

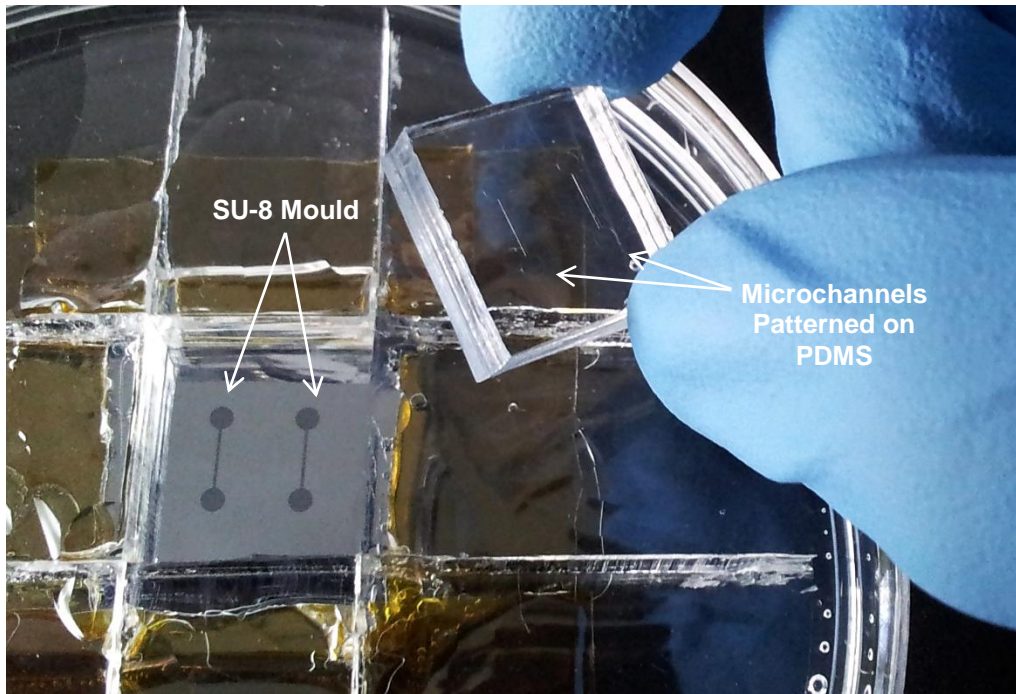


Figure 22 – PDMS chip upon removal from the SU-8 mould. The mould is on the bottom of a Petri plate, the liquid PDMS is poured on top, cured on the oven, and then the PDMS chip is cut from the mould.

3.4.4. Electrode Deposition and Patterning on Glass

The shape of the microchannels was patterned on PDMS, as described previously, but in order to have closed channels where a liquid can flow, there is the need for another surface where the channels can be sealed (bonded) against. In this case, the other surface was glass, where Titanium Tungsten (TiW) planar electrodes were previously deposited. The electrode deposition and patterning are described in this section. TiW was the material of choice given its availability for deposition in the laboratory and because it is less polarizable than gold, making them more suitable for streaming current measurements (Martins, et al., 2013).

As for the hard mask fabrication, the first step was the washing of glass with Alconox, DI water and IPA. Next, the glass was primed with HDMS, coated with photoresist (Figure 24, step 1) on the SVG track and patterned on the DWL (Figure 24, step 2). The electrode, track and pad design, identical to the ones used by (Martins, et al., 2011), are depicted in Figure 23. After the photoresist development, the areas corresponding to the electrodes, tracks and pads for electrical connection were unprotected by the photoresist (Figure 25, left), so that the TiW could be directly deposited on the glass (Figure 24, step 3). After the lithography step, a 3000 Å layer of TiW was deposited on the glass (Figure 24, step 4), by magnetron sputtering (as previously described for the aluminium deposition), in the Nordiko N7000. The sample, after TiW deposition, is depicted in Figure 25. Next, the sample was subject to a liftoff process by submersing it in Microstrip 3001, for several hours, at 65°C, with sonication, using a Fisher Scientific FB15047 hot bath/sonicator. During the liftoff process, the photoresist that was protecting certain areas of the sample was dissolved, removing (lifting) the metal layer on those areas.

Only the areas where the metal was directly deposited on the glass remained, defining the electrodes and pads (Figure 24, step 5).

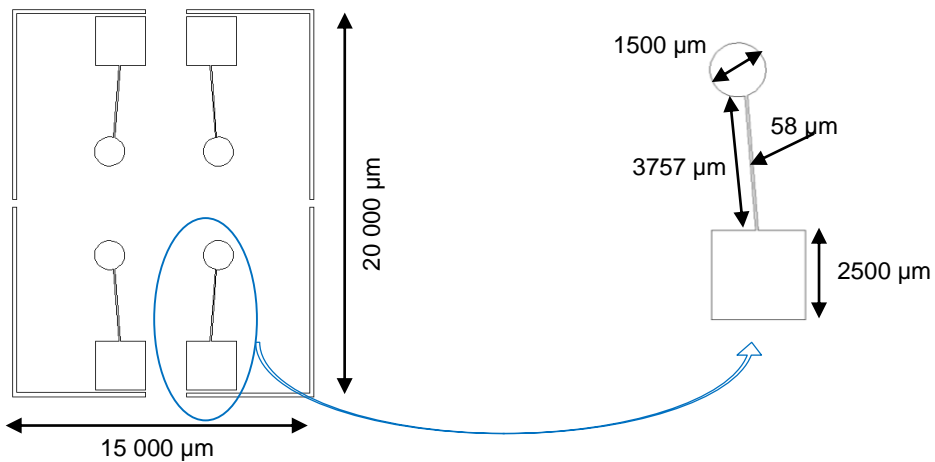


Figure 23 – AUTOCAD design of the electrodes and pads for two microchannels (left), and detail of the design (right), including dimensions (top view). Design as by (Martins, et al., 2011).

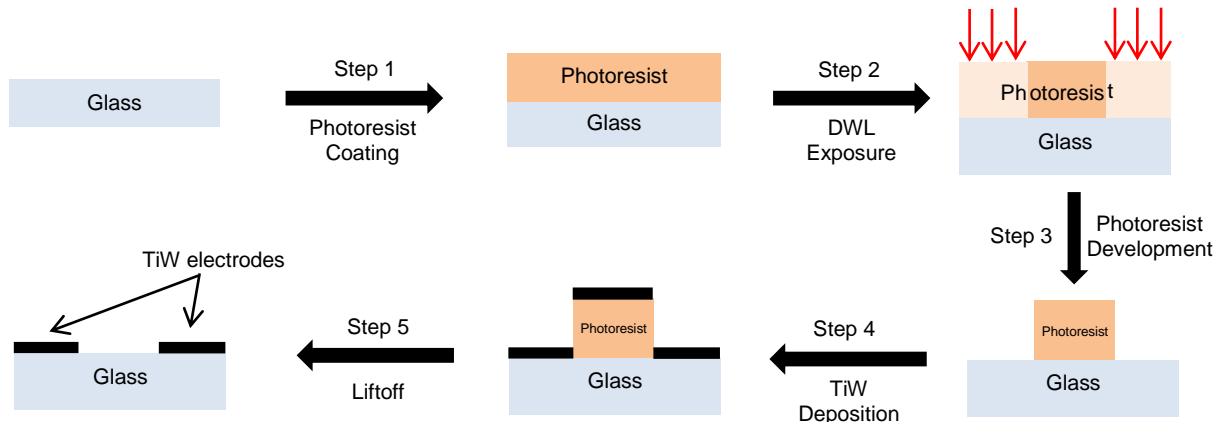


Figure 24 – Flowchart of the electrode deposition and patterning on glass (side view). Dimensions of materials not to scale.

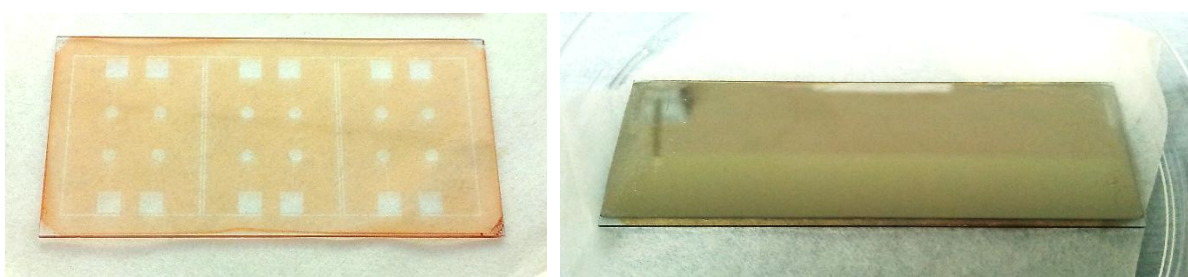


Figure 25 – Images of the TiW electrode microfabrication. Glass sample after lithography, with the transparent areas not covered by photoresist (left) and glass sample after TiW deposition, ready for the liftoff step (right).

3.4.5. Device Sealing and Ancillary Equipment Connection

After having the channels defined on PDMS and the TiW electrodes deposited on glass, the only missing step in order to have sealed channels is the bonding (Figure 26).

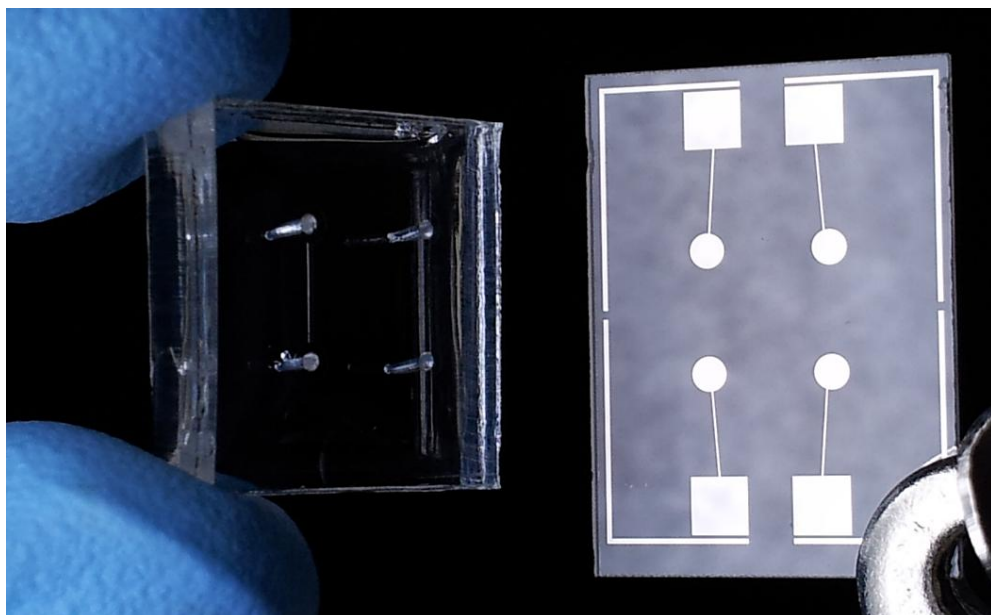


Figure 26 – PDMS chip (on the left), ready to be sealed against the glass with the TiW electrodes (on the right).

The bonding was achieved by first exposing the PDMS and glass surfaces to a UV/Ozone treatment, for 6 min, on a UVO Cleaner (Model 144AX-220 by Jelight Company). This method is derived from a UV/Ozone exposure technique originally developed for the removal of organic contaminants from semiconductors as an alternative to oxygen plasma ashing. (Tsao & DeVoe, 2009) Using a low-pressure mercury lamp to expose a substrate in an air-filled chamber at atmospheric pressure, light output at a wavelength of 184.9 nm is absorbed by oxygen in the air, resulting in the generation of ozone. Light at 253.7 nm is absorbed by the ozone, leading to breakup of the ozone and production of atomic oxygen. Hydrocarbons at the substrate surface are rapidly oxidized due to the presence of elemental oxygen, together with the fact that most hydrocarbons also absorb the 253.7 nm radiation from the UV source. The UV/ozone exposure can also break polymer chains and insert oxygen-containing functional groups (OH groups), substantially increasing surface energy. The increased surface energy will allow a strong bonding of the mating surfaces. (Tsao & DeVoe, 2009)

After the UVO treatment, the microchannels and the electrodes were manually aligned on a low power AMSCOPE microscope. The chip was pressed by hand with uniform pressure and was heated at 70 °C for 30 min in a Memmert oven to complete the bonding. The complete device is depicted in Figure 27. Having the devices sealed, there was the issue of interconnecting the microfluidic chip with the pumping system (New Era NE-300 syringe pump) and with the picoammeter (Keithley 237 source-measure unit) in order to perform the experiments. The fluidic connection was performed by inserting stainless steel adaptors in the inlet and outlet of the microchannel and by connecting those adaptors to

1ml luer-lock syringes using polytetrafluoroethylene tubing. A homemade PMMA chip holder with spring-loaded contacts was prepared in order to make electrical connections to the TiW pads on the chip (Figure 28). This chip holder was inserted on a metallic box (electrical shielding for low noise measurements) with BNC connectors, connected to a triaxial cable to drive the current from the electrodes to the picoammeter (Figure 29).

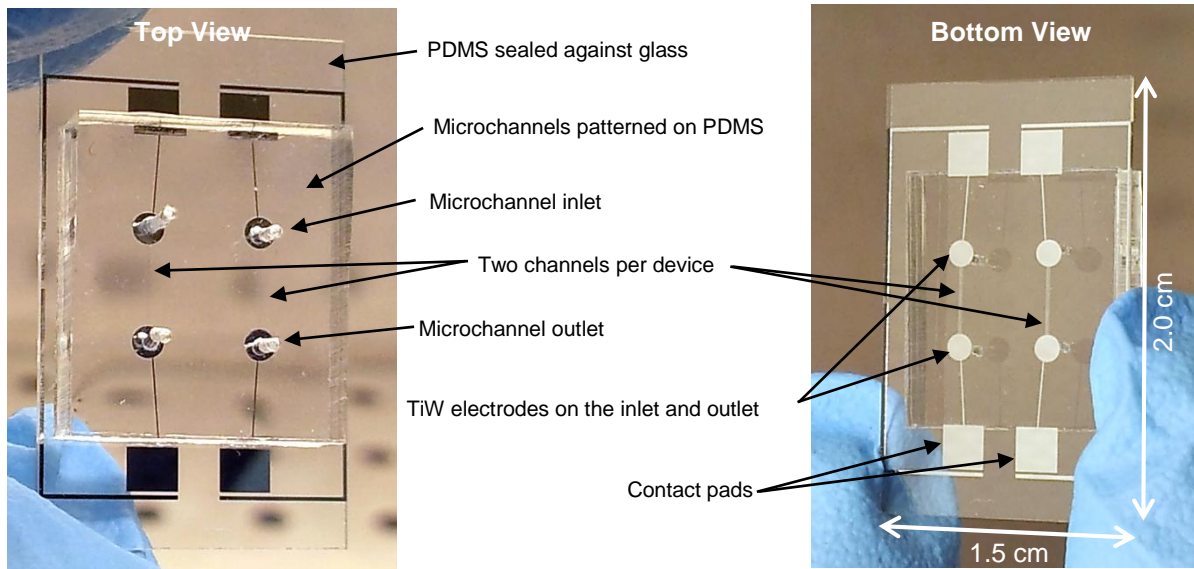


Figure 27 – Photographs of the sealed microfluidic devices. Top view (left) and the bottom view (right) of the chips employed in the streaming current and fluorescence experiments.

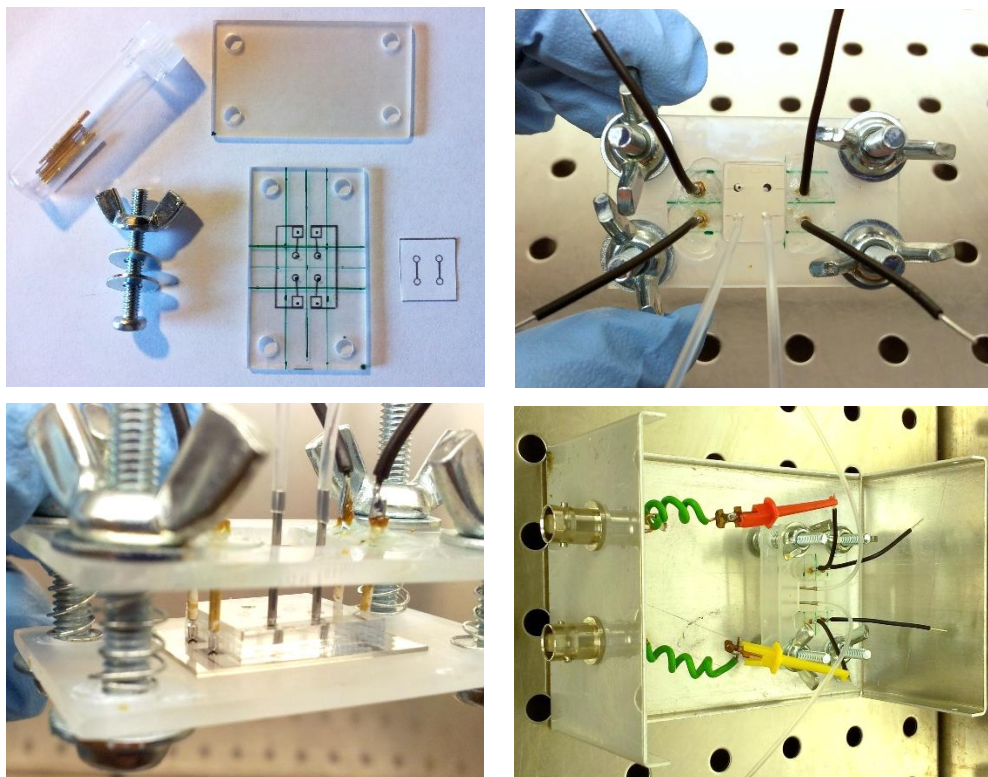


Figure 28 – Some of the parts used to manufacture the chip holder (top left), top view of the chip holder with mounted microfluidic chip, two tubes and adapters (top right), side view of the chip holder and chip (bottom left) and chip holder mounted inside a metallic box enclosure (bottom right).



Figure 29 – Picoammeter, syringe pump and metallic box (left) and detail of the syringe pump and metallic box (right).

3.5. Streaming Current and Potential Measurements

As mentioned before, the streaming current was measured using a Keithley 237 picoammeter, connected with a triaxial cable to the metallic enclosure where the microfluidic chip was installed. The picoammeter has a 10 fA resolution and typical noise levels, with the triaxial cable connected to the microfluidic channel, were of the order of pA. Some streaming potential measurements were also performed using the same equipment, but given the similarity of the procedures, and given that most of the measurements were of the streaming current type, only these measurements are described.

In the Keithley 237, positive current values are obtained when positive current is flowing out of the output HI terminal (+). The output HI terminal (+) was connected to the inlet electrode while the output LO terminal (-) was connected to the outlet electrode. In the case of an unfunctionalized channel, with DI water in the channel, the surface charge is negative and the counterions positive in nature. When the flow is started, positive counterions are pushed towards the outlet. These positive counterions are neutralized by electrons coming out of the outlet electrode, which is connected to the output LO terminal (-). Negative charge flowing out of the output LO terminal (-) is equivalent to positive current flowing in, which, in turn, is equivalent to positive current flowing out of the output HI terminal (+), which means a positive current value is observed on the picoammeter. Resuming: when positive current values are measured, the counterions are positive and the surface charge is negative (Figure 30).

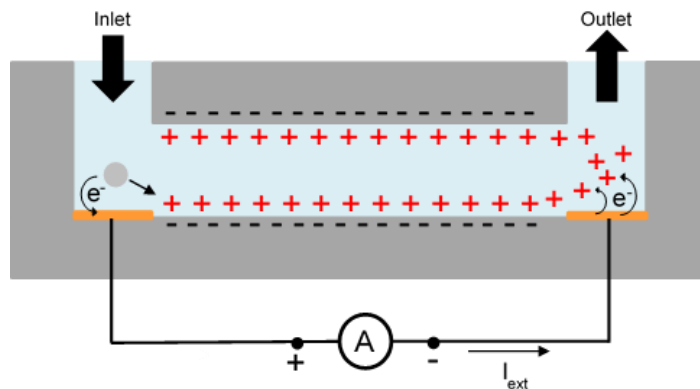


Figure 30 – Positive current convention. A neutral species gives an electron to the inlet electrode. The electron is driven through the picoammeter and delivered to a positive counterion at the outlet electrode, resulting in a positive current reading in the Keithley 237. If the measured current is positive, the counterions in the EDL are positive and the surface charge is negative.

The streaming current, measured with integrated polarizable electrodes, may have a transient behavior, and hence, the current was measured and recorded along time for posterior analysis. The acquisition rate of the picoammeter depends on the integration time, the filtering applied to the signal and the current scale. The integration time was the line cycle (corresponding to the 50 Hz of the grid), in order to remove 50 Hz noise. The filtering was disabled (no average of the signal performed) in order to have a better temporal resolution (more readings per time unit), and the instrument scale was, most of the time, the nA scale. In these conditions, two to three data points were acquired each second. In order to record the measurements directly to the computer and control the picoammeter, a C-language program was developed, which allowed to communicate with the device using the GPIB interface as long as the National Instruments NI488.2 drivers were installed on the computer. The measurements were performed at ambient temperature (between 22 °C and 24 °C), controlled by the air conditioning.

The determination of the real streaming current value from the measured external current was studied by (Martins, et al., 2013). If the flowing solutions have low ionic concentrations (up to 10^{-4} M), the measured current does not have a transient behavior and it corresponds to the real streaming current inside the channel (Figure 31). For higher counterion concentrations, the channel resistance decreases, and that, together with the polarizability of the electrodes, results in a transient behavior of the measured current (Figure 32). In the case of transient behavior, the current peak, right after initiating the flow, corresponds to the real streaming current value.

For each streaming current measurement, a baseline (with stationary liquid in the channel) was acquired for a few min, and, while recording, the syringe pump was actuated, initiating the flow inside the channel. The current is recorded for a few minutes and then the flow is stopped. Prior to start pumping again, there is the need to wait for all the currents to neutralize inside the channel (typical pumping and waiting times are in Table 4). All the streaming current values were measured three times and then averaged. The flow rate used was 10 μ l/min, unless otherwise stated.

For the lower counterion concentrations (non-transient external current) the streaming current values were calculated by averaging the current during the flow period and subtracting the baseline (Figure 33). For the higher concentrations, the value of the external current peak was determined and then the baseline was subtracted to it (Figure 33), yielding the real streaming current value.

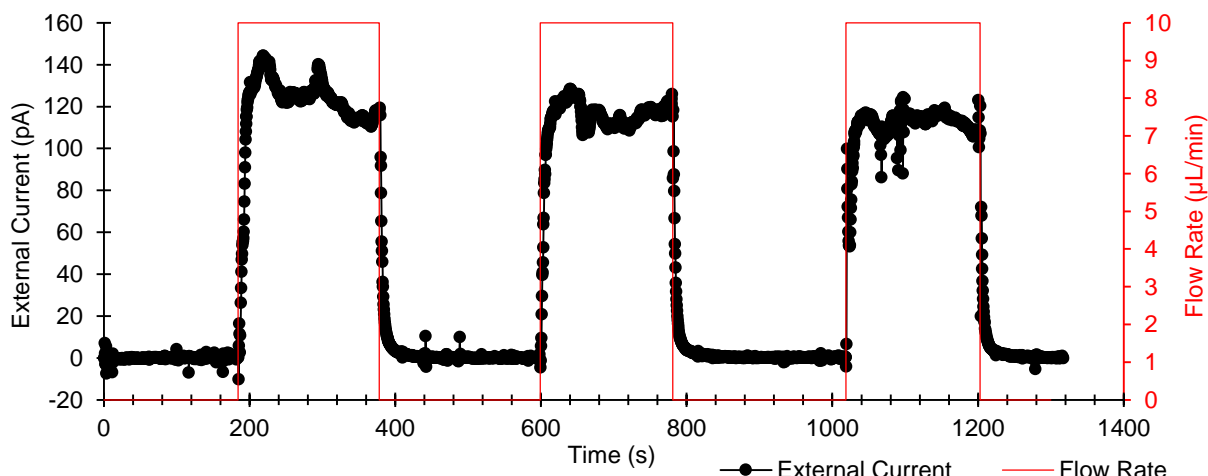


Figure 31 – Example of a streaming current measurement with DI water in the channel. No transient behaviour of the external current is observed due to the low ionic strength of the solution.

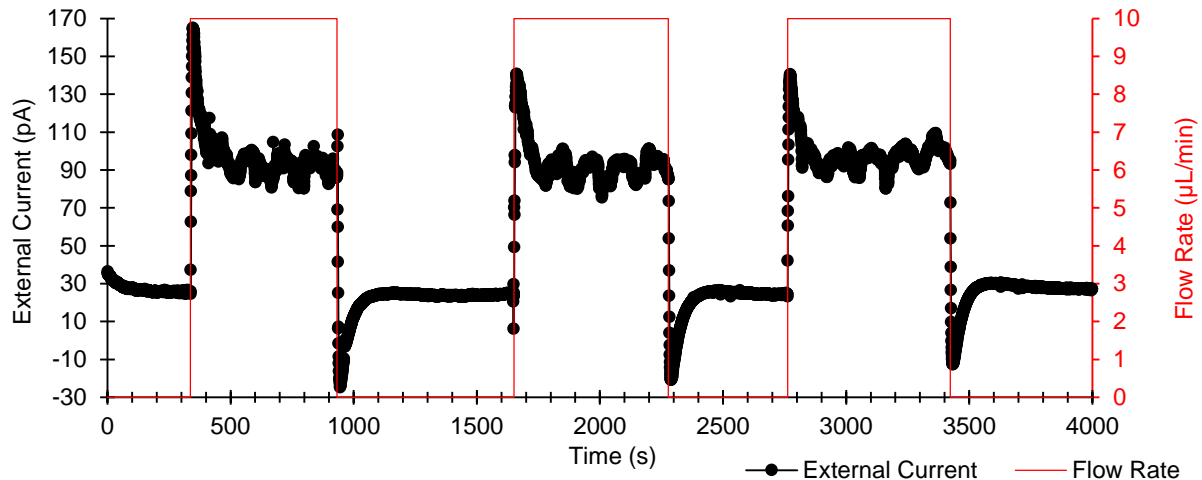


Figure 32 – Example of a streaming current measurement with a 1 mM KCl solution in the channel. The external current is transient because of the higher ionic strength of the solution, which decreases the channel resistance.

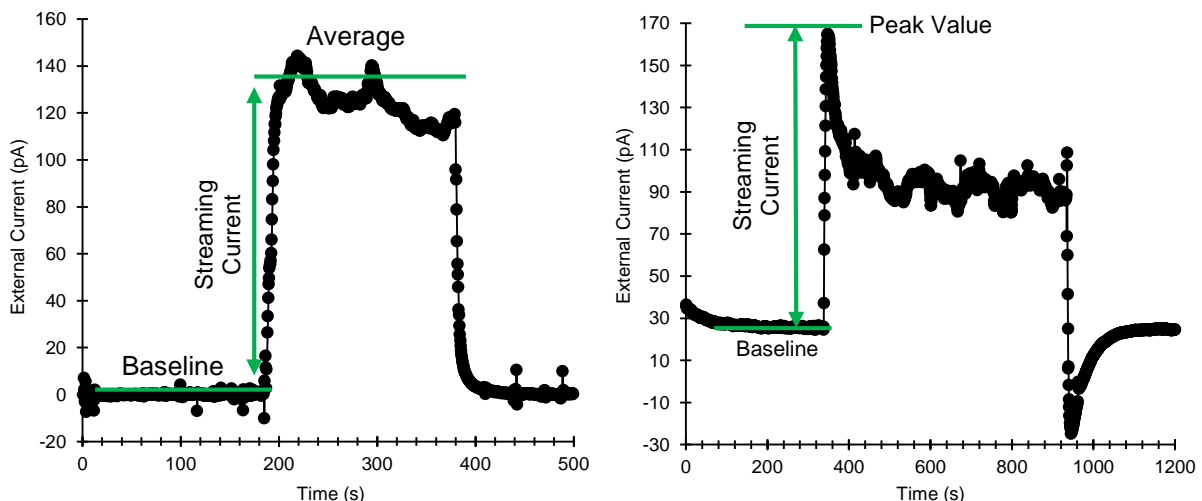


Figure 33 – Illustration of the method used to calculate the streaming current values from the measured external currents, in the case of a non-transient external current (left) and for a transient external current (right).

Table 4 – Typical experimental pumping and waiting periods for the streaming current measurements.

Counterion Concentration	Pumping Period (min)	Waiting Period (min)	Total Reading Time for 3 Measurements (min)
10^{-6} M (DI Water)	3	3	20
10^{-4} M	3	10	45
10^{-3} M	3	10	45
10^{-2} M	2	7	30
10^{-1} M	1	3	15

3.6. Fluorescence Measurements

The streaming current was measured after each protocol step. Afterwards, the inlet and outlet adapters were disconnected, the microfluidic chip was removed from the chip holder and took to the fluorescence microscope for imaging. A Leica DMLM microscope, equipped with a 20X objective (20X/0.4, N PLAN, Leica Germany, 566026), was used for the fluorescence imaging. The images were acquired with a Leica DFC300FX camera, using the maximum resolution option, in colour, and saved in 8 bit uncompressed tiff format. The exposure used was 2.0 s, gain=1 and gamma=1, unless otherwise stated. The filter cubes used and its characteristics are listed on Table 5. Three fluorescence images were acquired for each measurement: one in the beginning, other in middle and other at the end of the microchannel. The measurements were performed at ambient temperature, kept controlled by the air conditioning system, between 22 °C and 24 °C.

Table 5 – Fluorescence microscope filters used, respective characteristics and fluorophore response.

Filter Designation	Illumination Path	Observation Path	Used to Image	Fluorophore Excitation Peak	Fluorophore Emission Peak
I3	Band-Pass: 450-490 nm	Long Pass: 515 nm	Probe Molecules (6-FAM labelled)	495 nm	520 nm
TX2	Band-Pass: 540-560 nm	Band Pass: 645-675 nm	Target Molecules (DY560 labelled)	553 nm	578 nm

After the experiments, the images were opened on ImageJ (version 1.47) for processing. A region of interest was selected inside the microchannel and the mean intensity value (mean RGB value across the selected region) was taken. Then, a region outside the channel was selected and the background mean intensity value was measured. A numerical fluorescence value was obtained by subtracting the background mean intensity to the mean intensity on the channel region. This procedure was repeated for the three images along the channel and the final fluorescence value is the average of the three individual images. In Figure 34 there is an example of a fluorescence image and the regions of interest.

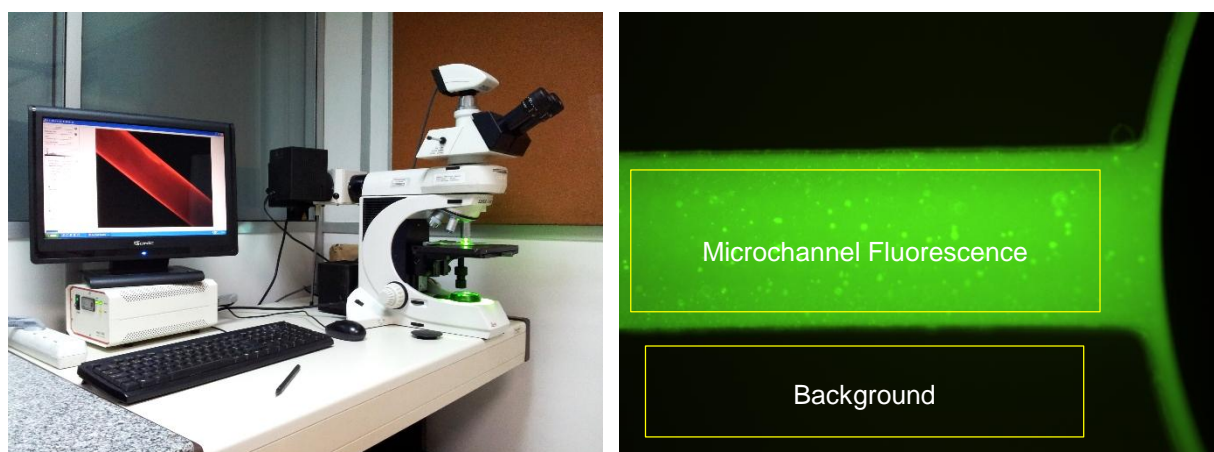


Figure 34 – Leica DMLM microscope setup, used for the fluorescence imaging (left) and fluorescence image acquired using the I3 filter, with highlighted regions of interest (right).

3.7. DNA Surface Density Calibration Using the Nanoplotter

At a certain point of the work, in order to better describe the probe immobilization, the density of DNA molecules at the surface of the microchannels was calculated using the fluorescence intensity. The base idea is that the mean fluorescence intensity of a given region depends on the density of fluorescently labelled DNA molecules at the surface. If it is possible to make a correspondence between the number of molecules per surface unit (surface density) and the mean fluorescence intensity, then it is possible to create a calibration curve and use it to calculate the molecule density from the measured fluorescence.

To perform this calibration, micro spots of oligonucleotide solutions were dispensed on the surface of PDMS. If the DNA concentration and volume of such spots is well known, then it is possible to calculate the number of molecules in each spot. After imaging, the area of the spot was calculated and it was possible to make a correspondence between the molecule density (number of molecules/surface unit) and the mean fluorescence intensity of the spot.

The SIM Nanoplotter 2.1, equipped with a NanoTip (piezoelectric tip), is able dispense volumes as low as 56 pL in predetermined positions of the PDMS microchannel (Figure 35). Given the dimensions of the microchannel, a volume of 1.12 nL, corresponding to 20x56 pL droplets, proved to be an adequate volume. The PDMS chips (not sealed) were treated with UVO and silanized (2% APTES in acetone, for 2 h). This treatment is identical to the one that the sealed microchannels were subject to. The Nanoplotter system contains a humidifying system that was regulated to 70% relative humidity for slow spot drying. The nanoplotter was covered with a black plastic cover to avoid photobleaching of the molecules, given that the spotting procedure took several hours to complete. The oligonucleotide solutions were prepared in 10 mM PB, and contained 5% glycerol so that the drops dried slowly. The following oligonucleotide concentration solutions were spotted (for both the probe and the target oligos): 0 M, 1.0X10⁻¹⁰ M, 5.0X10⁻¹⁰ M, 1.0X10⁻⁹ M, 5.0X10⁻⁹ M, 1.0X10⁻⁸ M, 5.0X10⁻⁸ M, 1.0X10⁻⁷ M, 5.0X10⁻⁷ M, 1.0X10⁻⁶ M, 5.0X10⁻⁶ M, 1.0X10⁻⁵ M and 5.0X10⁻⁵ M. Each concentration was spotted three times.

After spotting, the PDMS devices were imaged in the Leica microscope (the setup was previously described). Given the high range of concentrations spotted, the camera gain and exposure used were not constant, to avoid under and over exposure. Considering exposure linearity (experimentally verified), the fluorescence values obtained were later adjusted to the scale of the conditions used in the microchannel imaging (exposure=2.0 s, gain=1). Using ImageJ, the background was subtracted to the fluorescence of the spot and the area of the spots was calculated from the area in pixels, having the channel width (200 µm) as a reference. Examples of the spots on a microchannel are depicted in Figures 36 and 37.

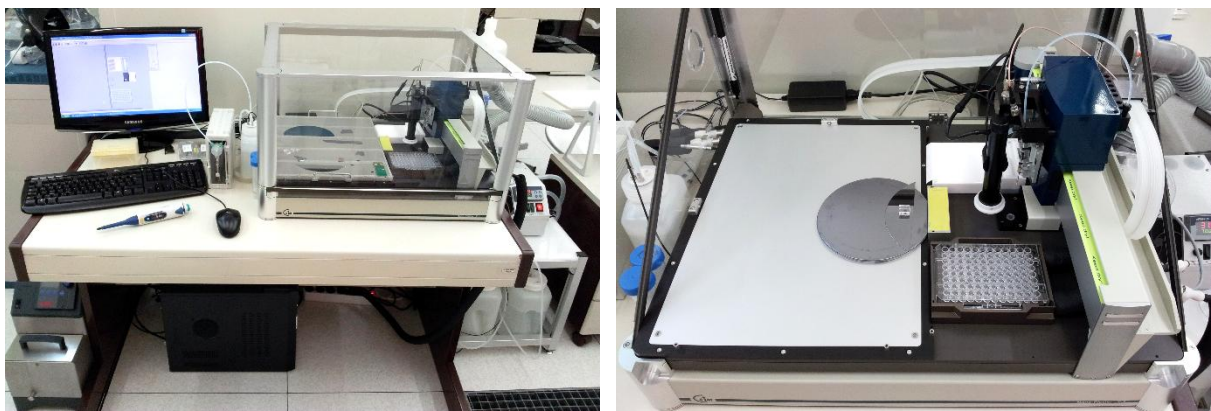


Figure 35 – SIM Nanoplotter 2.1 system overview (left) and detail of the open nanoplotter; note the PDMS chip on the center of the image, ready for spotting; the oligonucleotide solutions are deposited on the well plate (right).

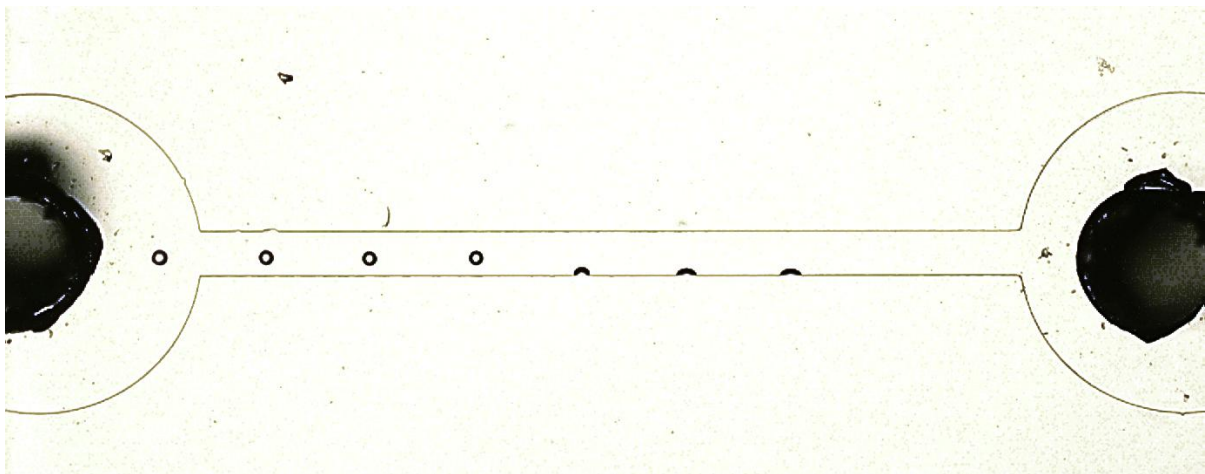


Figure 36 – PDMS microchannel after spotting 1.12 nL drops. The first four spots on the left dried on the center of the channel, but the last three dried towards the wall on the channel. The length of the microchannel is 4 mm and the width 200 µm. Imaging in visible light, using the Leica DMLM microscope with a 2.5x objective.

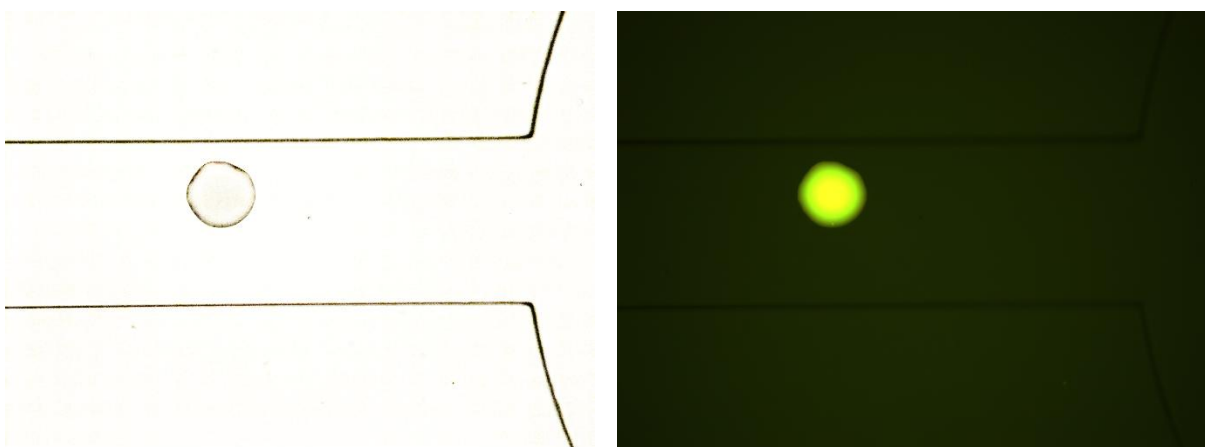


Figure 37 – Example of a 1.12 nL spot of DNA probe solution. Imaging in visible light (left) and using the I3 fluorescence filter (right), on the Leica DMLM microscope, with the 20x lens. The width of the microchannel is 200 µm.

4. Results and Discussion

This section summarizes the main results, explaining the sequence of the experiments and discussing the results obtained.

First, electrokinetic measurements were performed on an unfunctionalized channel in order to characterize the surface of the microchannel in terms of the ζ -potential. The accuracy of the streaming current and potential measurements was assessed.

Afterwards, the surface was functionalized and experiments for the detection of 5 μM target DNA were performed with success. Electrokinetic and fluorescence measurements were performed in parallel and used to discuss the protocol.

Working towards the detection of lower target concentrations, the surface blocking step was optimized by testing different blocking agents. Also, two target incubation conditions were compared, namely flow incubation and steady-state incubation. Lastly, the density of probe and target molecules on the surface was determined using fluorescence.

4.1. Measurements with DI Water, KCl and Buffer Solutions

After fabricating the first microfluidic devices, the former step was to measure the streaming current while running DI water, KCl solutions and buffer solutions (PB and PBS), in order to verify that the streaming current values made sense and were accurate. By varying the flow rate, it was possible to verify the linear relationship between the streaming current and the flow rate (Figure 38), which was expected (see Expression 6).

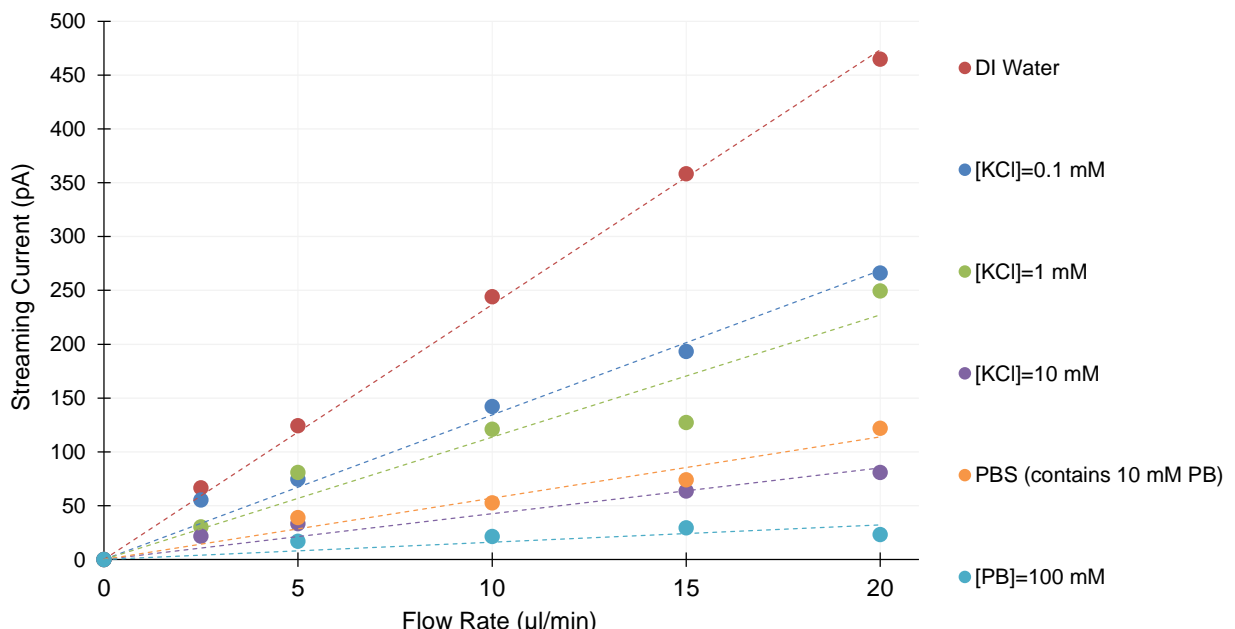


Figure 38 – Linear dependency of the streaming current on the flow rate, for DI water, KCl solutions, PB and PBS.

As discussed in section 3.5, given that the streaming current values are positive, the counterions are positive and the glass/PDMS surface charge is negative. This was expected given that the running solutions had pH ranging from 5.7 (DI water in equilibrium with the atmosphere) to 7.4 (PB and PBS buffers) and the isoelectric point (pl) of glass is pl = 2.1. (Lameiras, et al., 2008)

The streaming current values are higher for more dilute solutions, and hence the slopes of the current vs flow plots are higher for the lower counterion concentrations. According to expression (6), the slope of the current vs flow rate plot depends directly on the ζ -potential. This means that different ζ -potentials can be calculated from the slopes of the graphical representations above. Also obvious at this point is the fact that the ζ -potential depends on the counterion concentration.

The effect of counterion concentration on the ζ -potential arises from at least two effects. (Kirby & Hasselbrink, 2004) Firstly, the counterions may be adsorbed to the surface, or into the Stern layer, and thereby change the net surface charge density that must be shielded by the diffuse region. If the counterions are more adsorbed to the surface, the diffuse region will have a lower net charge, and, therefore, the ζ -potential and the streaming current will be lower in magnitude. Secondly, changing the counterion concentration changes the thickness of the EDL, which modifies the ζ -potential directly, even for a fixed surface charge density. If the surface charge density is unaffected by counterion strength, and all the shielding is performed by the diffuse portion of the double layer, then the dependence of ζ on counterion concentration (given constant temperature and dielectric constant) can be shown to be (Kirby & Hasselbrink, 2004):

$$\zeta \sim \lambda_D \sim a_0 + a_1 \log c \quad (8)$$

where λ_D is the Debye length (characteristic thickness of the EDL), a_0 and a_1 are constants and c is the counterion concentration, for a symmetric electrolyte with counterions of valency equal to 1. In the case of KCl or KH₂PO₄ (contained in PB and PBS), the counterion is K⁺ and expression (8) should apply. The previous expression applies for relatively low counterion concentrations and high ζ -potentials (generally applicable for silica below 100 mM at pH=6 and below 10 mM at pH=3.5). (Kirby & Hasselbrink, 2004)

The results for KCl at 10 mM are very similar to the ones for PBS. PBS consists of 10 mM phosphate buffer (KH₂PO₄), 2.7 mM KCl and 137 mM NaCl. Despite the 137 mM of NaCl in the PBS (near physiological values), which contribute with Na⁺ counterions, it seems that the K⁺ counterions are more relevant to the streaming current measurements. This may be due to the different solubilities (ion hydration) of Na⁺ and K⁺ counterions. Na⁺ has a higher solubility than K⁺ in water (Baldwin, 1996), meaning that it is more hydrated by the water molecules. Na⁺ will be less attracted to the glass surface because its charge is more shielded by the water molecules than K⁺. It now makes sense that K⁺ counterions, more attracted to the interface, have more influence in the streaming current measurements than Na⁺ counterions. The same rational would apply for any other ionic species with different solubilities.

Other factors that modify the ζ -potential are the pH and the temperature. For nonspecifically adsorbing counterions, the variation of the ζ -potential with pH is attributable to protonation or

deprotonation of silanol sites (see expression (1)) and is, to first order, independent of the concentration. The dependence of ζ on temperature comes from changes in the silanol equilibrium, adsorption equilibria, and diffuse double-layer thickness. The ζ -potential of silica increases approximately 1.75% per $^{\circ}\text{C}$. (Kirby & Hasselbrink, 2004) Therefore, even minor temperature variations (e.g., 5–10 $^{\circ}\text{C}$) are quite significant when ζ is calculated. Comparisons of ζ -potentials cannot be made unless temperatures are well-specified. All the measurements in this work were performed at temperatures between 22 $^{\circ}\text{C}$ and 24 $^{\circ}\text{C}$.

At this stage, measurements of the streaming potential were attempted, in order to verify if there was any advantage in using the streaming potential instead of the streaming current. The Keithley 237 was set to work as a voltmeter instead of an ammeter and the acquisition was performed as for the streaming current. According to expression (7), the streaming potential should also have a linear dependency on the flow rate. This dependency was verified for the various solutions (different counterion concentrations), as represented in Figures 39 and 40.

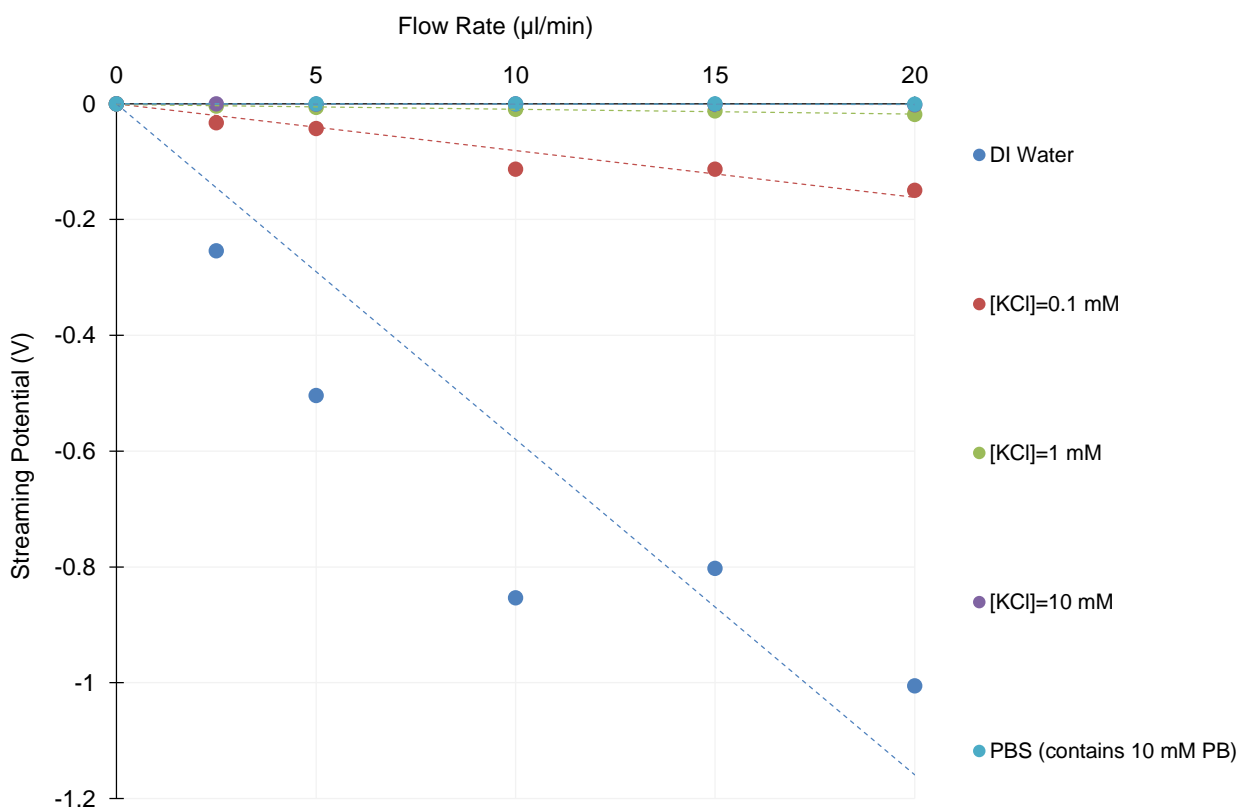


Figure 39 – Linear dependency of the streaming potential on the flow rate, for DI water, KCl solutions and PBS. On this streaming potential scale, the measurements for the higher counterion concentrations cannot be clearly distinguished (see the next figure).

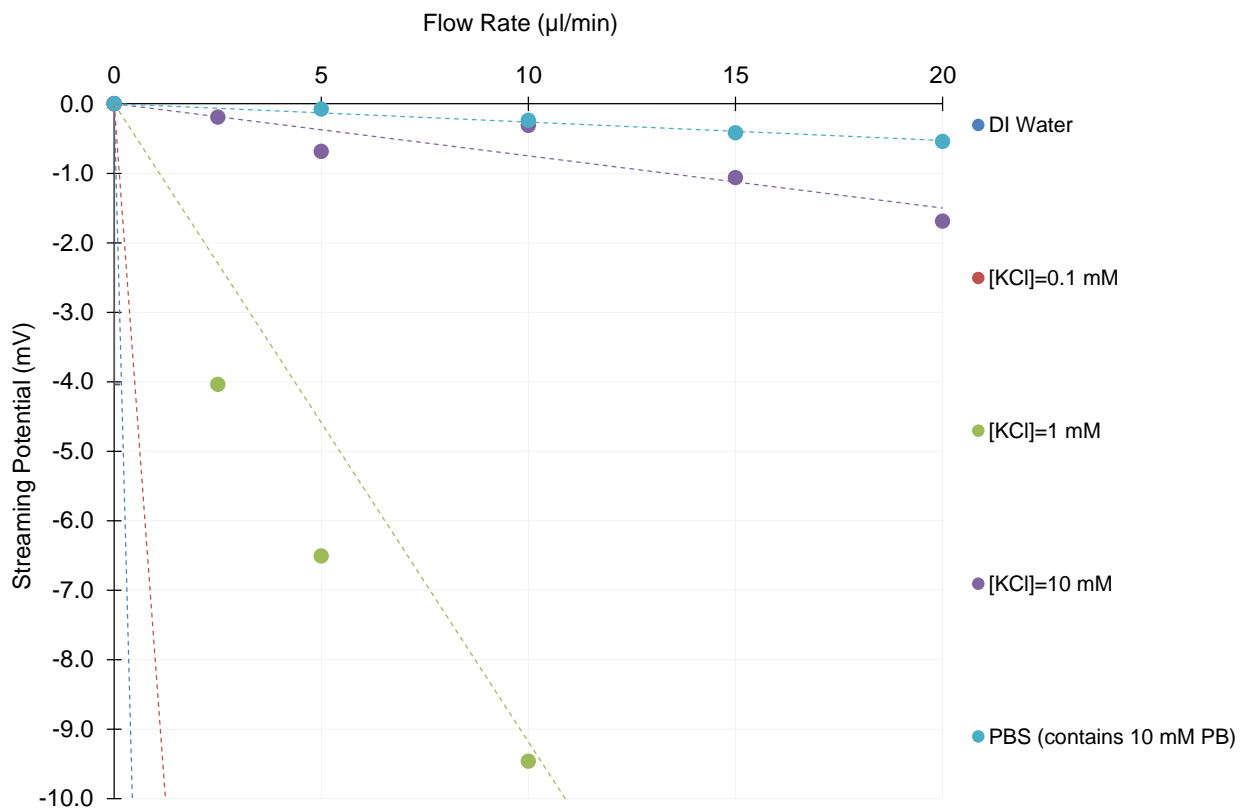


Figure 40 – Linear dependency of the streaming potential on the flow rate, for DI water, KCl solutions and PBS.

The streaming potentials obtained are negative because the positive terminal (output HI) of the voltmeter was connected to the inlet electrode (same connections as used for the current) and the negative terminal to the outlet. When the positive counterions are pumped towards the outlet, the potential in the outlet (negative terminal) is higher than on the inlet, yielding a negative potential reading (the negative terminal is connected to the positive charges). This confirms that the counterions are positively charged and the surface is negatively charged.

As previously noted for the streaming current, the streaming potential depends on the ζ -potential (expression (7)), which, in turn, is a function of the counterion concentration. All the comments made above, for the streaming current, can be extrapolated to the streaming potential, including the similarities between the readings made with KCl at 10 mM and PBS, which reflect different solubilities of the K^+ and Na^+ counterions.

The streaming potential behavior in time is identical to the streaming current behavior (Figure 33), and may be constant or transient in time, depending on the flowing solution. However, the Keithey 237 instrument used to perform the measurements has a better current sensitivity, and, therefore, there was apparently no advantage in using the streaming potential instead of the streaming current.

Given that both streaming current and streaming potential measurements were available, the ζ -potentials were calculated from both sets of data, for comparison. However, in order to use equation (7) for the ζ calculations from the streaming potential data, the apparent conductivities of the channels needed to be measured. This was made in an approximate manner, without flow in the channel, for the various solutions. The flow may modify the channel conductivity, but this was ignored. An I-V curve was

acquired with the channels filled with each one of the solutions, the electrical resistance of the channel was obtained from the slope of such I-V curves and the conductivities (S/m) were calculated using:

$$\sigma = \frac{1}{\rho} = \frac{R l}{A} \quad (9)$$

where ρ ($\Omega \cdot m$) is the electrical resistivity, R (Ω) is the electrical resistance, A (m^2) is the cross-sectional area of the microchannel ($4 \times 10^{-9} m^2$) and l is the length of the microchannel ($4 \times 10^{-3} m$).

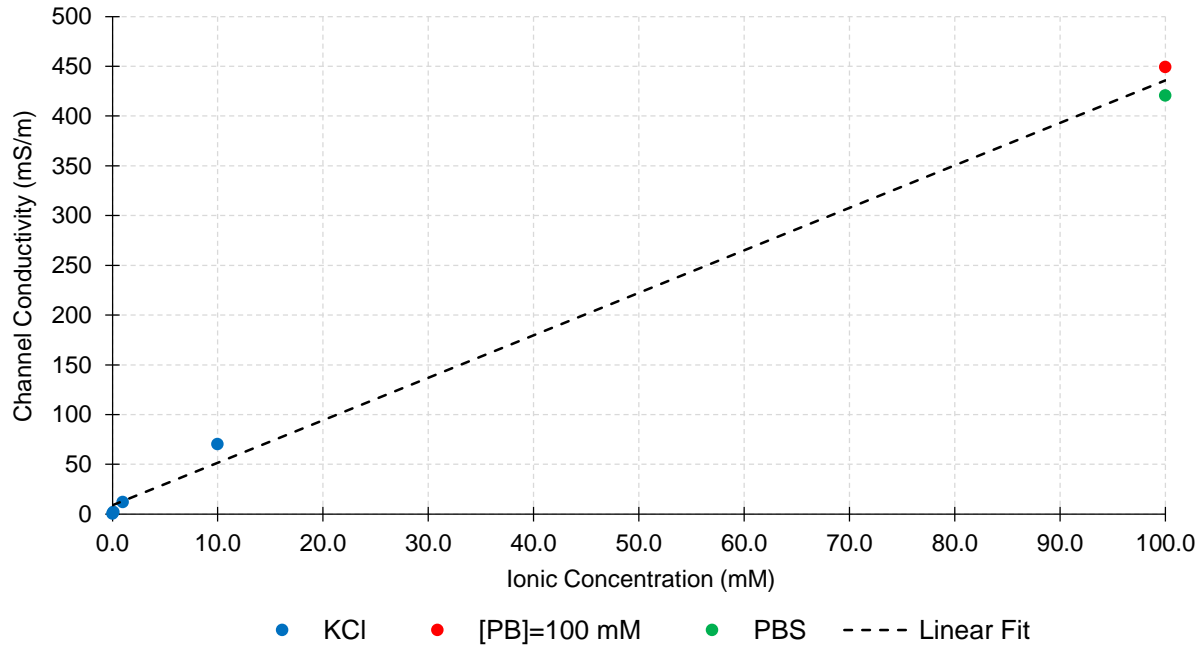


Figure 41 – Apparent conductivity of KCl, PB and PBS solutions in the microchannel, as a function of the ionic concentration.

The conductivity is proportional to the current that flows between the electrodes. For current to flow, ions must be present in solution to carry the charge from one electrode to another. Increasing the number of ions in solution will increase the amount of charge that can be carried between electrodes and will increase the conductivity. This is why solutions with higher ionic strength decrease the channel resistance and increase the conduction current that tends to neutralize the streaming current, making the readings transient in time and more difficult to perform. The electric conductivity through the bulk of the solution can be considered as the sum of the contributions due to the various ionic species in solution:

$$\sigma = \sum_i |z_i| u_i C_i \quad (10)$$

where z_i is the charge (valency) of each ionic species, C_i is the concentration of the species and u_i is the limiting velocity of the ion in an electric field (index of migration velocity). (Bard & Faulkner, 2001)

The channel conductivity is apparently linear on the ionic concentration of the solution (Figure 41). Looking at expression (10), if we consider that the $z=1$ and the index of migration velocity index (u) is identical for all the ionic species in solution, then the conductivity will depend only on the total concentration of ionic species in solution. Looking at Figure 41, perhaps the most interesting part of the result is the fact that a PB solution at 100 mM has an identical conductivity to PBS (137 mM NaCl, 10 mM PB), given that the total ionic concentration for PB and PBS is identical. This corroborates the theory that the conductivity depends linearly on the ionic strength of the electrolyte, and can be approximated by (10).

After obtaining the conductivities, the ζ -potentials could finally be calculated from both sets of data (streaming current and streaming potential). From expression (6), the slope of the streaming current vs flow rate plot can be approximated by:

$$\frac{dI_S}{dQ} = \frac{12 \varepsilon_0 \varepsilon_r}{h^2} \zeta \quad (11)$$

Therefore, for each counterion concentration, ζ can be calculated from the streaming current data using:

$$\zeta = \frac{dI_S}{dQ} \frac{h^2}{12 \varepsilon_0 \varepsilon_r} \quad (12)$$

The electric permittivity of vacuum was considered to be $\varepsilon_0 = 8.854187817 \times 10^{-12}$ F m⁻¹ (Mohr, et al., 2012) and the relative permittivity of the solutions were considered constant and equal to the relative electrical permittivity of water at 24 °C, $\varepsilon_r = 78.5$ (Fernández, et al., 1995). The square of the height of the channel, $h^2 = 4.0 \times 10^{-12}$ m².

From expression (7), the slope of the streaming potential vs flow rate plot can be approximated by:

$$\frac{d\Delta\phi}{dQ} = \frac{12 \varepsilon_0 \varepsilon_r l}{\sigma h^3 w} \zeta \quad (13)$$

where σ are the conductivities previously calculated for each of the running solutions (Figure 41). For each counterion concentration, ζ can be calculated from the streaming potential data using:

$$\zeta = \frac{d\Delta\phi}{dQ} \frac{\sigma h^3 w}{12 \varepsilon_0 \varepsilon_r l} \quad (14)$$

The results of the ζ -potential calculations, using expressions (12) and (14) are represented as a function of the ionic concentration in Figure 42.

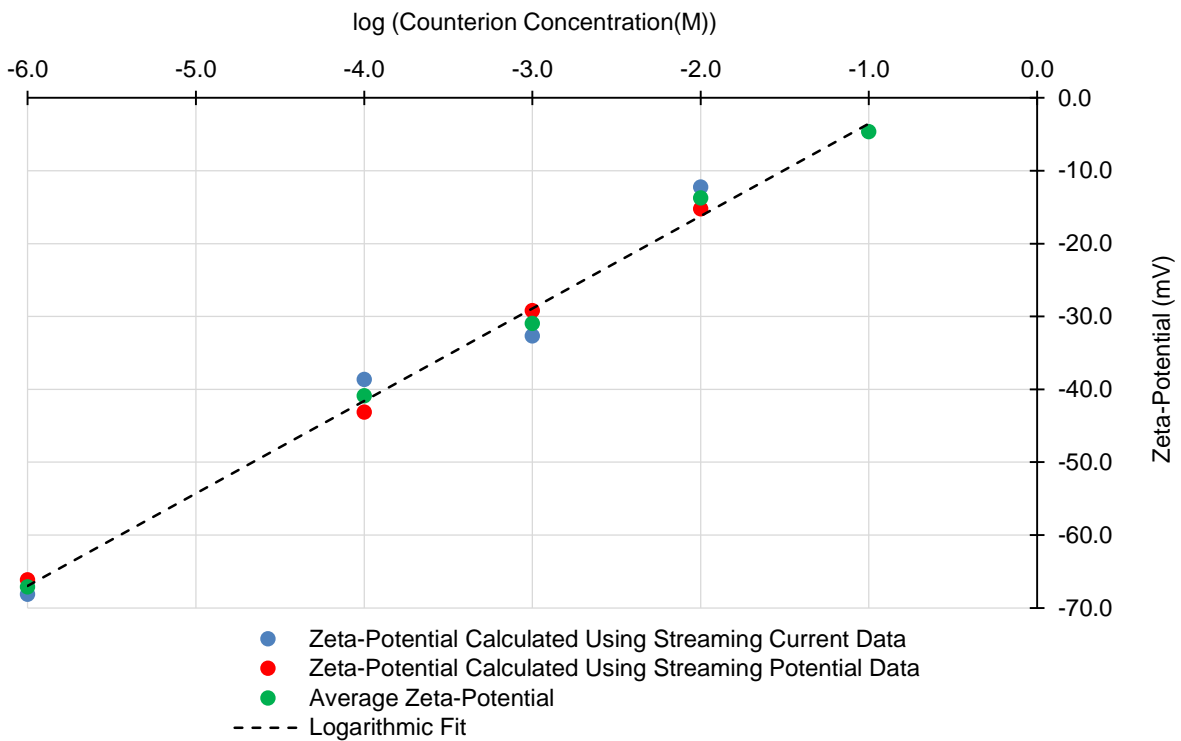


Figure 42 – Zeta potential as a function of the total ionic concentration of the solutions flowing in the microchannel. A logarithmic dependency is observed. The results are identical when calculating the zeta potential with the streaming current data and the streaming potential data.

As can be observed, there is a logarithmic dependency of the ζ -potential on the ionic strength of the solution. This behavior was expected and was discussed above (see expression (8)). Such a logarithmic regression yielded the following experimental dependency of the ζ -potential on the total ionic concentration of the solution (C) :

$$\zeta = 12.69 \log(C) + 9.1389 \quad (15)$$

where ζ has units of mV and C has units of molar (mol/L).

The results are identical when calculating the ζ -potential using the streaming current data and the streaming potential data, meaning that the measurements are robust. This also means that the approximations made in the calculations were reasonable (the conductivity measurements were performed with no flow, the electrical permittivity of the solutions was considered to be constant, the thickness of the EDL was considered to be much smaller than the other channel dimensions, among other approximations).

Finally, the ζ -potential values were compared to some values in the literature (Table 6). The experimental values are comparable to the ones in the literature (for silica).

Table 6 – Experimental and reference zeta-potential values as a function of the ionic strength of the solutions and depending on the material (silica or PDMS). Reference 1: (Erickson, et al., 2000). Reference 2: (Kirby & Hasselbrink, 2004).

Solution	Total Ionic Concentration (mM)	Conductivity (mS/m)	Experimental Zeta-Potential Calculated using:		Average Experimental Zeta-Potential (mV)	Reference Zeta-Potential		
			Streaming current data (mV)	Streaming potential data (mV)		for Silica (1) (mV)	for Silica (2) (mV)	for PDMS (2) (mV)
KCl	0.001	0.490	-68.11	-66.16	-67.13	-86	-	-
	0.1	2.056	-38.64	-43.12	-40.88	-59	-90	-111
	1	12.12	-32.69	-29.22	-30.95	-56	-60	-90
	10	70.47	-12.25	-15.21	-13.73	-	-35	-40
PB	100	449.4	-4.64	-	-4.64	-	-	-20

The streaming current measured on the microchannels is probably mainly due to the glass charge. The PDMS is hydrophobic by nature and has a very low surface charge. When subject to the UVO treatment for sealing, the PDMS eventually becomes more hydrophilic, but the effects of the treatment do not last for long periods. Additionally, the electrodes are deposited on the glass substrate and the flow is laminar, so it is expected that only the counterions coming from the glass surface can actually exchange charge with the electrodes. This explains why the average experimental ζ -potential is lower (almost half) than expected for glass (Table). The reference ζ -potential values for PDMS are very high and probably reflect some sort of surface treatment that the polymer was subject to prior the ζ -potential measurement.

4.2. Microchannel Silanization

After proving that the streaming current measurements were robust and reflected accurately the inner surface charge of the microchannel (or at least the glass surface charge), it was time to start functionalizing the channel in order to provide it with biorecognition capabilities.

An unused channel was washed with DI water, silanized with APTES, by static incubation with a 2% (v/v) solution in acetone for 2 hours and finally washed with acetone and DI water (as described in the protocol of section 3.3). The streaming current was measured before and after the silanization, using a 10 μ l/min flow of DI water. The experiment was repeated on different channels and the average and standard deviations are represented in Figure 43.

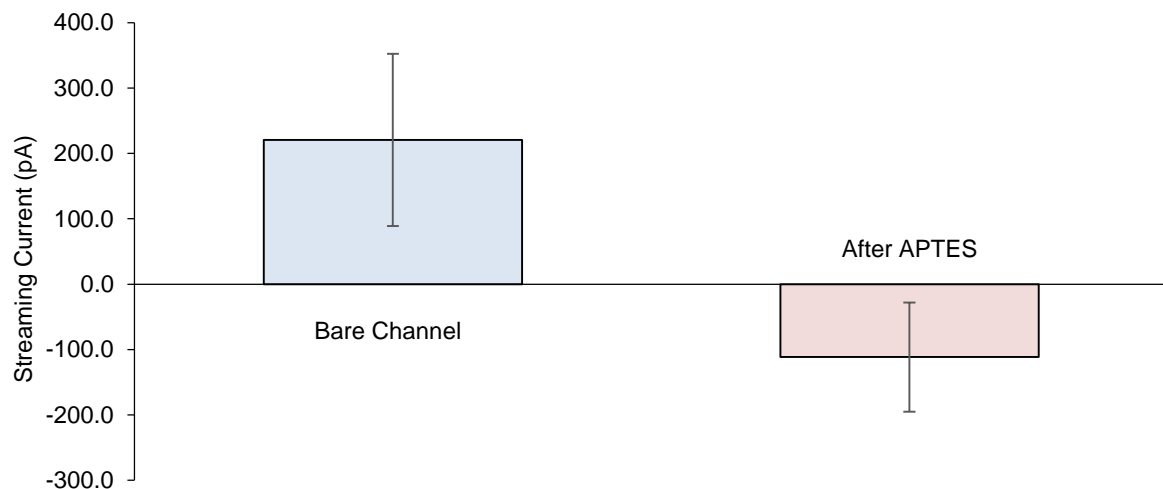


Figure 43 – Streaming current measured (DI water at 10 μ l/min) before and after the APTES silanization. The surface charge is reverted after silanization. Error bars represent the standard deviation due to 3 repetitions of the experiment, on distinct channels.

As expected, the APTES reacts with the hydroxyl groups on the surface, forming siloxane covalent bonds with the glass. The amine groups of the APTES (pK_a of about 10) are protonated when in contact with water. (Gubala, et al., 2013) Therefore, the surface is predominantly positive at pH~7, inverting the streaming current sign. At this moment, most of the surface charge is positive and, thus, the counterions are negative in nature.

The error bars are considerable, and reflect the variability on the current values between different microfluidic devices. This variability arises from differences in the alignment of the microchannels with the electrodes (manual alignment on the microscope) and, especially, from the UVO and the APTES surface treatments. As noted in the literature, charged surface groups resulting from plasma, UV, or UVO exposure can produce undesirable electrostatic interactions with the analyte molecules and excessive or poorly controlled electroosmotic flow. UV/ozone treatment was found to nearly double the ζ -potential for the channel sidewalls in polymer microfluidic chips. (Tsao & DeVoe, 2009) The time that passes between the UVO treatment and the insertion of water in the channel is another important factor that needs to be optimized if this protocol is to be used in the future.

In order to make it possible to compare the values between experiments on different microfluidic chips, one simple normalization strategy was used: all the streaming current values measured in the different steps of the functionalization/detection protocol are normalized to the value obtained for the bare (unfunctionalized) channel. This strategy was used for all the results presented from this point on.

To assess the APTES layer stability on the microchannel wall, several channels were silanized according to the protocol above, and then a series of washing steps with DI water were performed, while measuring the streaming current. The washing was performed for increasing solution flow times (up to 60 min) and for different flow rates (1 μ l/min, 5 μ l/min, 10 μ l/min and 20 μ l/min). The washing was stopped when the streaming current started to vary significantly.

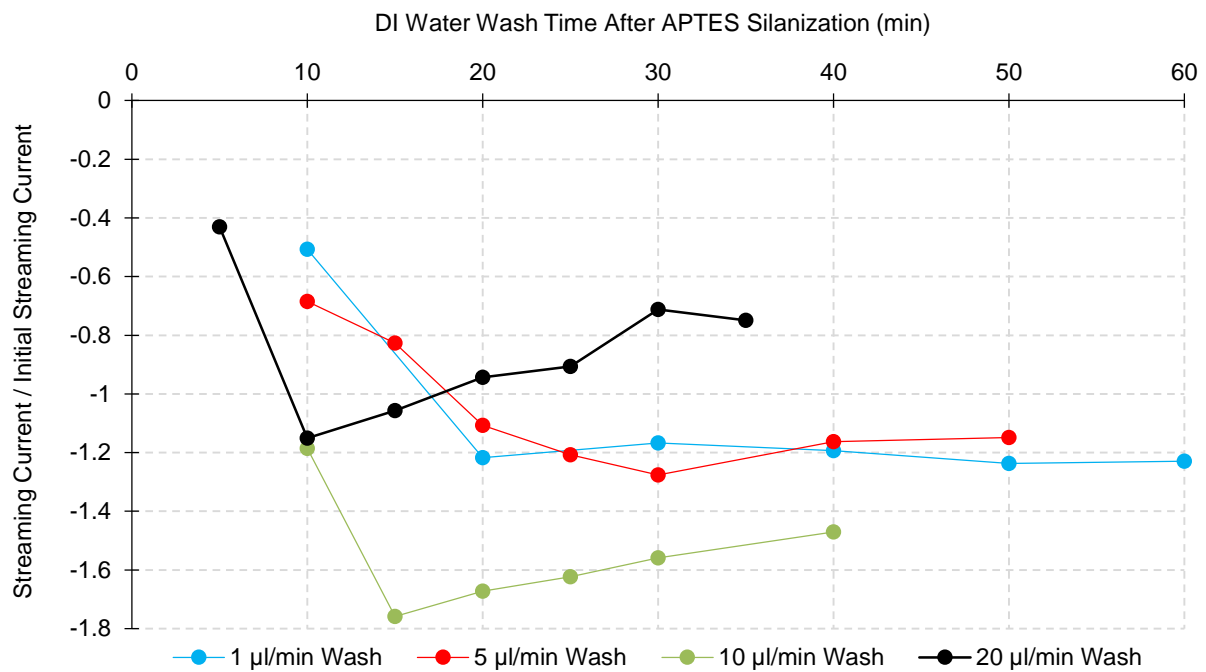


Figure 44 – Optimization of the washing conditions after APTES silanization.

From the results presented in Figure 44, it is possible to observe that for the first few minutes of washing, there is a tendency for the streaming current magnitude to increase (more negative values). This may reveal that organic solvent residues are being removed from the surface and from the bulk of the PDMS, and that APTES more loosely bound is being removed, exposing an increased number of amine groups of the APTES that is covalently bound to the surface.

For flow rates up to 5 $\mu\text{l}/\text{min}$, it is safe to say that the APTES is not removed from the surface due to extended flowing times. For both 1 $\mu\text{l}/\text{min}$ and 5 $\mu\text{l}/\text{min}$, the minimum washing time should be around 20 min. For 10 $\mu\text{l}/\text{min}$, the optimal washing time seems to be around 15 min, and above that, the APTES may start to be removed off the surface. For 20 $\mu\text{l}/\text{min}$, a 10 min wash should suffice, but above this, the APTES layer seems to deteriorate rapidly. With these results in mind, it was considered safe to perform streaming current measurements at 10 $\mu\text{l}/\text{min}$ for short periods of time.

4.3. Detection of 5 μM Target DNA

After approaching the channel silanization, a complete DNA detection experiment was performed (protocol described in detail in section 3.3). After the APTES silanization, a solution containing ssDNA probe was incubated in the channel in order to electrostatically immobilize it on the surface, which was followed by surface blocking with BSA and, finally, a 5 μM complementary target DNA (sequence identical to miR-122) solution was incubated in the channel. The experiment with the complementary target (miR-122) was performed in one microchannel, while a control experiment with a non-complementary target (miR-375) was performed using the other microchannel (each microfluidic device has two channels).

After each protocol step, a streaming current measurement and a fluorescence measurement were performed. The streaming current was measured with DI water except after the DNA target hybridization step. After hybridization, a series of reading and washing steps were performed, with decreasing PB concentrations (increasing stringency), in order to optimize the reading conditions after the hybridization. The lower the saline concentration, the higher is the electrostatic repulsion between the probe-target DNA hybrids. To some extent, this improves the specificity, but if the washing conditions are too stringent, then the target DNA may be washed away during the reading itself, yielding irreproducibility. The complete set of results for this experiment is presented below, in Figure 45.

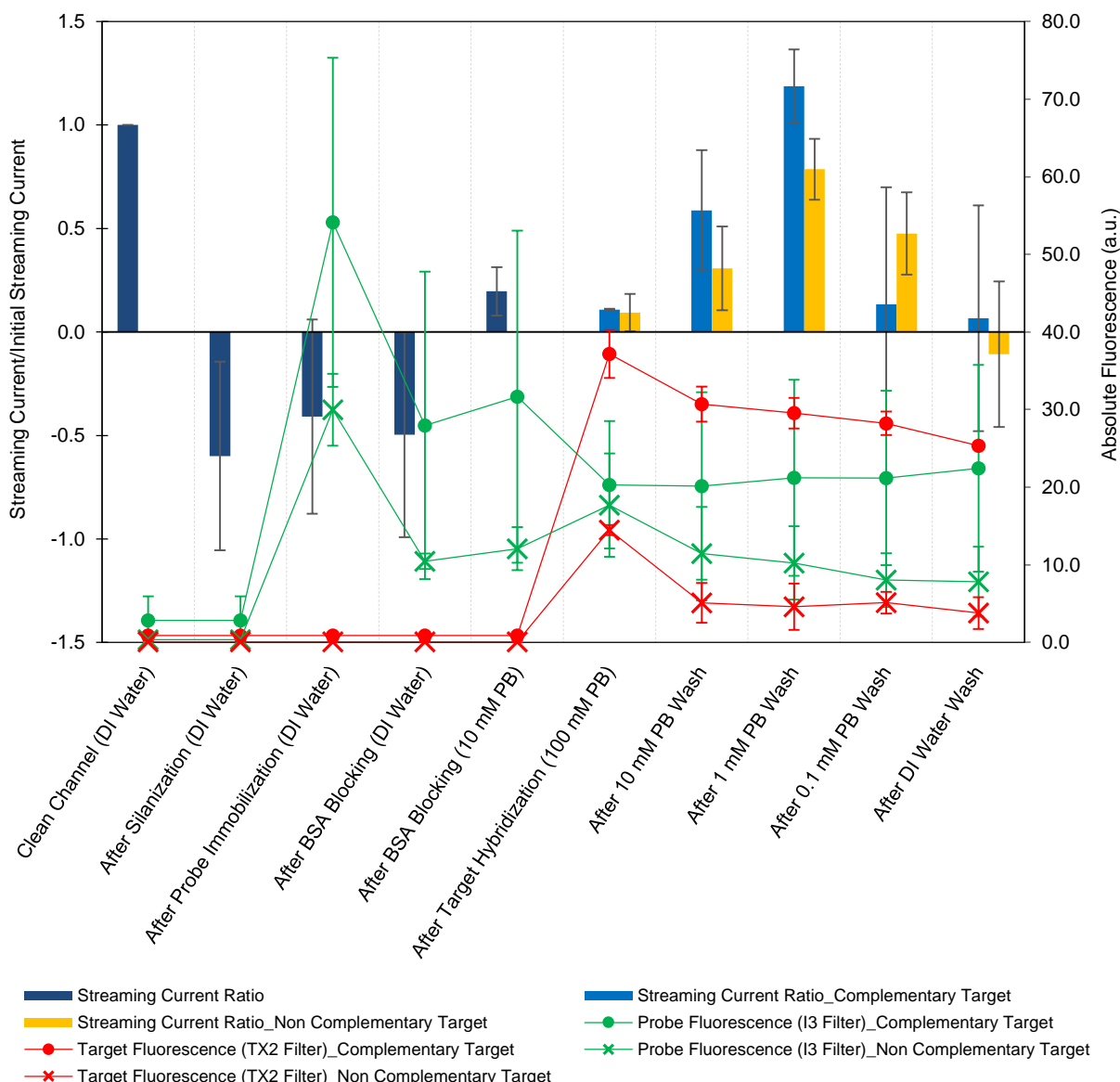


Figure 45 – Streaming current and fluorescence measurements after each functionalization step, culminating in the detection of 5 μ M of target DNA. It is possible to distinguish between a fully complementary DNA target (miR-122) and a DNA control target (miR-375). Error bars represent the standard deviation due to 3 repetitions of the experiment, in distinct channels.

The silanization step occurred normally, as described in the previous section, conferring a net positive surface charge to the surface. After incubating the ssDNA probe, the streaming current amplitude decreased slightly (a difference of 0.19 units, which corresponds to a 19% change relative to the absolute amplitude of the initial streaming current), indicating that probably only a relatively small amount of the surface was covered by the probe. Considering that all the DNA backbone phosphate groups contribute ($pK_a < 1$) with a negative charge, contrary to the APTES positive charge, the net surface charge becomes less positive, which leads to the decreasing of the streaming current amplitude. Considering that the streaming current change was only due to the addition of the DNA, a simplistic approximation for the surface coverage by the probe is 19%, right after the immobilization. It seems a reasonable value for the coverage, but the error bars associated to the readings after the silanization and after the probe immobilization are considerable, and indicate that the surface modifications are not very reproducible. As discussed before, this problem may start with the UVO treatment, and may also be due to slight temperature differences between the experiments, which were performed on different days and on different devices. The probe fluorescence (6-FAM labelled), measured with the I3 microscope filter, increases dramatically after the probe immobilization, but also has a considerable standard deviation associated, corroborating the hypothesis that the surface chemical modifications are not very reproducible. The average fluorescence for the probe on the control channels (non-complementary target) seems to be lower than that of the complementary channels, but the error bars are so high that probably this difference is not significant.

After the surface blocking with BSA, the streaming current was not significantly modified. However, the probe fluorescence decreased to about half, meaning that a significant fraction of the probe was lost after the blocking step, probably due to the competition for the surface or due to the washing with PBS after the blocking step. PBS possesses a significant ionic strength (137 mM NaCl and 10mM PB) and, as a result of which, the ions in solution may shield the APTES and the ssDNA probe charges, reducing the intensity of the electrostatic interaction and making the probe more prone to desorption from the APTES surface. Given that the fluorescence drops about 46% after the blocking, and considering the previous estimate of 19% coverage right after the probe immobilization, a rough estimate for the surface coverage after the surface blocking is of about 9%. If there is less probe on the surface but the streaming current is identical, there is an indication that BSA also contributes with a negative charge. The isoelectric point of BSA is $pI=4.7$. (Ge, et al., 1998) For DI water, at pH~6, BSA is slightly negatively charged. This, together with the fact that BSA may shield the APTES on some locations (the amine groups will not be so exposed and will not contribute with positive charge), explains why the streaming current reading didn't change considerably after the blocking step.

In order to better compare the readings before and after the target hybridization, an additional reading with PB at 10 mM (pH~7.4) was performed after the blocking with BSA. The streaming current was inverted in polarity, but the fluorescence was approximately the same, indicating that probably the constitution of the surface was not modified (i.e. no probe molecules were lost). The modification in the streaming current is most likely due to the pH increase relative to the DI water previously used. This implies that BSA will be more negatively charged, generating more positive counterions on the channel surface, and hence, a more positive streaming current value.

After the target hybridization, the streaming current values measured with 100 mM PB are very small in amplitude (as previously discussed, higher ionic strength solutions lead to a decrease in the ζ -potential and the streaming current), and cannot be used to distinguish between complementary and non-complementary targets. However, the target (DY560-labelled) fluorescence measurements, performed with the TX2 filter, are clear in distinguishing both targets, with a ratio of complementary/non-complementary equal to 2.6. The probe fluorescence on the complementary and non-complementary channels are similar.

After a more stringent wash, with 10 mM PB, the ratio of complementary/non-complementary signal in terms of fluorescence increases to 6 (see Figure 46 for fluorescence images). The decrease in the ionic strength of the solution contributed to an increase in the specificity of the assay, given that the control target, with low complementarity to the probe, got more loosely bound and more prone to wash. The amplitude of the streaming currents increased significantly and, at this point, the best complementary/non-complementary signal ratio, of about 1.9, was obtained. Looking at the error bars, one concludes that the streaming current measurements are less reproducible than the fluorescence measurements. In this work, the fluorescence was essential to complement the streaming current measurements. Temperature may play an important role in all the steps of the experiment, and, as was previously discussed for the ζ -potential, temperature changes lead to variations in the streaming current measurements.

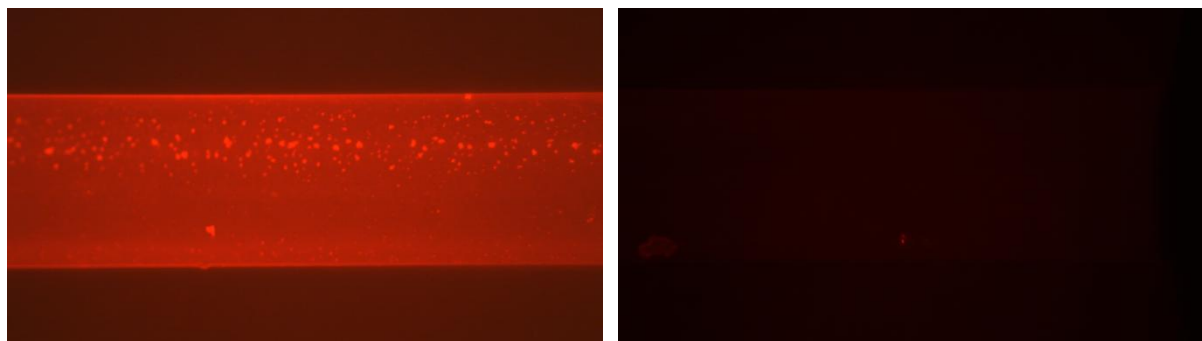


Figure 46 – Target DNA fluorescence on the functionalized microchannels, after the wash with PB at 10 mM. Complementary target (left) and non-complementary, control target (right). The complementary target signal is six times larger than the one of the non-complementary target, demonstrating specificity of the system.

At 1 mM PB, the streaming current amplitudes are even higher, the error bars are relatively smaller, but the complementary/non-complementary signal ratio in terms of the streaming current deteriorates. The fluorescence values are similar, but as the wash conditions get more stringent, there is a decrease in the complementary target fluorescence, probably due to de-hybridization of the target.

For the readings with PB at 0.1 mM and with DI water, the effects of the decrease of the pH are noticed. BSA is less negatively charged and thus, the net surface charge gets more positive, yielding more negative counterions and contributing to a more negative streaming current value. At these concentrations, the streaming current readings are not reproducible, generating large standard deviation values.

From this experiment, it was concluded that the optimal PB concentration to perform both the streaming current and the fluorescence measurements is 10 mM. It was also noticed that, with the

present surface functionalization protocol, the streaming current is at the limit of its capabilities in distinguishing between the fully complementary and the non-complementary targets. Main limiting factors are probably the temperature differences between experiments, adsorption of APTES or biomolecules to the electrodes (increased electrode resistances decrease the streaming current amplitudes and may, thus, lead to irreproducibility in the readings) and a relatively low surface coverage by the probe. Other confounding factor may exist: the fluorescence dyes (6-FAM and DY-560) might contribute with some charge, influencing the streaming current readings. If the DY-560 contributes with positive charge, contrary to the DNA charge, it decreases the sensitivity of the streaming current detection.

With the present sensitivity, the detection of miRNAs is orders of magnitude away. The range of miRNA concentrations of interest is of the order of fM to pM. Having in mind the fact that the microchannel used has a volume of 16 nL and that the 5 μ M solution containing the target molecules was incubated without flow, then, in this system, the streaming current in this particular channel can only detect 8×10^{-14} mol, where it should be sensitive to 1.6×10^{-23} mol. There is a difference of 9 orders of magnitude between the desired and the actual sensitivity level. In order to detect such low analyte concentrations in low volumes, a pre-concentration system is most likely necessary, as well as an improved surface chemistry.

4.4. Towards the Detection of Lower Target Concentrations

After the successful detection of 5 μ M, an experiment with lower DNA target concentration was performed in order to assess the sensitivity of the system. The protocol was the same, except for the target concentration that was 500 nM. Also, after the hybridization, only the measurements with 10 mM and 1 mM PB were performed, given that 10 mM was the optimal PB concentration determined in the previous experiment).

If the probe-target DNA hybrid dissociation constant is lower than 500 nM, and assuming that enough time is allowed for the DNA recognition to occur, it would be expected that even if the target concentration is decreased from 5 μ M to 500 nM, the fraction of occupied probe would still be considerable, providing a good recognition signal. In nearly all sensors, the transport of target molecules to the sensor can be as critical as the chemical reaction itself, being determinant in the resulting binding kinetics, and ultimately performance. (Squires, et al., 2008) In the case of this experiment, the mass transport is limited to convection and diffusion (the target solution was incubated without flow), which may create a zone, near the walls of the microchannel, that is depleted in terms of target molecules. Also, the time that molecules take to bind to the surface depends on the temperature. Both of these factors (incubation time and temperature) were not optimized

The results (averages and standard deviations due inter-experimental and batch variations) for the 500 nM target incubation experiment are presented in Figure 47. The trend of the streaming current and fluorescence during surface functionalization remains the same as for the previous experiment (Figure 46), so these results will not be discussed again. The main differences are detected after the target hybridization.

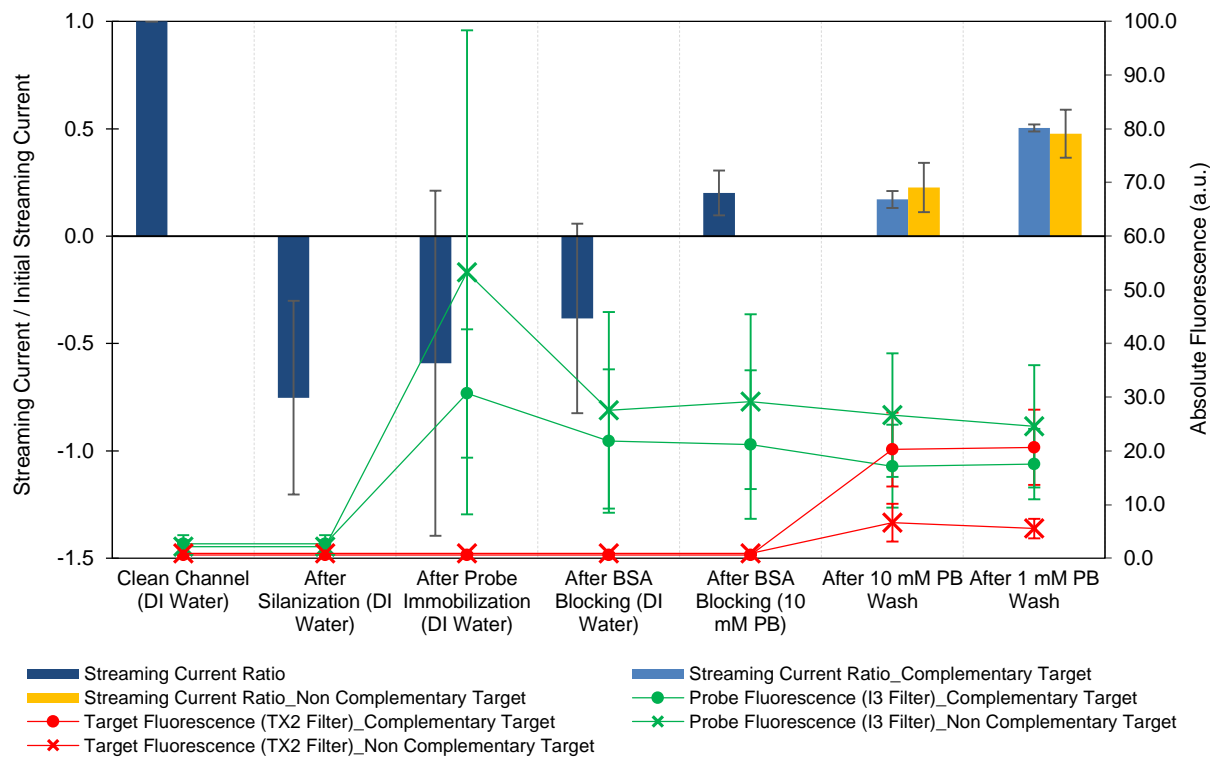


Figure 47 – Streaming current and fluorescence results of the experiment for the detection of 500 nM of target DNA by static incubation in the channel. The streaming current measurements do not distinguish between a fully complementary DNA target (miR-122) and a non-complementary DNA control target (miR-375), but fluorescence does. Error bars represent the standard deviation due to 3 repetitions of the experiment, in distinct channels.

On this experiment, after the target DNA incubation, the streaming current is similar for both fully complementary DNA target and for the negative control (non-complementary). However, the target fluorescence, measured with the TX2 filter, is still usable to distinguish between both targets. The ratio of complementary/non-complementary signal in terms of fluorescence is about 3.

Before these results, and working towards the detection of lower target DNA concentrations using the streaming current, the surface blocking step was optimized by testing different blocking agents. Also, because the target capture reaction may be limited due to target molecule depletion near the surface, flow target incubation instead of static incubation was attempted. These experiments are organized in the next sections.

4.4.1. Blocking Step Optimization

Non-specific adsorption of the non-complementary target molecules directly on the positively charged APTES surface may decrease the specificity of the detection scheme. Salmon sperm DNA was tested as blocking agent (Figure 49), and compared with BSA and with a control, using no blocking after the probe immobilization (Figure 48). The experiments were performed by using steady state target incubation (without flow), as previously. The comparison of the results after hybridization are summarized in Figure 50.

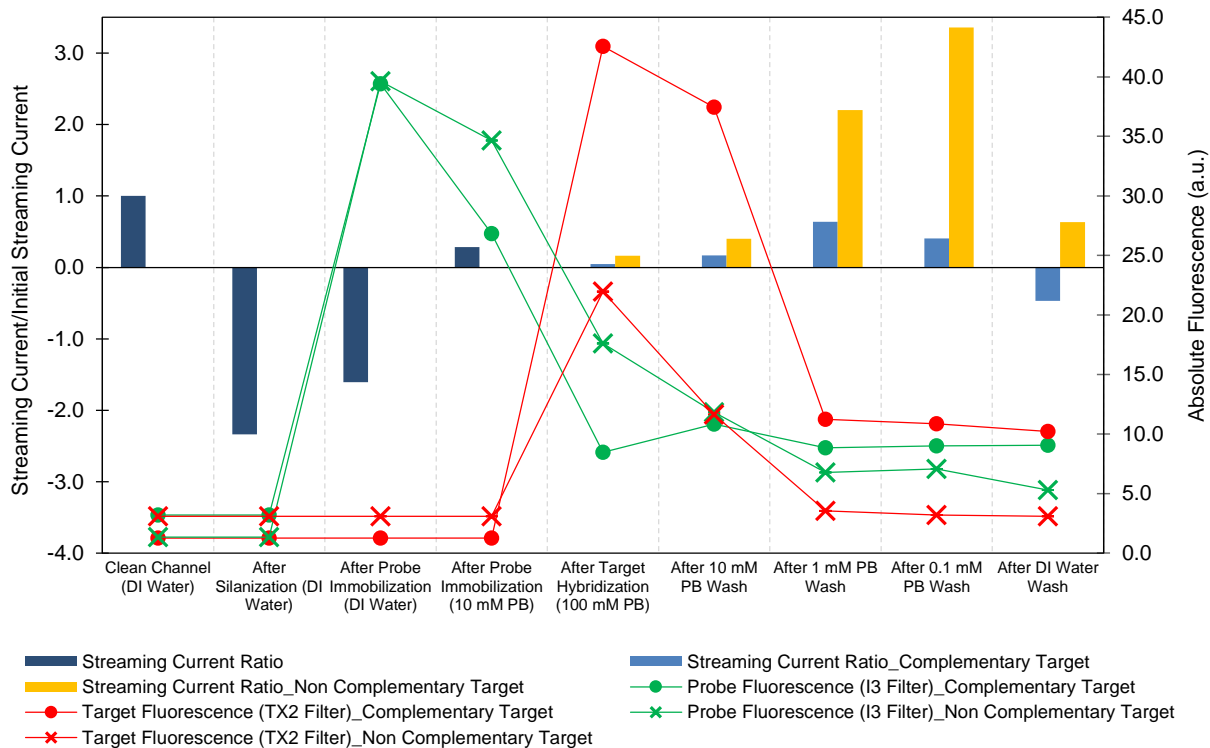


Figure 48 – Streaming current and fluorescence results of the experiment for the detection of 5 μ M of target DNA by static incubation in the channel (no surface blocking performed).

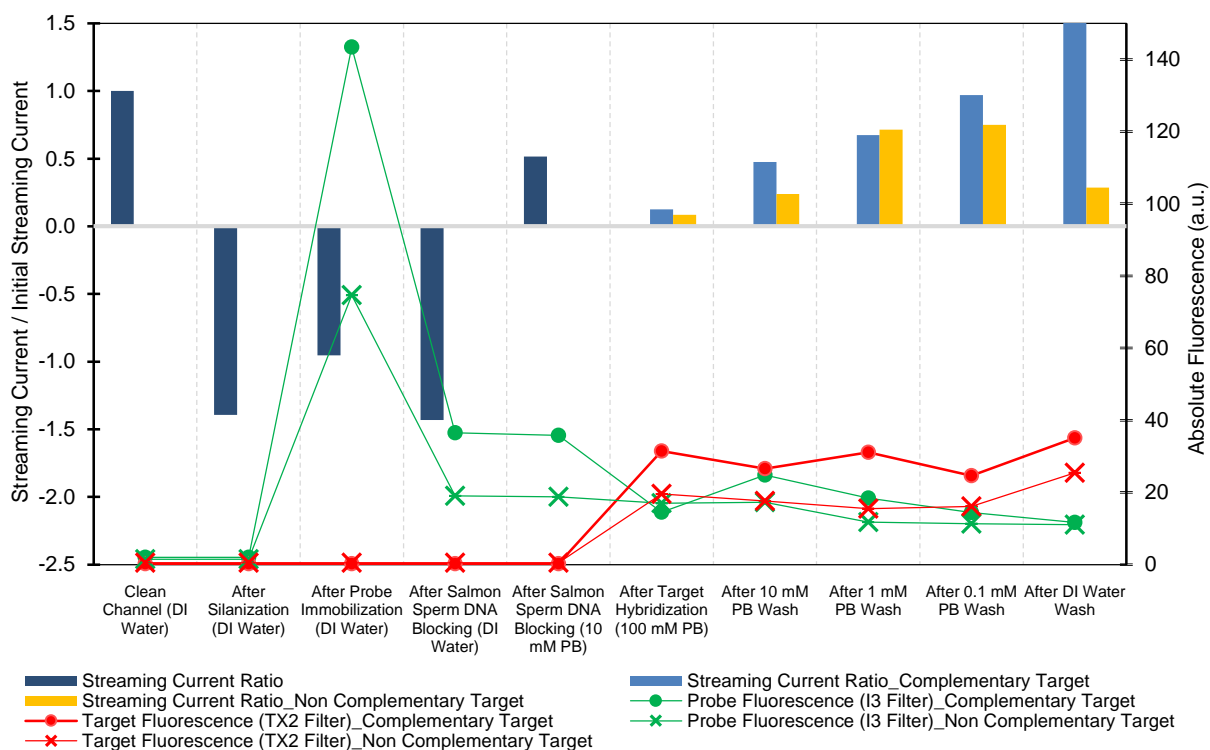


Figure 49 – Streaming current and fluorescence results of the experiment for the detection of 5 μ M of target DNA by static incubation in the channel (salmon sperm DNA blocking test).

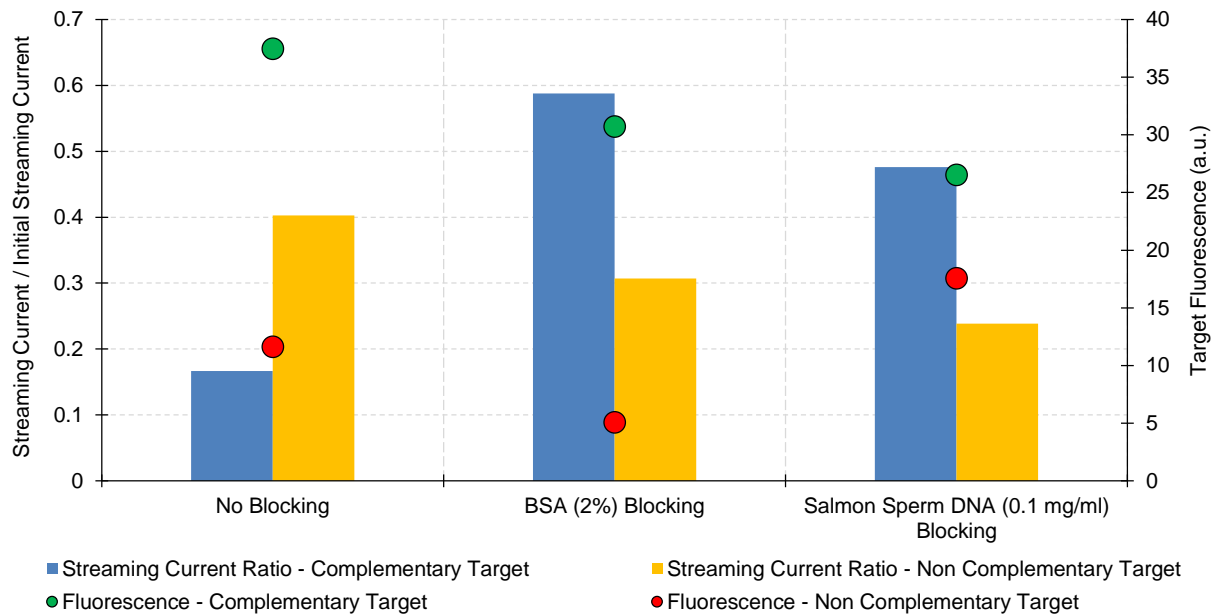


Figure 50 – BSA and salmon sperm DNA as surface blocking agents, compared with a control (no blocking). Streaming current and target fluorescence (TX2 filter) after the 10 mM PB wash step.

Regarding the experiment without the blocking step, after the immobilization there is no probe loss (10 mM PB reading after immobilization). However, probe loss occurred, when the target was incubated and washed, given that the probe fluorescence drops to less than half. The electrostatic immobilization seems to be very sensitive to the buffer. The salt in solution not only contributes to the stability of the probe-target hybrid, but also to the loss of probe due to the weakening of the electrostatic interactions between the APTES positive surface and the negative-charged DNA. The direct adsorption of the target to the surface yielded an unclear trend, in which the non-complementary target generated a higher signal than the complementary target. However, the results in terms of the fluorescence are clear in distinguishing the complementary from the non-complementary target.

With respect to the sonicated salmon sperm DNA, which contains fragments of multiple sizes, its action on the surface was quite pronounced in terms of probe loss. After the blocking step, the probe fluorescence dropped to less than one third of the value right after the probe immobilization. The salmon sperm DNA fragments are larger compared to the probe, and are also strongly attracted to the APTES surface, competing for the available surface and dislodging a considerable amount of probe. Both the electrokinetic and the optical measurements were able to distinguish both target molecules. The streaming current reading after the DI water wash, with a very high current reading for the complementary target, was probably an outlier, but as previously stated, this set of experiments should be repeated.

Looking at the comparison of the three experiments (Figure 50), the blocking agent that leads to the best complementary/non-complementary signal ratio, both in terms of the streaming current and the fluorescence, is BSA. Having reached this conclusion, BSA was used on the following experiments.

4.4.2. Steady State vs Flow Incubation

As discussed before, to avoid limiting the target capture reaction by molecule depletion near the surface (due to steady state incubation), several experiments with target incubation in flow conditions were performed. The protocol was the same as before (using BSA for blocking) except for the target incubation step that was performed at a flow rate of 0.5 $\mu\text{l}/\text{min}$ for 10 min. Experiments were performed for 5 μM and 0.5 μM target concentrations, and the results after hybridization were plotted with the previous incubation results. The error bars represent the standard deviation due to the execution of experiments in different channels and on different days.

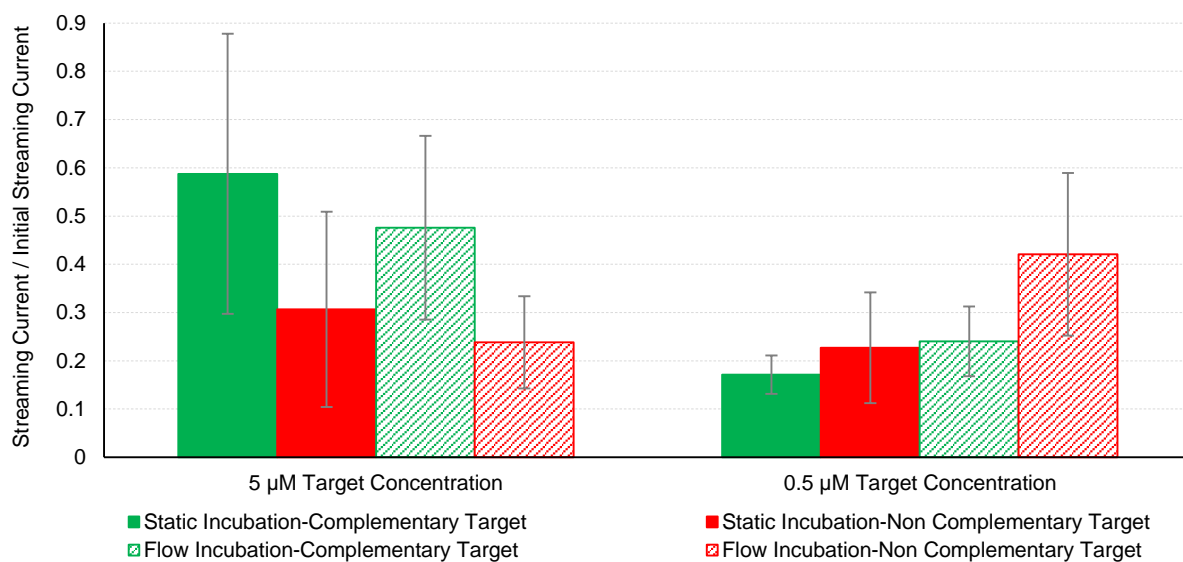


Figure 51 – Streaming current after static or flow incubation of target DNA. Readings performed with 10mM PB. The bars represent the average and the error bars the standard deviation of the individual experiments in different channels.

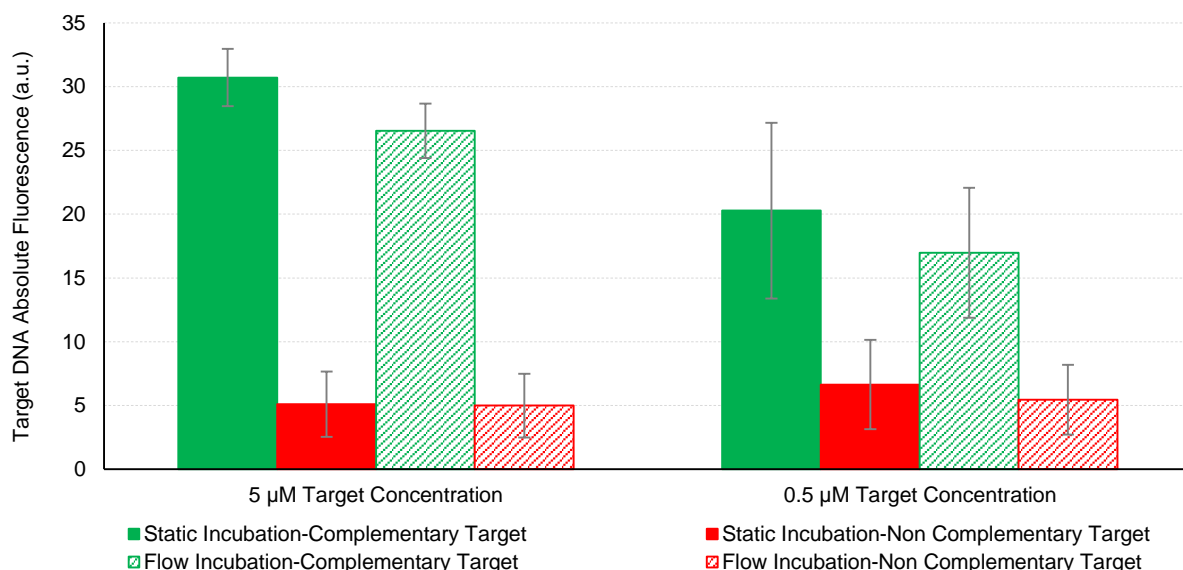


Figure 52 – Target fluorescence (TX2 filter) after static or flow incubation of target DNA. The bars represent the average and the error bars the standard deviation of the individual experiments in different channels.

The results above indicate that the target steady-state incubation and flow incubation techniques performed yield comparable results in terms of both streaming current and fluorescence. This was not expected, as a continuous flow of target molecules should contribute to saturate the immobilized probe. However, the flow conditions were not optimized and were based on the incubation conditions used by (Silva, 2013). At a flow rate of 0.5 μ l/min, the solution inside the channel was refreshed 31 times per minute. This refreshing rate should be optimized because a high flow rate may generate a considerable shear stress on the absorbed molecules and may hinder the target molecules from being recognized by the probes and settling on the surface.

Perhaps the major gap in the target DNA incubation conditions is the temperature, given that this parameter influences the reaction kinetics and the specificity of the assay. The DNA strand used as target has a length of 22 nt, a 45% CG content and a $T_m \sim 60^\circ\text{C}$ (Kibbe, 2007). Also, the target sequence has three self-annealing possibilities (Figure 53). At ambient temperature ($22\text{-}24^\circ\text{C}$), both the probe on the surface and the target in solution may be self-annealed, reducing the probability of probe-target interaction. Self-annealing could have been avoided by heating the target solution (inside the microchannel) above the melting temperature and then slowly reducing the temperature, allowing the probe-target hybrids to form. The optimization of this heating and cooling cycle should provide the system with a better sensitivity (by avoiding self-annealing) and specificity (targets with low complementarity to the probe have less tendency to bind at higher temperatures). By controlling the temperature, the salt concentration in the hybridization buffer can probably be reduced, solving the probe loss issue.



Figure 53 – miR-122 possible self-annealing sites (red).

4.4.3. DNA Surface Density Determination Using Fluorescence

In order to better describe the surface and confirm the previous estimates of the surface coverage by the ssDNA probe (coverage of about 19% after the immobilization, dropping to about 9% after the BSA blocking step), a spotting experiment was performed (see section 3.7 for the experimental details). The mean fluorescence intensity of a given region depends on the density of fluorescently labelled DNA molecules at the surface. To perform this calibration, micro spots of oligonucleotide solutions were dispensed on the surface of PDMS. If the DNA concentration and the volume of such spots are known, then it is possible to calculate the number of molecules in each spot. After imaging,

the area of the spot was calculated and it was possible to make a correlation between the molecule density (number of molecules/surface unit) and the mean fluorescence intensity of the spot.

Given the high range of concentrations spotted, the camera gain and exposure used were not constant, to avoid under- and over-exposure. Considering exposure linearity, the fluorescence values obtained were later adjusted to the scale of the conditions used in the microchannel imaging (exposure=2.0 s, gain=1). The first result obtained (Figure 54) was to verify the linearity of the exposure (e.g. doubling the exposure time or the gain doubles the fluorescence value obtained after treatment).

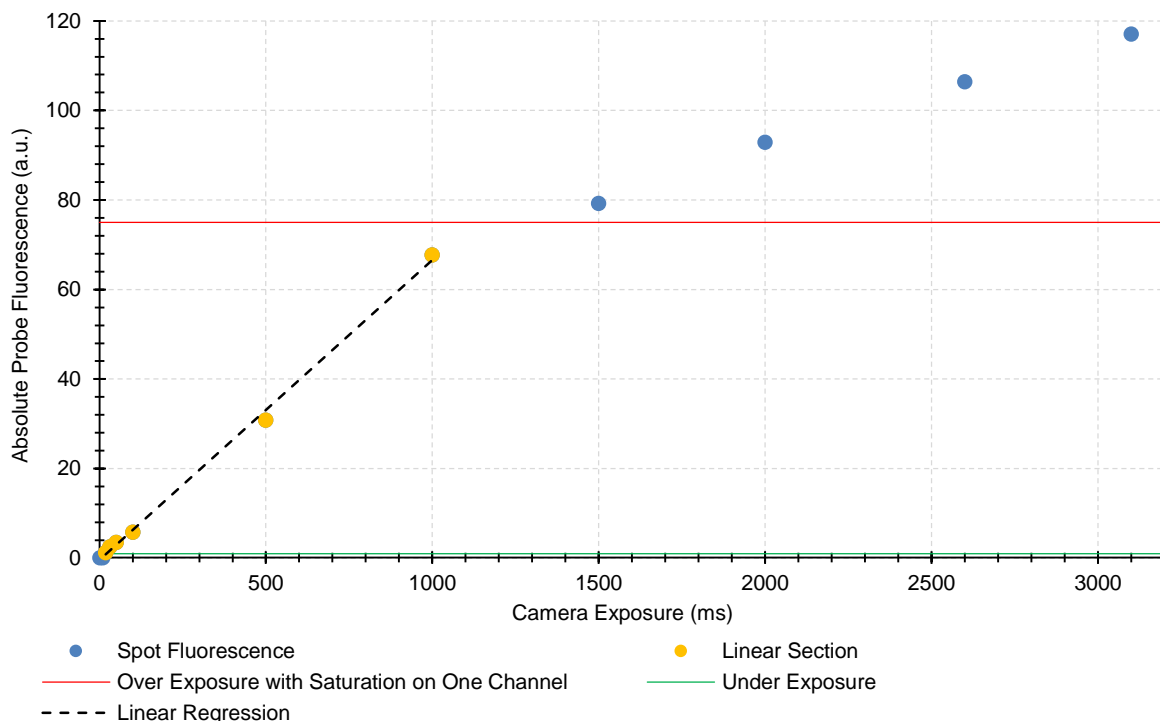


Figure 54 – Exposure linearity check. The fluorescence of one probe spot was imaged for several exposure conditions and the fluorescence intensity, after treatment on imageJ, was plotted against the exposure time. As long as there is no over exposure (saturation on at least one channel), the linearity holds good.

Given that the exposure linearity premise holds, the spot fluorescence values obtained with different exposure conditions can be adjusted to the same scale: the scale used for all the previous experiments (i.e. 2 s exposure and unitary gain). This way, it will be possible to use the fluorescence of any previous experiment to calculate the density of DNA molecules.

To calculate the DNA densities, typical dimensions of ssDNA were considered: 1 nm of width and 0.34 nm of length for each nucleotide. (Berg, et al., 2007) Given that the probe (and the target) has 22 nt, its length is of about 7.48 nm. The area of a ssDNA probe immobilized with the phosphate backbone against the APTES surface should occupy a surface of about $7.48 \times 10^{-6} \mu\text{m}^2 = 1.337 \times 10^{13} \text{ cm}^{-2}$. Thus, the surface density of a monolayer of ssDNA is around $\sigma = 1.337 \times 10^5 \mu\text{m}^{-2} = 1.337 \times 10^{13} \text{ cm}^{-2}$.

The results of the spotting experiment for the ssDNA probe are presented in Figure 55.

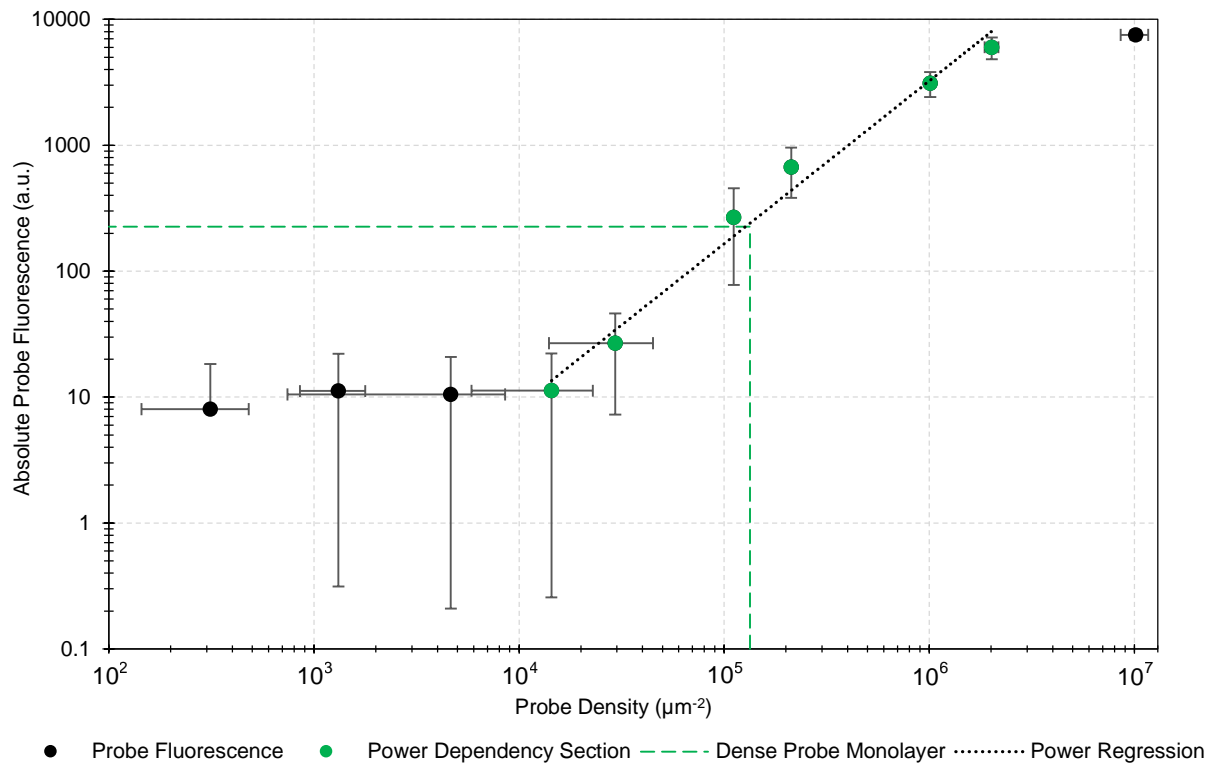


Figure 55 – Absolute probe fluorescence (I3 filter) as a function of the probe surface density. Fluorescence values adjusted to the scale of 2 s exposure, unitary gain conditions. Error bars (standard deviation) are due to spot area and fluorescence dispersion, given that each concentration was spotted 3 times.

From the plot above, it is possible to conclude that, by using the microscope setup previously described, it is not possible to detect fluorescence for ssDNA probe densities below $1.4 \times 10^4 \mu\text{m}^{-2}$. For the densities around the expected monolayer density, it was possible to make a power regression (fits better to the data than a linear regression) in order to obtain an expression to calculate the density of probe DNA molecules (σ) from the absolute probe fluorescence value (I):

$$\sigma = \left(\frac{I}{5.68 \times 10^{-5}} \right)^{\frac{1}{1.29}} \quad (16)$$

This expression was used to calculate the probe density in the experiment that detected 5 μM target DNA by incubation (section 4.3). Right after the electrostatic probe immobilization, the average probe fluorescence is 42.1 a.u., dropping to 15.8 a.u. after the BSA blocking. If we consider that these fluorescence values have the contributions from both the top and the bottom surfaces of the microchannel (given the low height of the channel), then the fluorescence corresponding to one surface is 21.03 a.u. after the probe immobilization and 7.9 a.u. after blocking. Using expression (16) to calculate the surface density, the value obtained is $2.09 \times 10^4 \mu\text{m}^{-2}$, corresponding to 15.7% of the monolayer and, after the blocking step, drops to about $9.71 \times 10^3 \mu\text{m}^{-2}$, which is 7.3% of the expected monolayer density. If the probe surface coverage was kept at levels around 15.7% thorough the whole experiment, then probably the streaming current results would have been more consistent. At 7.3% probe surface

coverage, the DNA hybridization will contribute, at most, with 7.3% more negative charge to the overall charge of the channel. As it was verified, the deviations (see the error bars on the graphs) associated with the irreproducibility of the surface functionalization steps (silanization, probe immobilization and blocking) and subsequent measurements are very significant and larger than 7.3%. The streaming current measurements are sensitive to the overall charge of the channel, and thus, a 7.3% change is hardly distinguished by this type of measurement. A higher probe surface coverage should be achieved, using a more robust and reproducible protocol.

For probe densities much higher than the one expected for the monolayer (e.g. $1 \times 10^7 \mu\text{m}^{-2}$ is a density equivalent to 100 monolayers), the fluorescence does not follow the power trend anymore. The high density of molecules on the spot seems to result in a quenching effect, and the fluorescence doesn't increase as much with the density increase as for the lower densities.

Afterwards, the calibration of the target DNA density using fluorescence was also performed. Both the complementary and the non-complementary target sequences were spotted and tested, and because the results were identical, only the results for the complementary target are presented below, in Figure 56.

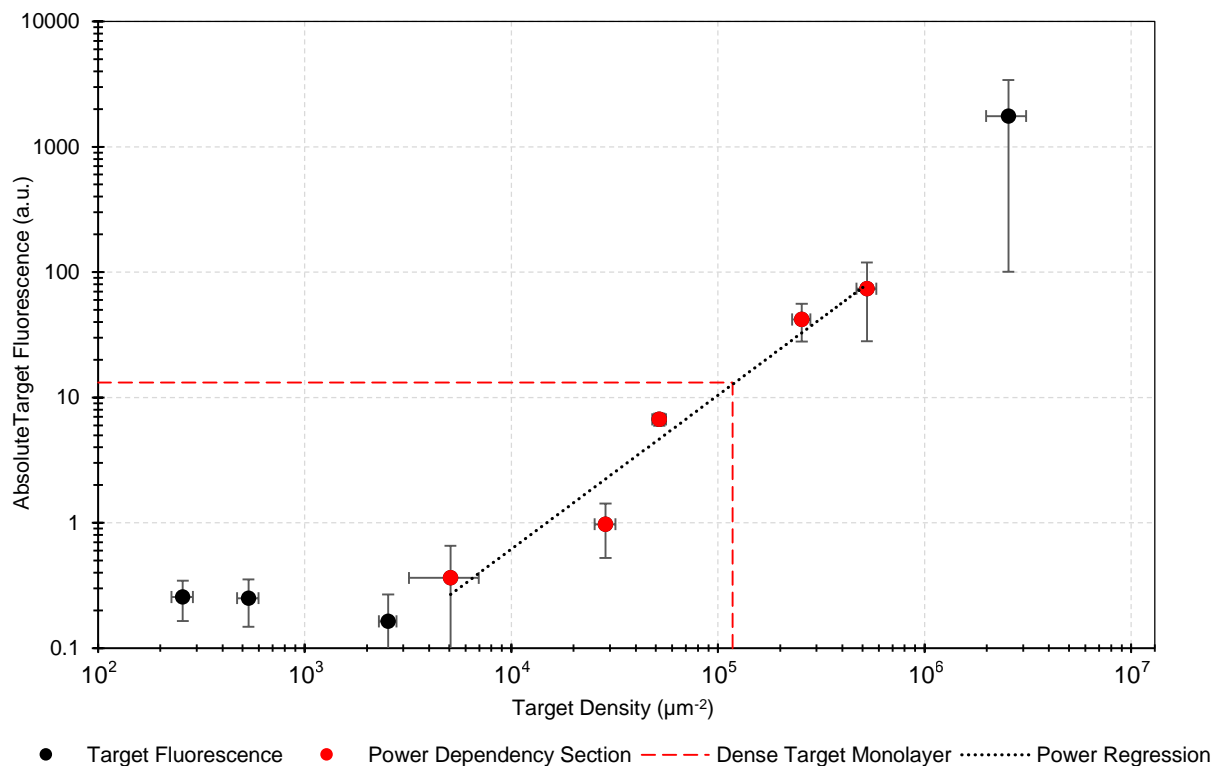


Figure 56 – Absolute target fluorescence (TX2 filter) as a function of the target surface density.

Fluorescence values adjusted to the scale of 2 s exposure, unitary gain conditions. Error bars (standard deviation) are due to spot area and fluorescence dispersion, given that each concentration was spotted 3 times.

As for the probe, there is a limit of detection regarding the target density, below which, even upon increasing the exposure or gain, it is not possible to detect any fluorescence. In this case, the inferior limit is about $5 \times 10^3 \mu\text{m}^{-2}$. When imaging densities below this, increasing the exposure will only result in background increase.

For the densities around the expected monolayer density, a power regression (fits better to the data than a linear regression) was performed in order to obtain an expression to calculate the density of target DNA molecules (σ) from the absolute target fluorescence value (I):

$$\sigma = \left(\frac{I}{7.58 \times 10^{-6}} \right)^{\frac{1}{1.23}} \quad (17)$$

The expression above was used to calculate the target density in the experiment that detected 5 μM target DNA by incubation (section 4.3). For the complementary target, the fluorescence intensity (15.4 a.u. for one surface) corresponds to a density of $1.34 \times 10^5 \mu\text{m}^{-2}$, which is higher than the one predicted for the monolayer. This density is 100.5% of the theoretical monolayer density calculated before. For the non-complementary target, the fluorescence intensity (2.1 a.u. for one surface) corresponds to a density of $2.66 \times 10^4 \mu\text{m}^{-2}$, 19.9% of the expected monolayer density.

In the best-case scenario, each probe binds one target molecule. Assuming that the probe coverage value is indeed around 7.3% (this value is identical to the one previously obtained by using the streaming current values: 9%), then at least 7.3% complementary target coverage should be obtained. Additional target coverage is due to non-specific target adsorption directly on the positive APTES surface and should occur both for the complementary and the non-complementary targets in identical amounts. If, for the non-complementary target, 19.9% of the surface was occupied by non-specifically bound target, then, for the complementary target, the surface coverage should have been around $19.9\% + 7.3\% = 27.2\%$. However, the value obtained was much higher.

The target density values calculated above seem overestimated and most likely do not correspond to the reality. Even by having extreme care in avoiding photobleaching (short exposure time on the microscope and using low ambient light), it was empirically verified that when the fluorescence of the target molecules (DY-560 labelled) was measured in solution, on the microscope, the fluorescence decreased significantly in just a few seconds. When performing measurements of molecules bound to the surface, this real-time photobleaching effect was not noticeable. With this additional information regarding the fluorophore bleaching, the results above can be explained. Considering that all the spots were bleached during the measurements on the microscope, the fluorescence intensities recorded are lower than they actually should be. Then, the whole calibration curve is shifted downwards, and the fluorescence corresponding to the monolayer is much lower (e.g. 10 instead of 100), leading to the erratic values calculated above. Thus, Figure 56 and expression (17) should not be used to derive the target molecule density from the fluorescence values obtained by imaging the surface-bound target molecules.

The calibration made above, using fluorescence as an absolute measurement for the molecule densities on the surface, can be somehow controversial, and is based on some assumptions. The first approximation is that imaging molecules adsorbed on a surface (in this case, DNA electrostatically immobilized on the surface) and on a wet drop (spot) is equivalent. On the drop, the molecules are dispersed in a considerable volume, and the height of the drop is certainly much larger than the thickness of the probe layer on the channel surface. However, the depth of field of the microscope lens is probably

high enough so that we can consider that the fluorescence of the molecules on the different planes of the spot are contributing to the final measurement. Even when imaging channels, probably both surfaces of the channel contribute to the measurements, and hence only half of the fluorescence value was considered for the calculations. Other pertinent question is whether the fluorophore dyes behave similarly when on the surface or on the spot. For the DY-560, the photobleaching effect in solution (and on the spots) was much more severe than when the molecules were immobilized on the surface, and the reason for this should be further explored. This effect was not observed for the 6-FAM labelled probe, and the calibration curve for the probe density vs fluorescence is probably accurate (the probe surface coverage obtained using fluorescence and the streaming current are similar: 7.3% and 9% of the monolayer, respectively).

5. Conclusions and Future Endeavors

5.1. Conclusions

The recent discovery of circulating miRNAs has opened the possibility to study this class of biologically active agents as biomarkers of disease. From the state-of-the-art techniques for miRNA profiling reviewed on this thesis (NB, microarrays, qRT-PCR, and NGS), qRT-PCR is probably the most suited for circulating miRNA profiling, given the analyte's scarce concentrations in the body fluids (fM). Despite their availability, these laboratory techniques are laborious, expensive and time demanding.

LOC systems may play a decisive role in the POC profiling of miRNAs for diagnostic purposes. μTAS are able to integrate multiple functional elements into a single compact device, such as pumping, flow control, filtering, separation, concentration and detection. In this thesis, an electrical label-free detection principle was explored. Transient streaming current measurements in microfluidic channels (16 nL) were used for the detection of DNA hybridization. Fluorophore-labelled DNA probe and target molecules were employed in order to use fluorescence imaging to prove the streaming current measurements.

The transient streaming current and potential measurements proved to be accurate and robust in describing the overall surface charge of the channel. Using a bare channel in contact with different saline solutions, ζ -potentials were calculated using the streaming current and the streaming potential, yielding similar results, which are comparable to values in the literature. ζ -potential values varied between -67 mV for DI Water and - 4.6 mV for 100 mM PB. The dependencies of the ζ -potential and the conductivity on the ionic concentration were discussed and compared to the literature, proving the validity of the electrokinetic measurements on the microchannel.

In order to perform the capture and recognition of the target DNA, the microchannel surface was functionalized with APTES to confer it with a positive charge. Afterwards, the negatively charged ssDNA probe was electrostatically immobilized to the APTES and the surface blocked to minimize non-specific adsorption of target molecules directly to the surface. The streaming current and fluorescence were measured, step by step, allowing to explain the evolution of the surface charge and probe coverage.

The system developed and characterized was able to distinguish between a ssDNA complementary target (miR-122 sequence) and a non-complementary control (miR-375) using both electrokinetic and optical detection methods. The streaming current measurements allowed to detect 5 μ M of target DNA while the fluorescence measurements detected down to 500 nM target DNA.

The optimal PB concentration for the transient streaming current readings was 10 mM, yielding the best complementary/non-complementary signal ratio. BSA proved to be a better blocking agent when compared to salmon sperm DNA and to a control (no blocking). Steady state incubation and flow incubation of the target DNA molecules was compared, yielding similar results. However, the flow rate and duration of the incubation was not fully optimized.

The microchannel functionalization protocol proved not to be reproducible enough for low-deviation streaming current measurements for biomolecule detection. The streaming current is sensitive to the overall charge near the surface (in a thickness of the order of the Debye length), and its measurement represents the average charge on the surface, that is due to the APTES, the ssDNA probe, BSA and the target DNA. It was proved that the density of probe molecules on the surface is relatively low. After the probe immobilization, the estimated density of molecules is $2.09 \times 10^4 \text{ } \mu\text{m}^{-2}$, corresponding to 15.7% of a dense monolayer and, after the blocking step, it dropped to about $9.71 \times 10^3 \text{ } \mu\text{m}^{-2}$, which is 7.3% of the expected monolayer density. Having these values in mind, it is safe to say that the specific target hybridization represents less than 10% of the overall channel charge, and hence, of the streaming current measurement after target hybridization. Given the errors associated to the measurements, the target hybridization contribution is marginal, which explains the large error bars associated to the streaming current measurements and the trouble in distinguishing a complementary from a non-complementary target. In this protocol, the fluorescence is obviously more specific than the streaming current because only the fluorophore-labelled DNA molecules contribute actively to the optical measurements.

5.2. Future Perspectives

A very reproducible surface functionalization protocol should be developed in order to use the electrokinetic measurements for biomolecule recognition detection. The electrostatic DNA immobilization is very sensitive to the buffer in the channel, leading to the loss of probe. An option for the probe immobilization would be to cover the microchannel surface with streptavidin, avidin, or other variants such as neutravidin, and then immobilize a biotinylated probe. In order to avoid capturing precursor miRNAs, a stem-loop-ended probe should be used. In addition, to improve the detection sensitivity by generating very stable probe-target hybrids, an LNA probe could be used instead of a DNA probe (LNA use was already discussed in the introduction). A peptide nucleic acid probe would also be a good option, given that the electrostatic repulsion between the probe and the target would be highly reduced, contributing to the enhancement of the sensitivity of the system.

The hybridization buffer as well as the reading buffer should be re-optimized by testing other buffer systems rather than PB and PBS. Tris or Tris-EDTA are probably a good choice given that Tris itself has a low salt effect, which would contribute to a less transient streaming current (the channel resistance would be higher and the conduction current, that opposes the streaming current, would be smaller). Some NaCl could be added to the Tris buffer (Tris-buffered saline), in order to improve the target capture. Besides the buffer type and salt concentrations, the flow conditions and step duration, for both the surface functionalization and the hybridization steps need to be further optimized.

There is the possibility that the APTES, DNA probe and BSA adhere to the surface of the electrodes, during the surface functionalization. In the future, it should be verified whether the adsorption of molecules to the electrodes affects or not the streaming current measurements. If it does, then future

microfluidic designs should prevent the electrodes from contacting the functionalizing solutions. The material of the electrodes should be reconsidered if the streaming current transient effect is to be avoided. A less polarizable material, with a higher ability to exchange charge with the solution, would improve the sensitivity of the current measurements.

Instead of using directly the streaming current value to study the surface modifications and the target hybridization, it may be preferable to calculate the surface charge instead. In order to calculate the density of surface charge, it is necessary to calculate the ζ -potential, which, in turn is calculated from the slope of the streaming current vs flow rate graph. This means that, for each protocol step, the measurements should be performed at different flow rates, allowing to calculate the density of surface charge.

If the internal surface of the microchannel has a less smooth topography, the surface-to-volume ratio increases and it is expected that the streaming current also increases, providing an easier measurement. This can be achieved by using different substrate materials than the ones in this work or by patterning its surface in order to increase the surface.

Regarding the integration of the electrokinetic detection method in a μ TAS, several important modifications could be included. First, instead of using an external, bench-top picoammeter, a miniaturized, integrated-circuit-based picoammeter should be used, both for portability and for low-noise measurements (avoiding the use of long cables).

Additionally, a thin-film integrated pumping system should be created. One promising idea is the use of on-chip electroosmotic pumps (electroosmosis is the converse of the streaming current). By applying a difference of potential between the extremes of the pump, the counterions will flow and drag the bulk of the liquid along the pump, due to its viscosity. The use of an integrated pump eliminates the need to manually perform connections from the chip to external bulky pumps. The microchannel height needs to be reduced, by using a thinner mould, to improve this type of pumping.

Another modification that could be introduced, perhaps one of the most important ones, is the use of an alternated fluid flow instead of a pulsed flow. The present pulsed flow imposes long waiting times and the acquisition of one measurement, repeated 3 times to allow averaging, can take one hour. If a low frequency, alternated flow was used, the polarizability effects of the electrodes would be mitigated and the reading could be performed in a matter of minutes. By reducing the reading time, the μ TAS would be fast. Also, the loss of molecules can probably be reduced by using this kind of flow. The integrated electrokinetic pumps could be used to establish such type of alternated flow.

Other important issue to be solved is the temperature control of the experiment. The reactions and the readings should occur in a tightly controlled temperature environment. By using a Peltier cell, with one of its two surfaces in contact with the microfluidic chip, inside an isolating box, and the other surface outside the enclosure, the temperature of the chip could be increased or decreased within a reasonably large range. This way, a temperature cycle could be performed while incubating the target DNA to the probe and while washing, increasing the specificity of the system.

In order to improve the sensitivity of the system and mitigate the problem of extremely low analyte concentrations (fM), an electrical miRNA pre-concentration module could be created and included in the chip. Because DNA is negatively charged, it can be separated using electrophoresis.

Electrophoresis was shown to be able to concentrate small molecules in microfluidics. (Cho, et al., 2009) Dielectrophoresis is also a good candidate technique for miRNA isolation and concentration, given that by tuning the frequency of the non-uniform electric field applied, different molecules or even cells can be attracted or repulsed based on their dielectric properties. (Asbury & Engh, 1998) (Donato, et al., 2013)

If a biological sample is to be directly inserted on the microfluidic chip, then it is possible that the sample needs to be processed, for example, for blood cell removal. This can be achieved by the use of cell traps, for example. This filtering module could be used as the first module in the microchip, followed by the pre-concentration unit and by the detection channel where the miRNA recognition and measurement occurs, all driven by included electrokinetic pumps and without external intervention.

Finally, it is easy to imagine a design with several detection channels, each one functionalized with a different probe, allowing for the profiling of different nucleic acid sequences. By introducing the above suggestions on the microfluidic system here used, a fully functional μ TAS for the detection of trace amounts of DNA could be efficiently developed, namely for the profiling of circulating miRNAs, for diagnostic purposes.

6. References

- Abaza, M. M. I., 1966. Streaming Current and Streaming Potential Induced by Water Flow Through Porous Media. *All Graduate Theses and Dissertations, Paper 1628*, <http://digitalcommons.usu.edu/etd/1628>.
- Almeida, M. I., Reis, R. M. & Calin, G. A., 2011. MicroRNA history: Discovery, recent applications, and next frontiers. *Mut Res*, 717(1-2), p. 1–8.
- Alwine, J. C., Kemp, D. J. & Stark, G. R., 1977. Method for detection of specific RNAs in agarose gels by transfer to diazobenzyloxymethyl-paper and hybridization with DNA probes. *Proc Natl Acad Sci U S A*, 74(12), p. 5350–5354.
- Arata, H., Hosokawa, K. & Maeda, M., 2014. Rapid sub-attomole microRNA detection on a portable microfluidic chip. *Anal Sci*, 30(1), p. 129-135.
- Asbury, C. L. & Engh, G. v. d., 1998. Trapping of DNA in Nonuniform Oscillating Electric Fields. *Biophys J*, 74(2 Pt 1), p. 1024-30.
- Avery, O. T., MacLeod, C. M. & McCarty, M., 1944. Studies on the Chemical Nature of the Substance Inducing Transformation of Pneumococcal Types. *J Exp Med*, 79(2), p. 137–158.
- Baldwin, R. L., 1996. How Hofmeister ion interactions affect protein stability. *Biophys J*, 71(4), p. 2056–2063.
- Bard, A. J. & Faulkner, L. R., 2001. *Electrochemical Methods-Fundamentals and Applications*. 2nd. ed. New York: John Wiley & Sons, Inc.
- Bartel, D. P., 2004. MicroRNAs: Genomics, Biogenesis, Mechanism, and Function. *Cell*, 116(2), p. 281–297.
- Benes, V. & Castoldi, M., 2010. Expression profiling of microRNA using real-time quantitative PCR, how to use it and what is available. *Methods*, 50(4), p. 244-9.
- Berg, J. M., Tymoczko, J. L. & Stryer, L., 2007. *Biochemistry*. 6th ed. New York: W. H. Freeman and Company.
- Beuvink, I. et al., 2007. A novel microarray approach reveals new tissue-specific signatures of known and predicted mammalian microRNAs. *Nucleic Acids Res*, 35(7), e52.
- Bio-Rad Laboratories, I., 2014. *qPCR/Real-Time PCR*. [Online] Available at: <http://www.bio-rad.com/en-pt/applications-technologies/qpcr-real-time-pcr> [Access: 03 06 2014].

- Biosoft, P., 2014. *TaqMan® Probes*. [Online]
Available at: http://premierbiosoft.com/tech_notes/TaqMan.html
- Blackburn, G. M., Gait, M. J., Loakes, D. & Williams, D. M., 2006. *Nucleic Acids in Chemistry and Biology*. 3rd ed. s.l.:The Royal Society of Chemistry.
- Bruus, H., 2008. *Theoretical Microfluidics*. USA: Oxford University Press.
- Castoldi, M. et al., 2006. A sensitive array for microRNA expression profiling (miChip) based on locked nucleic acids (LNA). *RNA*, 12(5), p. 913–920.
- Chen, C. et al., 2005. Real-time quantification of microRNAs by stem-loop RT-PCR. *Nucleic Acids Res*, 33(20), e179.
- Chen, X. et al., 2008. Characterization of microRNAs in serum: a novel class of biomarkers for diagnosis of cancer and other diseases. *Cell Res*, 18(10), p. 997-1006.
- Chen, Y., Gelfond, J. A., McManus, L. M. & Shireman, P. K., 2009. Reproducibility of quantitative RT-PCR array in miRNA expression profiling and comparison with microarray analysis. *BMC Genomics*, 10, p. 407.
- Chin, C. D., Linder, V. & Sia, S. K., 2012. Commercialization of microfluidic point-of-care diagnostic devices. *Lab Chip*, 12, p. 2118-2134.
- Cho, H. et al., 2009. Label-free and highly sensitive biomolecular detection using SERS and electrokinetic preconcentration. *Lab Chip*, 9(23), p. 3360-3.
- Conzone, S. D. & Pantano, C. G., 2004. Glass slides to DNA microarrays. *Mater Today*, 7(3), p. 20–26.
- Creemers, E. E., Tijssen, A. J. & Pinto, Y. M., 2012. Circulating MicroRNAs: Novel Biomarkers and Extracellular Communicators in Cardiovascular Disease?. *Circ Res*, 110(3), p. 483-495.
- Culbertson, C. T. et al., 2014. Micro Total Analysis Systems: Fundamental Advances and Biological Applications. *Anal Chem*, 86(1), p. 95–118.
- Doessing, H. & Vester, B., 2011. Locked and Unlocked Nucleosides in Functional Nucleic Acids. *Molecules*, 16, p. 4511-4526.
- Donato, S. S., Chu, V., Prazeres, D. M. F. & Conde, J. P., 2013. Metabolic viability of Escherichia coli trapped by dielectrophoresis in microfluidics. *Electrophoresis*, 34(4), p. 575-82.
- Edwards, J. M. et al., 2007. Thin film electro-osmotic pumps for biomicrofluidic applications. *Biomicrofluidics*, 1(1), p. 014101.

- Empel, V. P. M. v., Windt, L. J. D. & Martins, P. A. d. C., 2012. Circulating miRNAs: Reflecting or Affecting Cardiovascular Disease?. *Current Hypertension Reports*, 14(6), p. 498-509.
- Erickson, D., Li, D. & Werner, C., 2000. An Improved Method of Determining the zeta-Potential and Surface Conductance. *J Colloid Interface Sci*, 232(1), p. 186-197.
- Etheridge, A. et al., 2011. Extracellular microRNA: A new source of biomarkers. *Mutat Res*, 717(1-2), p. 85-90.
- Fernández, D. P., Mulev, Y., Goodwin, A. R. H. & Sengers, J. M. H. L., 1995. A Database for the Static Dielectric Constant of Water and Steam. *J. Phys. Chem. Ref. Data*, 24(1), p. 33-69.
- FitzGerald, S. P., Lamonta, J. V., McConnell, R. I. & Benchikh, E. O., 2005. Development of a High-Throughput Automated Analyzer Using Biochip Array Technology. *Clin Chem*, 51(7), p. 1165-76.
- Fluidigm Corporation, 2014. *Fluidigm - Chips and Kits*. [Online]
Available at: <http://www.fluidigm.com/chips-kits.html>
[Access: 13 06 2014].
- Garcia-Schwarz, G. & Santiago, J. G., 2013. Rapid High-Specificity microRNA Detection Using a Two-stage Isotachophoresis Assay. *Angew Chem Int Ed Engl*, 52(44), p. 11534-7.
- Ge, S., Kojio, K., Takahara, A. & Kajiyama, T., 1998. Bovine serum albumin adsorption onto immobilized organotrichlorosilane surface: influence of the phase separation on protein adsorption patterns. *J Biomater Sci Polym Ed*, 9(2), p. 131-50.
- Git, A. et al., 2010. Systematic comparison of microarray profiling, real-time PCR, and next-generation sequencing technologies for measuring differential microRNA expression. *RNA*, 16(5), p. 991-1006.
- Grier, S. H. B. & D. G., 2001. The Charge of Glass and Silica Surfaces. *J Chem Phys*, 115, p. 6716-6721.
- Gubala, V. et al., 2013. Simple approach to study biomolecule adsorption in polymeric microfluidic channels. *Anal Chim Acta*, 760, p. 75-82.
- Jang, J. S. et al., 2011. Quantitative miRNA Expression Analysis Using Fluidigm Microfluidics Dynamic Arrays. *BMC Genomics*, 12, 144.
- Kibbe, W. A., 2007. *OligoCalc: an online oligonucleotide properties calculator*. [Online]
Available at: <http://www.basic.northwestern.edu/biotools/oligocalc.html>
[Access: 10 11 2013].

- Kinet, V., Halkein, J., Dirkx, E. & DeWindt, L. J., 2013. Cardiovascular extracellular microRNAs: emerging diagnostic markers and mechanisms of cell-to-cell RNA communication. *Front Genet*, 4, p. 214.
- Kirby, B. J. & Hasselbrink, E. F., 2004. Zeta potential of microfluidic substrates: 1. Theory, experimental techniques, and effects on separations. *Electrophoresis*, 25, p. 187–202.
- Kirby, B. J. & Hasselbrink, E. F., 2004. Zeta potential of microfluidic substrates: 2. Data for polymers. *Electrophoresis*, 25, p. 203–213.
- Kong, W., Zhao, J.-J., He, L. & Cheng, J. Q., 2009. Strategies for profiling microRNA expression. *J Cell Physiol*, 218(1), p. 22-5.
- Korten, S. et al., 2013. Sample solution constraints on motor-driven diagnostic nanodevices. *Lab Chip*, 13, p. 866-876.
- Koshiol, J. et al., 2010. Strengths and Limitations of Laboratory Procedures for MicroRNA Detection. *Cancer Epidemiol Biomarkers Prev*, 19(4), p. 907-11.
- Kruhøffer, M. et al., 2007. Isolation of Microarray-Grade Total RNA, MicroRNA, and DNA from a Single PAXgene Blood RNA Tube. *J Mol Diagn*, 9(4), p. 452–458.
- Kuczenski, R. S., Chang, H.-C. & Revzin, A., 2011. Dielectrophoretic microfluidic device for the continuous sorting of Escherichia coli from blood cells. *Biomicrofluidics*, 5(3), p. 032005–032005-15.
- Lameiras, F. S. et al., 2008. Measurement of the zeta potential of planar surfaces with a rotating disk. *Mat. Res*, 11(2), p. 217-219.
- Lange, J., 2010. microRNA profiling on automated biochip platform reveals biomarker signatures from blood samples (Advertising Feature). *Nature Methods*, 7, Application Notes.
- Laterza, O. F. et al., 2009. Plasma MicroRNAs as sensitive and specific biomarkers of tissue injury. *Clin Chem*, 55(11), p. 1977-83.
- Lawrie, C. et al., 2008. Detection of elevated levels of tumour-associated microRNAs in serum of patients with diffuse large B-cell lymphoma. *Br J Haematol*, 141, p. 672–675.
- Lee, R. C., Feinbaum, R. L. & Ambros, V., 1993. The *C. elegans* Heterochronic Gene lin-4 Encodes Small RNAs with Antisense Complementarity to lin-14. *Cell*, 75(5), p. 843–854.
- Lewis, P. J. S. et al., 2011. Circulating microRNAs as potential markers of human drug-induced liver injury. *Hepatology*, 54(5), p. 1767-76.
- Li, D., 2004. *Electrokinetics in Microfluidics*. UK: Elsevier Ltd.

Liu, C.-G., Spizzo, R., Calin, G. A. & Croce, C. M., 2008. Expression profiling of microRNA using oligo DNA arrays. *Methods*, 44(1), p. 22-30.

Liu, J., Jennings, S. F., Tong, W. & Hong, H., 2011. Next generation sequencing for profiling expression of miRNAs: technical progress and applications in drug development. *J Biomed Sci Eng*, 4(10), p. 666–676.

Liu, L. et al., 2012. Comparison of Next-Generation Sequencing Systems. *J Biomed Biotechnol*, vol. 2012, Article ID 251364, 11 pages.

Lundblad, R., 2003. Considerations for the Use of Blood Plasma and Serum for Proteomic Analysis. *The Internet Journal of Genomics and Proteomics*, Volume 1, Number 2.

MacPherson, M. J. & Ravichandiran, M., 2011. Lab-on-a-chip technology: the future of point-of-care diagnostic ability. *UWOMJ*, 80(1), p. 24-26.

Martins, D. C., Chu, V., Prazeres, D. M. F. & Conde, J. P., 2011. Electrical detection of DNA immobilization and hybridization by streaming current measurements in microchannels. *Appl. Phys. Lett.*, 99, 183702.

Martins, D. C., Chu, V., Prazeres, D. M. F. & Conde, J. P., 2013. Streaming currents in microfluidics with integrated polarizable electrodes. *Microfluid Nanofluid*, 15, p. 361–376.

Maxam, A. M. & Gilbert, W., 1977. A new method for sequencing DNA. *Proc Natl Acad Sci U S A*, 74(2), p. 560–564.

Ma, Y. et al., 2013. Genome-wide sequencing of cellular microRNAs identifies a combinatorial expression signature diagnostic of sepsis. *PLoS One*, 8(10), e75918.

Mestdagh, P. et al., 2009. A novel and universal method for microRNA RT-qPCR data normalization. *Genome Biol*, 10(6), R64.

Meyer, S. U., Pfaffl, M. W. & Ulbrich, S. E., 2010. Normalization strategies for microRNA profiling experiments: a ‘normal’ way to a hidden layer of complexity?. *Biotechnol Lett*, 32(12), p. 1777-88.

Micro Magnetics, I., 2014. *Magnetron Sputtering Technology*. [Online]
Available at: <http://www.directvacuum.com/sputter.asp>
[Access: 09 06 2014].

Mitchell, P. S. et al., 2008. Circulating microRNAs as stable blood-based markers for cancer detection. *Proc Natl Acad Sci U S A*, 105(30), p. 10513-8.

Mohr, P. J., Taylor, B. N. & Newel, D. B., 2012. CODATA Recommended Values of the Fundamental Physical Constants: 2010. *Rev. Mod. Phys.*, 84, 1527.

Moltzahn, F. et al., 2011. High throughput microRNA profiling: optimized multiplex qRT-PCR at nanoliter scale on the fluidigm dynamic arrayTM IFCs. *J Vis Exp.*, (54), p. 2552.

Moltzahn, F. et al., 2011. Microfluidic based multiplex qRT-PCR identifies diagnostic and prognostic microRNA signatures in sera of prostate cancer patients. *Cancer Res.*, 71(2), p. 550–560.

Motameny, S., Wolters, S., Nürnberg, P. & Schumacher, B., 2010. Next Generation Sequencing of miRNAs – Strategies, Resources and Methods. *Genes*, 1(1), p. 70-84.

Novo, P., Volpetti, F., Chu, V. & Conde, J. P., 2013. Control of sequential fluid delivery in a fully autonomous capillary microfluidic device. *Lab Chip*, 13, p. 641-645.

Patnaik, S. K. et al., 2012. MicroRNA Expression Profiles of Whole Blood in Lung Adenocarcinoma. *PLoS ONE*, 7(9), e46045.

Peltier, H. J. & Latham, G. J., 2008. Normalization of microRNA expression levels in quantitative RT-PCR assays: Identification of suitable reference RNA targets in normal and cancerous human solid tissues. *RNA*, 14(5), p. 844–852.

Puchberger-Engl, D. et al., 2011. Microfluidic concentration of bacteria by on-chip electrophoresis. *Biomicrofluidics*, 5(4), p. 044111–044111-10.

Reid, G., Kirschner, M. B. & Zandwijk, N. v., 2011. Circulating microRNAs: Association with disease and potential use as biomarkers. *Critical Reviews in Oncology/Hematology*, 80, p. 193–208.

Reinke, V., 2006. *Germline genomics*, *The C. elegans Research Community, WormBook*, doi/10.1895/wormbook.1.74.1. [Online]
Available at: <http://www.wormbook.org>
[Access: 29 05 2014].

Rivet, C. et al., 2011. Microfluidics for medical diagnostics and biosensors. *Chemical Engineering Science*, 66, p. 1490–1507.

Roderburg, C. et al., 2013. Circulating MicroRNA-150 Serum Levels Predict Survival in Patients with Critical Illness and Sepsis. *PLoS ONE*, 8(1), e54612.

Sanger, F., Nicklen, S. & Coulson, A. R., 1977. DNA sequencing with chain-terminating inhibitors. *Proc Natl Acad Sci U S A*, 74(12), p. 5463–5467.

Schmittgen, T. D., Jiang, J., Liu, Q. & Yang, L., 2004. A high-throughput method to monitor the expression of microRNA precursors. *Nucleic Acids Res.*, 32(4), e43.

- Schöler, N. et al., 2010. Serum microRNAs as a novel class of biomarkers: a comprehensive review of the literature. *Exp Hematol*, 38(12), p. 1126-30.
- Shi, R. & Chiang, V. L., 2005. Facile means for quantifying microRNA expression by real-time PCR. *Biotechniques*, 39(4), p. 519-25.
- Silva, M., 2013. Detection of circulating miRNAs using microfluidics – a diagnostic method for cardiovascular diseases. Biotechnology M.Sc. Thesis. *Instituto Superior Técnico, Portugal*.
- Squires, T. M., Messinger, R. J. & Manalis, S. R., 2008. Making it stick: convection, reaction and diffusion in surface-based biosensors. *Nat Biotechnol*, 26(4), p. 417-426.
- Sze, A., Erickson, D., Ren, L. & Li, D., 2003. Zeta-potential measurement using the Smoluchowski equation and the slope of the current–time relationship in electroosmotic flow. *Journal of Colloid and Interface Science*, 261, p. 402–410.
- Tang, F. et al., 2006. 220-plex microRNA expression profile of a single cell. *Nat Protoc*, 1(3), p. 1154-9.
- Tran, N., 2009. Fast and Simple micro-RNA Northern Blots. *Biochemistry Insights*, 2, p. 1-3.
- Tsao, C.-W. & DeVoe, D. L., 2009. Bonding of thermoplastic polymer microfluidics. *Microfluid Nanofluid*, 6(1), p. 1–16.
- United States National Library of Medicine, 2013. *MeSH Heading: Biological Markers*. [Online] Available at: http://www.nlm.nih.gov/cgi/mesh/2014/MB_cgi?mode=&index=14733 [Access: 10 12 2013].
- Vasan, R., 2006. Biomarkers of Cardiovascular Disease: Molecular Basis and Practical Considerations. *Circulation*, 113, p. 2335-2362.
- Wang, H., Ach, R. A. & Curry, B., 2007. Direct and sensitive miRNA profiling from low-input total RNA. *RNA*, 13(1), p. 151–159.
- Wang, K. et al., 2012. Comparing the MicroRNA Spectrum between Serum and Plasma. *PLoS ONE*, 7(7), e41561.
- Wang, K. et al., 2009. Circulating microRNAs, potential biomarkers for drug-induced liver injury. *Proc Natl Acad Sci U S A*, 106(11), p. 4402-7.
- Wang, W. et al., 2014. High-Pressure Open-Channel On-Chip Electroosmotic Pump for Nanoflow High Performance Liquid Chromatography. *Anal Chem*, 86(4), p. 1958–1964.
- Wang, X., Cheng, C., Wang, S. & Liu, S., 2009. Electroosmotic pumps and their applications in microfluidic systems. *Microfluid Nanofluidics*, 6(2), p. 145.

- Watson, J. & Crick, F., 1953. Molecular structure of nucleic acids; a structure for deoxyribose nucleic acid. *Nature*, 171(4356), p. 737-8.
- Weston, M. C., Nash, C. K. & Fritsch, I., 2010. Redox-Magnetohydrodynamic Microfluidics Without Channels and Compatible with Electrochemical Detection Under Immunoassay Conditions. *Anal Chem*, 82(17), p. 7068–7072.
- Wightman, B. et al., 1991. Negative regulatory sequences in the lin-14 3'-untranslated region are necessary to generate a temporal switch during *Caenorhabditis elegans* development. *Genes & Dev.*, 5, p. 1813-1824.
- Wightman, B., Ha, I. & Ruvkun, G., 1993. Posttranscriptional regulation of the heterochronic gene lin-14 by lin-4 mediates temporal pattern formation in *C. elegans*. *Cell*, 75(5), p. 855-62.
- Willenbrock, H. et al., 2009. Quantitative miRNA expression analysis: Comparing microarrays with next-generation sequencing. *RNA*, 15(11), p. 2028-34.
- Wu, M. et al., 2013. Single Cell MicroRNA Analysis Using Microfluidic Flow Cytometry. *PLoS One*, 8(1), e55044.
- Yin, J. Q., Zhao, R. C. & Morris, K. V., 2008. Profiling microRNA expression with microarrays. *Trends Biotechnol*, 26(2), p. 70-6.
- Yu, Z. et al., 2011. Differences between Human Plasma and Serum Metabolite Profiles. *PLoS ONE*, 6(7), e21230.
- Zeng, Y., 2006. Principles of micro-RNA production and maturation. *Oncogene*, 25, p. 6156–6162.
- Zhao, Z. et al., 2012. Circulating microRNA miR-323-3p as a biomarker of ectopic pregnancy. *Clin Chem*, 58(5), p. 896-905.
- Zipper, H., Brunner, H., Bernhagen, J. & Vitzthum, F., 2004. Investigations on DNA intercalation and surface binding by SYBR Green I, its structure determination and methodological implications. *Nucleic Acids Res*, 32(12), e103.

7. Annexes

7.1. Run Sheet – Aluminium Hard Mask Fabrication

Responsible: Rui Pinto, 62842

STEP 1: Substrate Cleaning

Date: 2013/09/04

Operator: Rui Pinto

Machine: Wet Bench (Ultrasounds)

Substrate: Glass (thickness=0.5mm)

Conditions: - Clean for 30 minutes in Alconox solution with ultrasounds

- Clean for 30 minutes in DI water with ultrasounds

- Clean with IPA, DI water and blow dry with compressed air gun.

STEP 2: 3000A Aluminium Deposition

Date: 2013/09/04

Operator: Pedro Novo; Rui Pinto

Machine: N7000 (Magnetron sputtering)

Thickness: 1000A

- Module 4: Al deposition
- Sequence: Al 1000A
- Function 1

Conditions:

Chamber pressure before deposition: _____ Torr

Chamber pressure during deposition: 1.8E-3 Torr

Subst Rotn: 30 rpm

Readpoint:

P = 2kW

V = 402V

I = 5A

Side View (After Deposition):

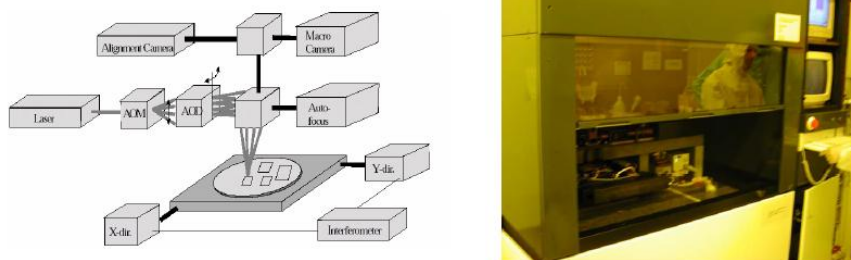


STEP 3: Microchannel shape definition - DWL

Date: 2013/09/09

Operator: Virgínia Soares

Machine: DWL (Direct Write LASER)



Coating conditions:

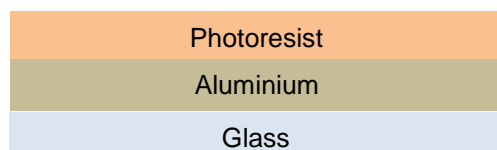
- Vapour prime (5min HDMS) @ 130 ° C (program 0):
 - deposition of an adhesive monolayer of HDMS (gas phase)
HDMS: hexamethyldisilazane [(CH₃)₃Si]₂NH (adhesive promoter for PR)
 - use program zero (5 min HDMS)
 - press reset and then start
 - check if pressure drops
 - make sure 41-42 appears on the display before taking the sample out

Step duration~30 min

- Resist Coating

- Paste the substrate to a Si wafer with yellow tape on the four corners
- Put the wafer on the SVG track for coating
- Photoresist: Coater 6/2
 - 2.5 krot/min
 - 1.5um resist thickness
 - baking at 85°C for 1 min.

Side View (After Coating):



Exposing Conditions:

Mask name: streaming_current_2013_1.dwg

Layer: PDMS

Server File for DWL: strcurrmask

Map: 1 die

Die dimensions: [X: 13795.3137 Y: 15212.9805] um

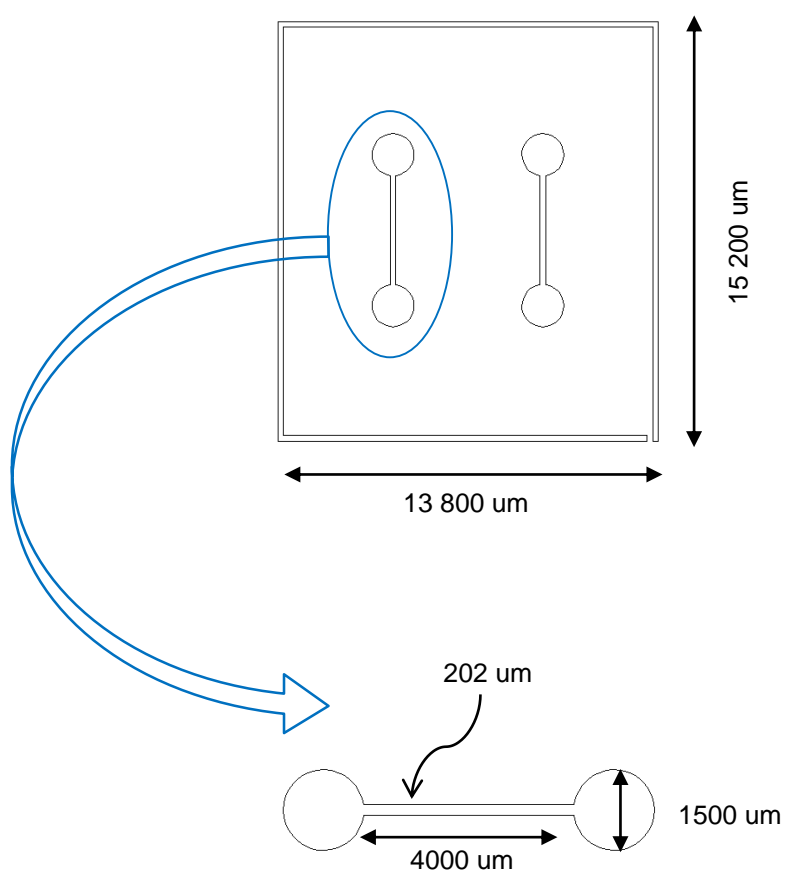
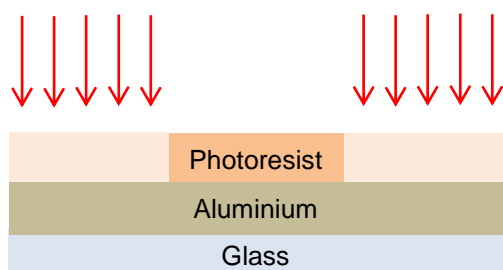
Alignment marks: none

Focus:

Energy:

Offset:

Mask top view:

**Side View (Exposure):**

Development: recipe: 6-2

- Put the Si wafer on the SVG track for development
- Conditions:
 - 1 minute at 110°C
 - Development for 1 minute (program 2)

After the normal development, the sample is inspected with cleanroom microscope aid (be sure the filter is on). Overdevelop if necessary.

Overdevelopment: not necessary

Side View (After Development):**STEP 3: Aluminium Etching by Wet Etch****Date:** 2013/09/09**Operator:** Rui Pinto, Jorge Santos**Machine:** Wet Bench

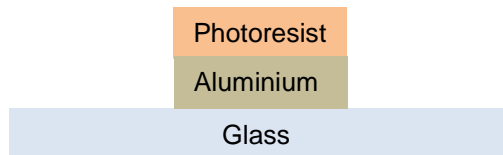
- Aluminium Etchant is Isotropic and Selective
- Expected Etch Rate: 50-100nm/min
- Thickness to be etched: 100nm
- Time: 4min (includes over etch)
- Verify the etching is complete, otherwise, over etch.

Conditions:

- Ambient Temperature
- Manual Agitation
- No Dilution

Etchant: Technic Aluminium Etchant Micropur MOS**Batch:** 020194

Side View (after etching):



STEP 6: Resist Stripping

Date: 2013/09/09

Operator: Rui Pinto, Jorge Santos

Machine: Wet Bench

Conditions:

- Microstrip 3001 @ 60 °C
- Duration: 10 min
- Clean with IPA and DI water
- Blow dry with N₂ stream

Side View:



7.2. Run Sheet – SU-8 Mould Fabrication

Responsible: Rui Pinto, 62842

STEP 1: Substrate (Si) Cleaning

Date: 2013/09/10

Operator: Rui Pinto

Machine: Wet Bench (Ultrasounds)

Conditions:

- Rub with acetone to remove photoresist
- Alconox, 15 min, 65°C
- Clean with DI water and IPA
- Blow dry with compressed air gun.

STEP 2: SU-8 Coating, UV Exposure and Development

Date: 2013/09/10

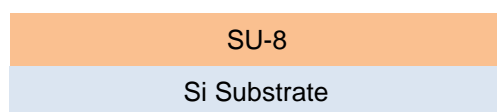
Operator: Rui Pinto, Narayanan Srinivasan

Machine: Spinner

- Protect the spinner with thin foil to avoid photoresist spilling
- Turn on the bench power and vacuum pump
- Open the vacuum and N₂ valves
- Turn on the spinner
- Press Edit Mode and go to program 19 or 20 (because the first programs are reserved)
- Edit the spinning steps on the spinner menu:
 - Spin at 500 rpm for 10 seconds with acceleration of 100 rpm/second
 - Spin at 1700 rpm for 34 seconds with acceleration of 300 rpm/second
- Put the substrate on the spinner and press the vacuum button. Make sure that the substrate is fixed
- Pour the SU-8 (2015) on the Si substrate
- Press Run Mode, Press Run
- After the spin coating, heat on hot plate at 95 °C for 4 min (soft bake)
- Cool down to room temperature (minimum 2 min)

Desired SU-8 Thickness: 20um

Side View (After Coating):

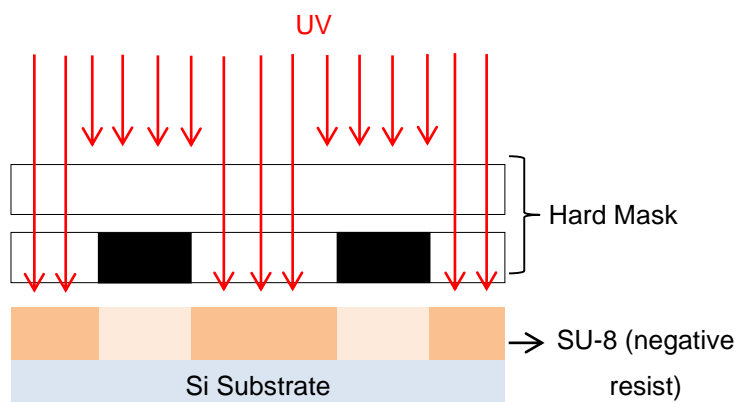


Machine: UV Light Box

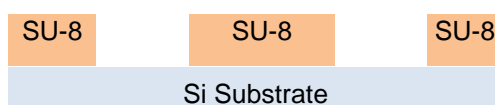
- Paste the substrate and the hard mask to the light box support.
- Insert the UV filter and the substrate holder on the respective slots.
- Remove the filter and start counting the time: 25 to 29 seconds UV exposure
- Insert the filter and remove the substrate holder
- Remove the substrate and hard mask from the holder
- Heat the substrate on a hot plate: 5 min at 95 °C (Post-exposure Bake)
- Cool down (minimum 2 min)

Comments:

Turn UV lamp on 30 minutes before use (wear UV goggles) and let people know you are using the UV lamp.

Side View (Exposure):**Development:**

- Development of the SU-8 by immersing the sample in PGMEA (mild agitation for 2min)
- Check if the development is complete. If it is not, keep developing.
- When developing is complete, clean with IPA and blow dry (don't point the IPA squirt directly to the SU-8 structure!!!)
- Hard-bake at 150 °C for 15 min

Side View (After Development):

- Verify SU-8 mould thickness on the profilometer:

7.3. Run Sheet – PDMS Microchannel Fabrication

Responsible: Rui Pinto, 62842

STEP 1: PDMS Preparation

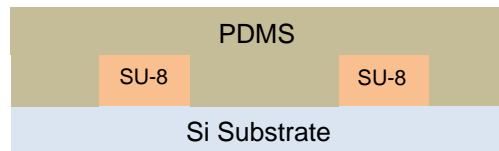
Date: 2013/09/10

Operator: Rui Pinto

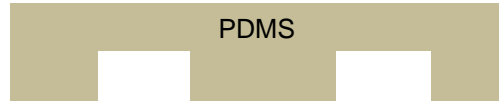
Machine: Wet Bench

- Sylgard 184: Mix 10:1 (w/w) (base:curing agent)
- Mix base and curing agent for 5 minutes
- Clean the mixing tool with isopropanol (IPA)
- Put in vacuum for air bubbles extraction (~40 min)
- Dispense PDMS on the moulds
- Cure in the oven: 70°C for 2hours

Side View (PDMS on the mould):



Side View (after curing):



- Manually punch the inlet and outlet holes

STEP 2: Irreversible surface bonding

Date:

Operator: Rui Pinto

Machine: Wet Bench

- Clean the glass (containing the electrodes) and the PDMS with IPA and blow dry

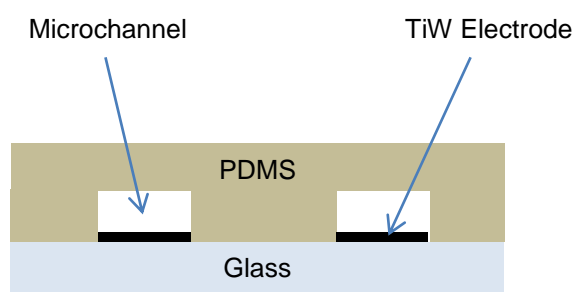
Machine: UVO (11 min)

- 6 min UV+Ozone
- 5 min for ozone exhaustion

- Press the PDMS and the glass together

- Dry for 30 min @ 70°C

Side View (After Sealing):



7.4. Run Sheet – TiW Electrode Fabrication

Responsible: Rui Pinto, 62842

STEP 1: Substrate Cleaning

Date: 2013/09/13

Operator: Rui Pinto

Machine: Wet Bench (Ultrasounds)

Substrate: Glass (thickness=0.5mm)

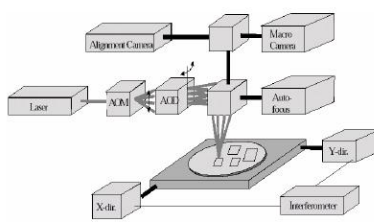
- Conditions:
- Clean for 30 minutes in Alconox solution with ultrasounds;
 - Clean for 30 minutes in DI water with ultrasounds;
 - Clean with IPA and blow dry with compressed air gun.

STEP 2: Electrode Shape Definition

Date: 2013/09/13

Operator: Virgínia Soares

Machine: DWL (Direct Write LASER)



Coating conditions:

- Vapour prime (5min HDMS) @ 130 °C (program 0):
 - deposition of an adhesive monolayer of HDMS (gas phase)
HDMS: hexamethyldisilazane [(CH₃)₃Si]₂NH (adhesive promoter for PR)
 - use program zero (5 min HDMS)
 - press reset and then start
 - check if pressure drops
 - make sure 41-42 appears on the display before taking the sample out

Step duration~30 min

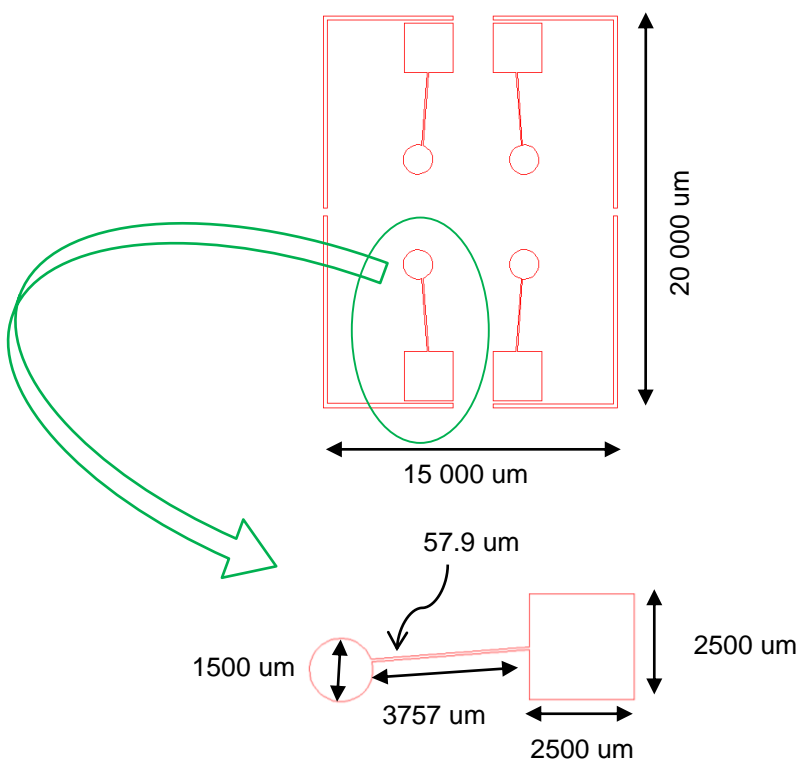
- Resist Coating

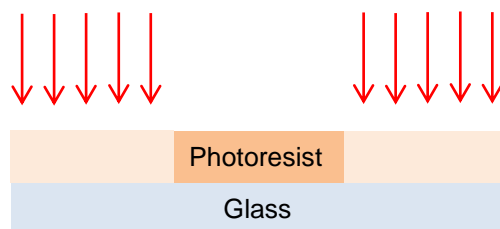
- Paste the substrate to a Si wafer with yellow tape on the four corners
- Put the wafer on the SVG track for coating
- Photoresist: Coater 6/2
 - 2.5 krot/min
 - 1.5um resist thickness
 - baking at 85°C for 1 min.

Side View (After Coating):**Exposing Conditions:**

Mask name: streaming_current_2013_1.dwg
Layer: Electrodes
Server File for DWL: strcurrelectrodes
Map: strcurr4
Die dimensions: [X: 15000 Y: 20000] um
Alignment marks: none
Focus: 50
Energy: 75

Approximate Exposure Time per die: 12min

Mask:

Side View (During Exposure):**Development:** recipe: 6-2

- Put the Si wafer on the SVG track for development
- Conditions:
 - 1 minute at 110°C
 - Development for 1 minute (program 2)

After the normal development, the sample is inspected with cleanroom microscope aid (be sure the filter is on). Overdevelop if necessary.

Side View (After Development):**STEP 3: 3000A TiW Deposition****Date:** 2013/09/18**Operator:** Fernando Silva**Machine:** N7000 (Magnetron sputtering)**Thickness:** 3000 A**Recipe:** TiW 1500A Low Power:

- 3x Module 3, Function 5: 0.5kW, 423V, 1,20A
- 2x Module 3, Function 3: 3 min cool down

Conditions:

Chamber pressure before deposition: 5.4E-9 Torr

Chamber pressure during deposition: 1.8E-3 Torr

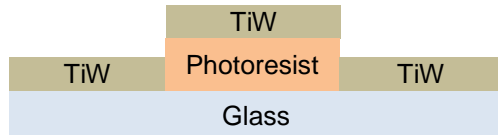
Subst Rotn: 30 rpm

Ar flux=50 sccm, N2 flux= 10 sccm

Power=0.5 kW (423V; 1,20 A)

Readpoint:

Ar flux=49.7 sccm, N2 flux=10 sccm
Power=0.5kW (423V; 1.20 A)

Side View (After Deposition):**Test Sample Thickness:****STEP 3: TiW Lift-Off**

Date: 2013/09/19

Operator: Rui Pinto

Machine: Wet Bench

- Place the sample in a beaker filled with microstrip 3001
- Place the beaker in the hotbath
- Apply ultra-sounds every half hour
- Clean the sample with IPA and DI water
- Rinse again with IPA and dry with N₂ stream

Conditions:

- Ambient Temperature
- Ultrasounds
- No Dilution

Batch: N2K13NAS (Microstrip 3001 Fujifilm)

Confirm the thickness of TiW deposited with the aid of Dektak profilometer

Side View: